

**Measurement of the B_d^0 Mixing Frequency Using a
 New Probability Based Self-Tagging Algorithm
 Applied to Inclusive Lepton Events from $p\bar{p}$
 Collisions at $\sqrt{s} = 1.8 \text{ TeV}$.**

by

Tushar Shah

Submitted to the Department of Physics
 in partial fulfillment of the requirements for the degree of

Doctor of Philosophy

at the

MASSACHUSETTS INSTITUTE OF TECHNOLOGY

September 2000

©Tushar Shah, 2000

Author
 Department of Physics
 July 12, 2000

Certified by
 Jerome I. Friedman
 Institute Professor
 Thesis Supervisor

Accepted by
 Thomas Greytak
 Professor
 Associate Department Head for Education

Measurement of the B_d^0 Mixing Frequency Using a New
Probability Based Self-Tagging Algorithm Applied to
Inclusive Lepton Events from $p\bar{p}$ Collisions at $\sqrt{s} = 1.8 \text{ TeV}$.

by

Tushar Shah

Submitted to the Department of Physics
on July 12, 2000, in partial fulfillment of the
requirements for the degree of
Doctor of Philosophy

Abstract

We present a measurement of the B_d mixing frequency performed in an inclusive lepton sample, $B \rightarrow l + X$. A secondary vertex identifies a B meson decay, and a high p_t lepton determines the flavor at the time of decay. We use a self-tagging algorithm (exploiting the correlation between the charge of particles produced along with a B meson and its flavor) in order to determine the B flavor at the time of production. Confusion of B daughter particles with charge-flavor correlated particles can cause significant degradation of the flavor tagging performance. Monte Carlo based probability distributions over kinematic and geometric properties of tracks are used to distinguish between potential self-tagging candidates and unidentified B meson daughters. We measure $\Delta m_d = 0.42 \pm 0.09(stat) \pm 0.03(sys) \times (\text{ps})^{-1}$.

Thesis Supervisor: Jerome I. Friedman
Title: Institute Professor

Measurement of the B_d^0 Mixing Frequency Using a New
Probability Based Self-Tagging Algorithm Applied to
Inclusive Lepton Events from $p\bar{p}$ Collisions at $\sqrt{s} = 1.8 \text{ TeV}$.

by

Tushar Shah

Submitted to the Department of Physics
on July 12, 2000, in partial fulfillment of the
requirements for the degree of
Doctor of Philosophy

Abstract

We present a measurement of the B_d mixing frequency performed in an inclusive lepton sample, $B \rightarrow l + X$. A secondary vertex identifies a B meson decay, and a high p_t lepton determines the flavor at the time of decay. We use a self-tagging algorithm (exploiting the correlation between the charge of particles produced along with a B meson and its flavor) in order to determine the B flavor at the time of production. Confusion of B daughter particles with charge-flavor correlated particles can cause significant degradation of the flavor tagging performance. Monte Carlo based probability distributions over kinematic and geometric properties of tracks are used to distinguish between potential self-tagging candidates and unidentified B meson daughters. We measure $\Delta m_d = 0.42 \pm 0.09(stat) \pm 0.03(sys) \times (\text{ps})^{-1}$.

Thesis Supervisor: Jerome I. Friedman
Title: Institute Professor

Eleven years ago, as a freshman at MIT, I knocked on Professor Jerry Friedman's office to ask if he would sponsor me in the Undergraduate Research Opportunities Program. Professor Friedman agreed to guide me into the world of physics, and continued to do so through my graduate years as well. Jerry employed his immense talents as a physicist and as a teacher since that very first day to help me become a better student and a better person. Jerry didn't have to put such an effort into my education; but he did. To a large extent the way I think about physics and the way I solve problems reflects those efforts. I am also grateful for the independence he allowed me in developing this analysis and the sense of collaboration with which he approached advising me.

It is largely because of Professor Paris Sphicas that I came to CDF in the first place. He exemplifies just how high one can set personal standards of excellence.

Gerry Bauer, Petar Maksimović, and Jeff Tseng played essential roles in the development of this analysis. The creativity and rigor of thought that they have shown throughout my time at Fermilab has taught me as much humility as it has physics.

Also at Fermilab, Petar, Troy, Wasiq, Dejan and Baber made life entertaining and intellectually stimulating the first few years out at the lab and Andreas, Ivan, Mike and Konstantine took over that role when those first guys went off to seek their fortunes. Ilya, Paul, and Sasha also made the trailers a more enjoyable place to be. Someone at the MIT admissions committee is doing their job well, as I can't imagine working in a better research group.

Without Steve Pavlon, nothing would work and life would be much more dull.

Sekhar and I experienced grad school in parallel. His friendship and perspective has helped me withstand many of the problems that one must encounter when doing a doctoral thesis. Ravi, Eric, and Laura were always an email or a phone call away when I needed them, which was often. Anne, Dev, Joel, Adam, Rob, Gunther and Kahlil helped me enjoy life outside of the lab and are friends in the truest sense.

My greatest debt is to my wife, Sara Zion. In every dimension of my life, Sara made things much better - often at her own considerable expense. Without her, I would not have completed this thesis and I would not be a happy person today.

Finally, I would like to acknowledge my parents. Their love and support can not be overestimated. Whatever sense of curiosity and integrity that I possess came from them.

It is impossible to properly acknowledge all of the people who helped make this thesis possible. In the last hectic moments of grad school, I am called upon to recognize those people who have meant so much to me over the past few years. I am sure that someone will read this and feel that their contribution was underestimated or ignored altogether. To this person, I say that you are right, and that I am sorry that I did not thank you adequately. I hope that I do so in the future.

Contents

1	Introduction	15
1.1	Preliminary Comments	15
1.2	Meson Mixing: A Two-State Quantum System	16
1.3	Quark Mixing and Δm_d in the Standard Model	18
1.4	The Historical Development Leading to the CKM Matrix	21
1.5	The CKM Matrix	23
1.5.1	Physics Beyond the Standard Model	25
1.6	Summary	27
2	The Experimental Apparatus	28
2.1	Introduction	28
2.2	The Accelerator	29
2.3	The CDF Detector	32
2.3.1	Defining the Coordinate System	32
2.3.2	Parameterizing a Track	34
2.3.3	Overview of the Detector	34
2.3.4	The Silicon Vertex Detector	35
2.3.5	The Vertex Time Projection Chamber	39
2.3.6	The Central Tracking Chamber	40
2.3.7	The Central Electromagnetic Calorimeter (CEM)	43
2.3.8	The Central Hadronic Calorimeter (CHA)	45
2.3.9	Muon Chambers	45
2.4	Data Acquisition	48

3	Overview of Mixing Methods	50
3.1	Ingredients of a Mixing Measurement	50
3.2	Data Selection	51
3.3	Flavor Tagging	51
3.3.1	Decay Flavor Tagging	52
3.3.2	Production Flavor Tagging	53
3.3.3	Time-Integrated Measurements	60
3.3.4	The Time Dependent Mixing Asymmetry	61
3.4	A Note About SST Algorithms Used with Inclusive Lepton Data . .	66
3.5	Summary of Methods in This Analysis	66
4	Data and Monte Carlo Samples	68
4.1	Lepton Selection Criteria	68
4.1.1	Electron Selection Criteria	69
4.1.2	Muon Selection Criteria	69
4.2	Secondary Vertex Finding	70
4.3	Monte Carlo Samples	73
4.4	Fake Electron Trigger Fraction	76
4.5	Electron Conversion Fraction	80
4.6	Electron Prompt Charm Fraction	83
4.7	Muon Fake Fraction	85
4.8	Muon Prompt Charm Fraction	85
4.9	$b\bar{b}$ and $c\bar{c}$ Particle Species	87
5	The Proper Time of Decay	88
5.1	Proper Time Reconstruction	88
5.2	k -Factor Distributions	90
5.3	The Proper Time Resolution	95
6	Flavor Tagging	102
6.1	Decay Flavor Tagging	102

6.2	Production Flavor Tagging	104
6.2.1	Avoiding Tagging on B Daughters	106
6.2.2	Parameterization of the Probability Distributions	113
6.2.3	L_{xy} Dependence of the Probability Distributions	115
6.2.4	Voting Algorithm	116
6.2.5	Charged and Neutral B Mesons and SST	118
6.2.6	Effect of Tagging on B Daughters in the Voting Algorithm . .	118
6.3	Measured Asymmetries	124
7	The Fit	125
7.1	The Fitting Method	125
7.2	The Probability Density Functions for B^0 Mesons	128
7.3	The Probability Density Functions for B^+ Mesons	128
7.4	The Probability Density Functions for B_s Mesons	129
7.5	The Probability Density Functions for Λ_b Baryons	129
7.6	The Probability Density Functions for Prompt Charm Mesons	130
7.7	Dilutions	131
7.8	Results	134
8	Systematic Uncertainties	137
8.0.1	Parameters	137
8.0.2	k -Factor Distributions	142
8.0.3	L_{xy} Resolution	143
8.0.4	Tagging on B Daughters	144
8.0.5	Dilutions for Particles Other Than B^0 and B^+	145
8.1	Total Systematic Errors	146
9	Conclusions	147
9.0.1	Future Applications	148
A	The Statistical Error on an Asymmetry	150

List of Figures

1-1	The Feynman diagrams for $B^0 - \bar{B}^0$ mixing.	20
1-2	The only $K^0 \rightarrow \mu^+ \mu^-$ diagram prior to the GIM mechanism.	22
1-3	A $K^0 \rightarrow \mu^+ \mu^-$ diagram which, by virtue of th GIM mechanism, sup- presses this decay mode.	22
1-4	The Bjorken Triangle reflecting unitarity of the CKM matrix.	27
2-1	The Accelerator Complex at Fermilab.	29
2-2	A Diagram of how we get proton-antiproton collisions starting with hydrogen gas.	31
2-3	An isometric view of the CDF detector.	33
2-4	A cross-section of the CDF detector.	35
2-5	An isometric view of the Silicon Vertex Detector.	36
2-6	An SVX ladder.	36
2-7	Resolution in impact parameter in the SVX as a function of the trans- verse momentum of reconstructed tracks.	37
2-8	An event display with two reconstructed B vertices.	38
2-9	A CTC endplate, showing the superlayer structure of tilted sense and field wire cells.	42
2-10	Feynman diagram for Bremsstrahlung.	44
2-11	Feynman diagram for the photon conversion process.	44
2-12	An $\eta - \phi$ map of the Muon Systems.	47
3-1	Feynman diagram for $b \rightarrow cW$, indicating the charge-flavor correlation between the lepton and the decaying b hadron.	52

3-2	The fragmentation of a heavy quark producing a fragmentation chain.	54
3-3	The fragmentation of a b quark into a neutral and charged B mesons. The correlation between the first charged particle in the fragmentation chain and the production flavor of the B meson is indicated. That the correlation is different for charged and neutral B mesons is shown. . .	55
3-4	A classical rigid rotator model of a meson.	56
3-5	The fragmentation of a heavy quark in the Lund model.	58
3-6	Soft Lepton and Jet Charge OST methods.	59
3-7	The definition of L_{xy}	65
4-1	The definition of a tracking jet.	71
4-2	The definition of the impact parameter with respect to the primary vertex.	72
4-3	A Comparison between the Monte Carlo and data of the muon and electron p_t distributions after p_t weighting.	75
4-4	The expected $\frac{dE}{dX}$ as a function of track momentum for muons, pions, electrons, kaons, and protons.	78
4-5	The $(\frac{dE}{dX}_i - \frac{dE}{dX}_e)/\sigma_i$ distribution for the trigger electrons, with a central Gaussian corresponding to the electron contribution super-imposed. .	79
4-6	The $(\frac{dE}{dX}_i - \frac{dE}{dX}_e)/\sigma_i$ for the conversion partner candidates.	81
4-7	The determination of the efficiency for trigger lepton conversion part- ner track reconstruction from an exponential fit of the p_t distribution of reconstructed partner tracks.	82
4-8	The determination of the $b\bar{b}$ fraction in the electron event sample using the secondary vertex mass distribution.	84
4-9	The determination of the $b\bar{b}$ fraction in the muon event sample using the secondary vertex mass distribution.	86
5-1	The transverse momentum for secondary vertex tagged jets from elec- tron data and Monte Carlo samples.	91

5-2	The transverse momentum for secondary vertex tagged jets from muon data and Monte Carlo samples.	92
5-3	k -Factor Distributions for $b\bar{b}$ particle species.	93
5-4	k -Factor distributions for $c\bar{c}$ particle species.	94
5-5	A comparison of the L_{xy} distributions from the electron data and the electron Monte Carlo samples.	96
5-6	A comparison of the L_{xy} distributions from the muon data and the muon Monte Carlo samples.	97
5-7	A comparison of the pseudo-proper time distributions from the electron data and electron Monte Carlo samples.	98
5-8	A comparison of the pseudo-proper time distributions from the muon data and muon Monte Carlo samples.	99
5-9	The resolution in proper time determined from the electron Monte Carlo.	100
5-10	The resolution in proper time determined from the muon Monte Carlo.	101
6-1	The definition of p_t^{rel}	105
6-2	Tracks that are closer to the primary vertex have larger values of r than tracks that are closer to the secondary vertex.	108
6-3	The distributions over r for B meson daughters and primary tracks for electron and muon Monte Carlo samples as well as the probability of finding a B meson daughter as a function of r	109
6-4	The distribution over ΔR for B meson daughters and primary tracks for electron and muon Monte Carlo samples as well as the probability of finding a B meson daughter as a function of ΔR	112
6-5	The parameterizations of the probability of finding a B daughter as a function of r for four regions in ΔR	114
6-6	The probability that a track is a B daughter as a function of r for three different L_{xy} cuts.	115
6-7	The optimization of the probability cut.	117

6-8	The probability of tagging on a B daughter as a function of L_{xy} when using the minimum p_t^{rel} and voting SST algorithms.	121
6-9	The probabilities of tagging on a B daughter as a function of pseudo-proper time given that the SST tag is associated with a B^0 and B^+ meson.	122
6-10	The asymmetry for daughter-tagged B^0 and B^+ events in the lepton Monte Carlo as a function of pseudo-proper time.	123
6-11	The measured asymmetries as a function of pseudo-proper time in the electron and muon data samples.	124
7-1	The dilution as a function of t' for $b\bar{b}$ particle species using the voting algorithm. Also shown are linear fits to the dilutions. The B^0 and B^+ dilutions have no t' dependence by construction and fits have no significant slopes: -0.04 ± 0.10 for neutral B mesons and 0.06 ± 0.09 for charged B mesons.	132
7-2	The dilution as a function of t' for $c\bar{c}$ particle species using the voting algorithm. These linear fits are used as the dilution shape in the determination of Δm_d	133
7-3	Fit results for the electron asymmetry as a function of t' from the combined electron and muon fit super-imposed over the measured asymmetries from the electron event sample.	135
7-4	Fit results for the muon asymmetry as a function of t' from the combined electron and muon fit super-imposed over the measured asymmetries from the muon event sample.	136

List of Tables

8.1	The first half of the input parameters to the fit.	140
8.2	The second half of the input parameters to the fit.	141
8.3	Systematic errors associated with the input parameters.	141
8.4	Systematic errors associated with the decay model.	142
8.5	Systematic errors associated with the modeling of electron isolation. .	143
8.6	Systematic errors associated with the resolution in L_{xy}	144
8.7	Systematic errors associated with the Monte Carlo model for daughter-tagging.	145
8.8	Systematic errors associated with the Monte Carlo determination of dilution ratios.	145
8.9	Combined systematic errors, dominated by the input parameters and the Monte Carlo model for daughter-tagging.	146

Chapter 1

Introduction

1.1 Preliminary Comments

Mixing is a common physical phenomenon characteristic of two-state quantum mechanical systems in which the physical states of interest do not diagonalize the Hamiltonian. In this case, the interesting states are superpositions of the eigenstates of the system and are not themselves stationary. The time evolution of these “mixed” states is oscillatory, with an oscillation frequency that depends on the Hamiltonian. This oscillatory behavior is called mixing. By measuring the oscillation frequency we can probe some fundamental properties of the system.

The B^0 and \bar{B}^0 mesons are strong interaction eigenstates but they are not weak interaction eigenstates and undergo flavor¹ oscillations: $B^0 \rightarrow \bar{B}^0$ and $\bar{B}^0 \rightarrow B^0$. We present a measurement of the mixing frequency, Δm_d , for these flavor oscillations in this thesis. By measuring Δm_d we can learn about one of the elements of the Cabibbo-Kobayashi-Maskawa [1, 2] quark mixing matrix in the Standard Model Lagrangian. The role this matrix plays in the phenomenology of weak interactions will be discussed in the next few sections. By measuring the elements of this matrix we can learn about

¹It is conventional to refer to flavor in two distinct ways which should be clear from context. Two quarks have different flavors if they are distinguishable according to the six quark flavors: up, down, charm, strangeness, topness and bottomness. Two B mesons are said to have different flavors if the charges of their b quarks differ.

much interesting physics, including the violation of the charge-parity (CP) symmetry in weak interactions and the physics beyond the standard model.

In addition to the measurement of an important parameter in the Standard Model, this thesis is also of experimental interest since new techniques have been developed that are useful for the study of physics associated with B mesons in the noisy environment of inclusive data from $\bar{p}p$ interactions.

1.2 Meson Mixing: A Two-State Quantum System

In the absence of the weak interactions, the B^0 and \bar{B}^0 states ($\psi_{\bar{b}}$ and ψ_b) would be degenerate eigenstates of the Hamiltonian, which would consist of strong and electromagnetic terms. The weak Hamiltonian is not diagonal in the B^0 - \bar{B}^0 basis and allows transitions between the two states. Ignoring the continuum states into which the B mesons will decay ², the Schroedinger equation for this two-state system can be written in the B^0 - \bar{B}^0 basis as:

$$i\frac{d}{dt}\psi = (\bar{M} - \frac{i}{2}\bar{\Gamma})\psi, \quad (1.1)$$

where

$$\bar{M} = \begin{bmatrix} m & m_{12} \\ m_{12}^* & m \end{bmatrix} \quad (1.2)$$

is the mass matrix,

$$\bar{\Gamma} = \begin{bmatrix} \Gamma & \Gamma_{12} \\ \Gamma_{12}^* & \Gamma \end{bmatrix} \quad (1.3)$$

is the decay matrix, and ψ is a two-state vector. We call ψ_1 and ψ_2 the states that diagonalize $\bar{M} - \frac{i}{2}\bar{\Gamma}$:

$$(\bar{M} - \frac{i}{2}\bar{\Gamma})\psi_1 = E_1\psi_1 \quad (1.4)$$

$$(\bar{M} - \frac{i}{2}\bar{\Gamma})\psi_2 = E_2\psi_2. \quad (1.5)$$

²This is the Wigner-Weisskopf [3] approximation developed in the context of line-width analysis of atomic spectra.

We can diagonalize $\bar{M} - \frac{i}{2}\bar{\Gamma}$ to find the eigenstates:

$$\psi_1 = \frac{p\psi_b + q\psi_{\bar{b}}}{\sqrt{|p|^2 + |q|^2}} \quad (1.6)$$

$$\psi_2 = \frac{q\psi_b - p\psi_{\bar{b}}}{\sqrt{|p|^2 + |q|^2}} \quad (1.7)$$

$$p = m_{12} - \frac{i}{2}\Gamma_{12} \quad (1.8)$$

$$q = \sqrt{(m_{12} - \frac{i}{2}\Gamma_{12})(m_{12}^* - \frac{i}{2}\Gamma_{12}^*)} \quad (1.9)$$

$$(1.10)$$

and the eigenvalues:

$$E_1 = m - \frac{i}{2}\Gamma - \sqrt{(m_{12} - \frac{i}{2}\Gamma_{12})(m_{12}^* - \frac{i}{2}\Gamma_{12}^*)} \quad (1.11)$$

$$E_2 = m - \frac{i}{2}\Gamma + \sqrt{(m_{12} - \frac{i}{2}\Gamma_{12})(m_{12}^* - \frac{i}{2}\Gamma_{12}^*)}. \quad (1.12)$$

Note that

$$E_2 - E_1 = \Delta m_d + \frac{i}{2}\Delta\Gamma, \quad (1.13)$$

where we have made the definitions

$$\frac{1}{2}(\Delta m_d + \frac{i}{2}\Delta\Gamma) = \sqrt{(m_{12} - \frac{i}{2}\Gamma_{12})(m_{12}^* - \frac{i}{2}\Gamma_{12}^*)}. \quad (1.14)$$

A state, ψ , which has definite flavor initially, $\psi(t=0) = \psi_b$, will evolve in time as follows:

$$\psi(t) = e^{-i(M - \frac{i}{2}\Gamma)t}\psi(0) = \frac{e^{-i(M - \frac{i}{2}\Gamma)t}(p\psi_1 + q\psi_2)}{\sqrt{|p|^2 + |q|^2}} = \frac{pe^{-iE_1t}\psi_1 + qe^{-iE_2t}\psi_2}{\sqrt{|p|^2 + |q|^2}}. \quad (1.15)$$

From this we can compute the probability of finding a \bar{B}^0 meson at time t given the particle started as a \bar{B}^0 initially:

$$|\langle\psi_b|\psi(t)\rangle|^2 = |\bar{p}|^4 e^{-(\Gamma - \frac{\Delta\Gamma}{2})t} + |\bar{q}|^4 e^{-(\Gamma + \frac{\Delta\Gamma}{2})t} + 2|\bar{p}|^2|\bar{q}|^2 e^{-\Gamma t} \cos \Delta m_d t, \quad (1.16)$$

where we have defined

$$\bar{p} = \frac{p}{\sqrt{|p|^2 + |q|^2}} \quad (1.17)$$

$$\bar{q} = \frac{q}{\sqrt{|p|^2 + |q|^2}}. \quad (1.18)$$

Note that $\left|\frac{p}{q}\right| = 1$ and thus $|\bar{p}| = |\bar{q}| = 1/2$. We ignored the states into which the B would decay, and therefore the probability of finding a B meson is not conserved, though it is necessary to normalize the distribution so that the particle decays at some time. Furthermore, $\frac{\Delta\Gamma}{\Gamma}$ for the B_d system is small [4]. The probability of finding a \bar{B}^0 meson at time t given the particle started as a \bar{B}^0 initially can be written as

$$|\langle\psi_b|\psi(t)\rangle|^2 = \frac{\Gamma}{2}e^{-\Gamma t}(1 + \cos \Delta m_d t) \quad (1.19)$$

and the probability of finding a B^0 meson at time t given the particle started as a \bar{B}^0 initially is

$$|\langle\psi_{\bar{b}}|\psi(t)\rangle|^2 = \frac{\Gamma}{2}e^{-\Gamma t}(1 - \cos \Delta m_d t). \quad (1.20)$$

We can see in Equation 1.20 that the probability that a \bar{B}^0 meson decays with the opposite flavor from when the particle was produced oscillates with the frequency Δm_d . The probability of finding a B meson of either flavor decay at some time is properly normalized to one:

$$\int dt \left(\frac{\Gamma}{2}e^{-\Gamma t}(1 - \cos \Delta m_d t) + \frac{\Gamma}{2}e^{-\Gamma t}(1 + \cos \Delta m_d t) \right) = \int dt \Gamma e^{-\Gamma t} = 1. \quad (1.21)$$

1.3 Quark Mixing and Δm_d in the Standard Model

So far the discussion has been quite general. We have assumed that $B^0 \rightarrow \bar{B}^0$ and $\bar{B}^0 \rightarrow B^0$ transitions are allowed by the weak interactions in the Standard Model, but we have not shown how this mixing is incorporated into the model and thus how Δm_d is related to parameters in the Standard Model Lagrangian. The origin of mixing in the Standard Model is the fact that the quark mass eigenstates (u, c, t, d, s, b) are not the same as the weak quark eigenstates (u', c', t', d', s', b'). Regardless of the origin of the quark masses, this is the case. In the Standard Model the quark-Higgs interactions generate the quark masses. It appears that the quark states that couple to the Higgs are not the weak eigenstates, because the mass matrix in the weak basis is not diagonal. The quark mass eigenstates and the weak eigenstates are related by

unitary transformations:

$$\begin{pmatrix} u \\ c \\ t \end{pmatrix} = U^{up} \begin{pmatrix} u' \\ c' \\ t' \end{pmatrix} \quad (1.22)$$

$$\begin{pmatrix} d \\ s \\ b \end{pmatrix} = U^{down} \begin{pmatrix} d' \\ s' \\ b' \end{pmatrix}. \quad (1.23)$$

We will use these unitary matrices to write the charged-current term in the weak Lagrangian of the Standard Model in terms of the quark mass eigenstates. In the weak eigenstate basis we have

$$\mathcal{L}_{cc} = \frac{g}{\sqrt{2}} W^\mu (\bar{u}', \bar{c}', \bar{t}') \gamma_\mu (1 - \gamma_5) \begin{pmatrix} d' \\ s' \\ b' \end{pmatrix} + c.c. \quad (1.24)$$

where g is a coupling constant and W^μ is the W boson field. By combining Equations 1.22, 1.23, and 1.24 we get

$$\mathcal{L}_{cc} = \frac{g}{\sqrt{2}} W^\mu (\bar{u}, \bar{c}, \bar{t}) \gamma_\mu (1 - \gamma_5) U^{up} (U^{down})^\dagger \begin{pmatrix} d \\ s \\ b \end{pmatrix} + c.c. \quad (1.25)$$

The matrix $V = U^{up} (U^{down})^\dagger$ is called the CKM quark mixing matrix. The elements of the CKM matrix are explicitly given by:

$$V = \begin{pmatrix} V_{ud} & V_{us} & V_{ub} \\ V_{cd} & V_{cs} & V_{cb} \\ V_{td} & V_{ts} & V_{tb} \end{pmatrix}. \quad (1.26)$$

It is conventional to think of the CKM matrix as only acting on the down-type quarks in Equation 1.25.

If the CKM matrix were diagonal the weak and mass eigenstates for the quarks would be the same. In this case, every quark would exchange W bosons with exactly one other quark. For example the top quark would always decay into a W and a b

quark and the bottom quark would be stable. Off-diagonal elements of the CKM matrix allow for inter-generational couplings and thus B^0 flavor oscillations. The lowest order Feynman diagrams through which B^0 mixing occurs is shown in Figure 1-1. We can see the contributions of the CKM matrix elements to these diagrams.

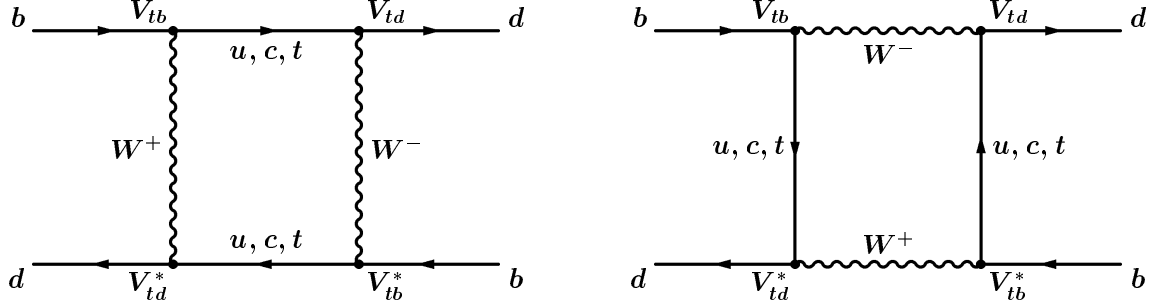


Figure 1-1: The Feynman diagrams for $B^0 - \bar{B}^0$ mixing. The top quark contribution dominates because the process has a quadratic dependence on the quark mass and therefore the V_{td} and V_{tb} CKM matrix elements determine the mixing frequency.

The value of Δm_d can be related to the elements of the CKM matrix by explicitly computing the amplitude for mixing from the Feynman diagrams shown in 1-1:

$$\Delta m_d = \frac{G_F^2}{6\pi^2} m_B m_t^2 F \left(\frac{m_t^2}{m_W^2} \right) \eta_{QCD} B_{B_d} f_{B_d}^2 |V_{tb}^* V_{td}|^2, \quad (1.27)$$

where G_F is the Fermi constant, m_B is the mass of the B meson, m_t is the mass of the top quark, F is the Inami-Lim function [5], η_{QCD} is a perturbative QCD factor, B_{B_d} is the non-perturbative bag factor, and f_{B_d} is the B meson decay constant. Equation 1.27 can be inverted to determine $|V_{td} V_{tb}^*|$ in terms of Δm_d with the uncertainty dominated by the theoretical determination of B_{B_d} and f_{B_d} . It should be noted that the theoretical uncertainties mostly cancel for the ratio of mixing frequencies for the B_d^3 and the B_s [6]: ⁴

$$\frac{\Delta m_s}{\Delta m_d} = (1.14 \pm 0.08) \left| \frac{V_{ts}}{V_{td}} \right|^2 \quad (1.28)$$

³When it is not clear from context what the flavor of the non- b quark in the B meson is we indicate it in a subscript.

⁴None of the formalism has relied on the properties of the non- b quark (called the spectator quark) and we therefore expect the B_s to exhibit flavor oscillations as well. The determination of the B_s mixing frequency is an important open problem in experimental physics.

1.4 The Historical Development Leading to the CKM Matrix

We have presented a description of B meson flavor oscillations in the context of quark mixing in the Standard Model. Here we place the notion of quark mixing in a historical context.

A lepton will only exchange a W boson with the other member of its generation. For example, the $e^- \rightarrow W^- \nu_e$ transition will occur but the $e^- \rightarrow W^- \nu_\mu$ will not, as was first observed at the AGS experiment [7] at Brookhaven. This leads to the existence of the conservation of electron, muon, and tau lepton number. The number of particles of a lepton generation minus the number of anti-particles of the generation is always the same before and after a particle interaction. If quarks also only interacted within their generations there would be similar conservation laws applying to them. Such a conservation law, however, is observed to be violated, for example in the strangeness-changing decays of the kaon.

In 1963 (one year before quarks would be proposed in the classic papers by Gell-Mann [8] and Zweig [9] and five years before the substructure of the proton was discovered in the classic MIT-SLAC experiments [10]) the weak hadronic currents were split into two pieces, a $\Delta S = 0$ piece corresponding to decays such as $n \rightarrow p e \nu$ and a $\Delta S = 1$ piece corresponding to decays such as $K \rightarrow \mu \nu$. Cabibbo [1] proposed a rotation between the $\Delta S = 0$ current and the $\Delta S = 1$ current, by an angle θ_c . According to Cabibbo (rephrased by Gell-Man in terms of the quark model), the u quark coupled not to the d , but rather to the superposition $d \cos \theta_c + s \sin \theta_c$. In this way, the $s \rightarrow W u$ transition could occur. The decay rates of strange hadrons could now be expressed in terms of $\sin \theta_c$. Unfortunately, this model did not always predict the decay rates for strange mesons very accurately. In particular, the $K^0 \rightarrow \mu^+ \mu^-$ decay rate is substantially overestimated. Figure 1-2 shows the Feynman diagram that contributed to this decay in the Cabibbo model.

In 1970, Glashow, Iliopoulos, and Maiani [11] predicted the existence of a fourth quark, the charm quark, in order to resolve this problem. They proposed a “mixing

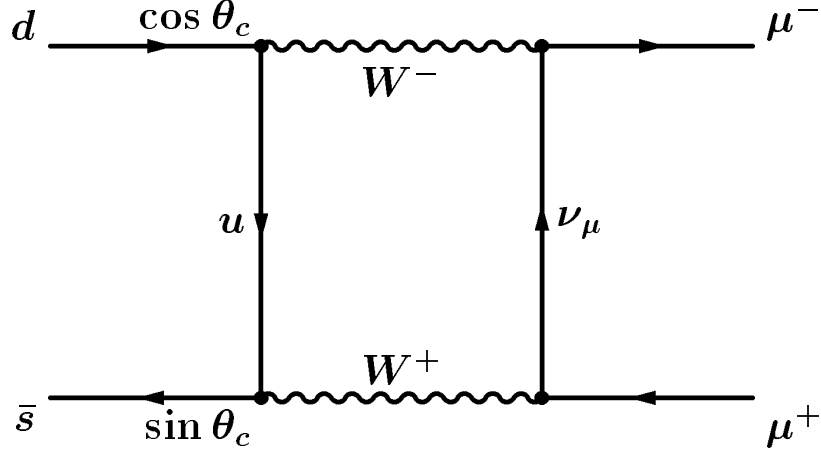


Figure 1-2: The only first order Feynman diagram for $K^0 \rightarrow \mu^+ \mu^-$ prior to the GIM mechanism.

matrix” that would rotate the d, s basis into the d', s' basis which coupled to the u and c :

$$\begin{pmatrix} d' \\ s' \end{pmatrix} = \begin{pmatrix} \cos \theta_c & \sin \theta_c \\ -\sin \theta_c & \cos \theta_c \end{pmatrix} \begin{pmatrix} d \\ s \end{pmatrix}. \quad (1.29)$$

By doing this, they introduced a second diagram for the $K^0 \rightarrow \mu^+ \mu^-$ decay, shown in Figure 1-3. If the charm and up quarks had the exact same mass, these two diagrams

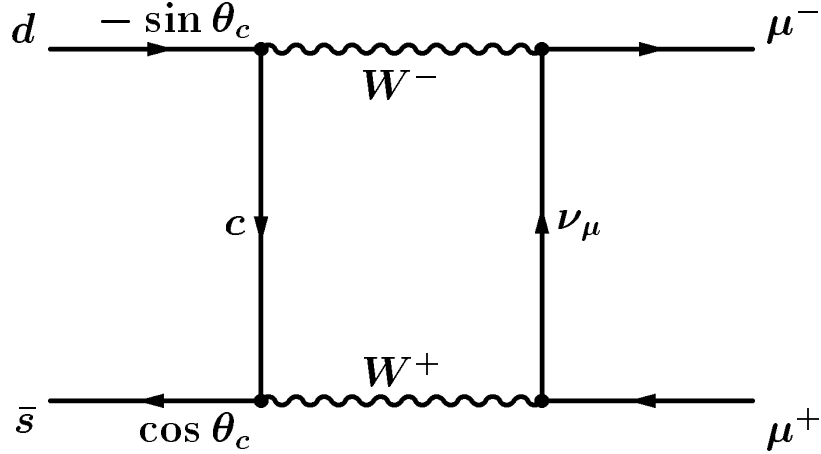


Figure 1-3: This diagram enters with a minus sign relative to the $K^0 \rightarrow \mu^+ \mu^-$ diagram shown in Figure 1-2. If the charm and up quarks had the same mass, the two diagrams would cancel entirely.

would cancel perfectly. Since their masses are not exactly the same, the new diagram suppressed the decay so that the predicted rate is consistent with experiments. This

is known as the GIM mechanism.

In 1973, one year before charmonium would be discovered, Kobayashi and Maskawa [2] added a third generation (the top and bottom quarks) to the model and generalized the GIM mixing matrix to be the most general unitary transformation from the flavor states of the down-type quarks to the weak interaction states of down-type quarks. This is the CKM matrix shown in Equation 1.26. They were motivated by the fact that a violation of the CP symmetry had been observed in 1964, by Cronin and Fitch, in the decays of the K^0 meson [12]. With three generations, Kobayashi and Maskawa could incorporate CP violation through the mixing matrix while with only two generations they could not, as will be discussed in the next section. The bottom quark was discovered in 1977 [13] and the top quark was discovered in 1995 [14], both at Fermilab.

1.5 The CKM Matrix

The independent elements of the CKM matrix are parameters in the Standard Model that can only be determined by experiments. CP violation can be introduced to the Standard Model through the CKM matrix if the matrix has a complex phase. Physics beyond the Standard Model may also become evident upon experimentally determining the properties of the CKM matrix.

CP Violation

The decay rates of the B and \bar{B} mesons into CP conjugate final states, $B \rightarrow f$ and $\bar{B} \rightarrow \bar{f}$, may be different if CP is violated. Suppose there are two paths by which the initial states can reach the final states. The total amplitude for the process $B \rightarrow f$ is given by $A + Be^{i\delta}e^{i\gamma}$ where the two amplitudes for the two paths are given by A and $Be^{i\delta}e^{i\gamma}$, and δ is a CP conserving (strong) phase while γ is a CP violating phase. The amplitude for $\bar{B} \rightarrow \bar{f}$ is therefore $A + Be^{i\delta}e^{-i\gamma}$. The decay rates are then just

$$\Gamma_B \sim |A + Be^{i\delta}e^{i\gamma}|^2 \tag{1.30}$$

$$\Gamma_{\bar{B}} \sim |A + Be^{i\delta}e^{-i\gamma}|^2. \quad (1.31)$$

$$(1.32)$$

The difference in decay rates is thus given by

$$\Gamma_B - \Gamma_{\bar{B}} \sim [\cos(\delta + \gamma) - \cos(\delta - \gamma)]. \quad (1.33)$$

If both δ and γ are non-zero, the rates are different. The CP violating phase γ can arise when the Lagrangian is complex. Violations of the CP symmetry have been measured in the kaon system. There is considerable effort underway to observe this symmetry violation in the B meson system and to determine if the CKM matrix will provide an explanation for this lack of symmetry. Techniques developed in this thesis may well prove useful in measuring CP violation in the B system.

Kobayashi and Maskawa recognized that the most generic 3×3 quark mixing matrix would be real for one or two generations of quarks, but with three or more generations of quarks, complex phases could be introduced to the matrix. They argued as follows. In general, for n generations of quarks, we would have an $n \times n$ mixing matrix. Any $n \times n$ complex matrix has $2n^2$ parameters. Unitarity provides $n(n-1)/2$ complex constraints and n real constraints. This leaves $n^2 = 2n^2 - 2(n(n-1)/2) - n$ independent parameters. Of these n^2 parameters, we can eliminate $2n-1$ by redefining the $2n-1$ independent quark phases. Therefore we are left with $(n-1)^2$ free parameters to be measured in an $n \times n$ mixing matrix. For $n = 3$, we have 4 independent parameters. Any 3×3 orthogonal matrix can be constructed from three independent parameters (usually taken to be the three Euler Angles). If all four parameters are non-zero, the matrix must be complex. This inclusion of a complex phase is needed for the description of the CP violation observed in the kaon system. Kobayashi and Maskawa recognized that if $n = 2$, as in the GIM description, there is only one free parameter, which is the Cabibbo mixing angle. This was the motivation for Kobayashi and Maskawa to predict the existence of the bottom and top quarks. It is an experimental issue to determine if the structure of observed decays is consistent with the picture of a CKM matrix with complex phase that is sufficient to provide CP violation in the weak decays of hadrons. The B system is a particularly convenient

system with which to probe the unitarity of the CKM matrix and the magnitude of the complex phase, as will be discussed in the next section.

1.5.1 Physics Beyond the Standard Model

The existence of any new charged particles which can couple to the quarks in the mixing diagrams shown in 1-1 would alter the mixing frequencies. The determination of the CKM matrix elements ignoring these new processes would be incorrect. In this case there is no reason to expect the incorrect *measured* CKM matrix to be unitary. The charged Higgs, for example may also contribute to processes like those shown in 1-1. A non-unitary measured matrix may be indirect evidence for the existence of new charged particles like the charged Higgs. Another possibility if the 3×3 CKM matrix is measured to be non-unitary is that there are as of yet undiscovered heavier quark generations. For n generations, the $n \times n$ mixing matrix must be unitary, but any $m \times m$ submatrix ($m < n$) need not be unitary. For example, the 3×3 CKM matrix in Equation 1.26 may not be unitary if there is a fourth generation of quarks.

The CKM matrix may well prove to be a window exposing new physics beyond the standard model.

Wolfenstein Parameterization and the Bjorken Triangle

A common parameterization of the CKM matrix was given by Wolfenstein in 1983 [15]. The four parameters are taken to be λ ($\sin \theta_c$), A , ρ , and η , and the matrix looks like:

$$\begin{pmatrix} 1 - \frac{\lambda^2}{2} & \lambda & A\lambda^3(\rho - i\eta) \\ -\lambda & 1 - \frac{\lambda^2}{2} & A\lambda^2 \\ A\lambda^3(1 - \rho - i\eta) & -A\lambda^2 & 1 \end{pmatrix}. \quad (1.34)$$

The matrix is accurate to fourth order in λ , which is roughly equal to 0.22 [4]. The parameters other than λ are all roughly of order unity. We can see in this parameterization that cross-generational weak decays are CKM suppressed by factors of λ .

The unitarity condition $VV^\dagger = 1$ yields the equations $\sum_j V_{i,j}V_{k,j}^* = \delta_{i,k}$. Note that the off diagonal conditions ($i \neq k$) can be represented as triangles in the complex plane. Each of the three terms is a vector in the complex plane and the sum of these vectors is zero. If the CKM matrix had been real, this triangle would lie entirely on the real axis. The greater the CP violating effects, the larger the area of the triangles. It is easiest to measure the area of a triangle when all of the angles are roughly the same size. The triangle defined by the unitarity condition

$$V_{ud}V_{ub}^* + V_{cd}V_{cb}^* + V_{td}V_{tb}^* = 0, \quad (1.35)$$

which can be written to leading order in λ as

$$A\lambda^3(\rho + i\eta) - A\lambda^3 + A\lambda^3(1 - \rho - i\eta) = 0, \quad (1.36)$$

is roughly equilateral, with each side proportional to λ^3 . Inspection of the CKM matrix elements included in this triangle (Equation 1.35) leads one to the conclusion that studying B decays is a very useful way of probing CP violation introduced via the CKM matrix. The triangle associated with Equation 1.35 is called the Bjorken Triangle [16] and is shown in Figure 1.5.1.

If there had been more generations, Equation 1.35 would have more terms (one for each new generation) and the associated figure in the complex plane would be a polygon with the number of sides equal to the number of generations. If it is experimentally found that the Bjorken Triangle is not closed, this would be evidence for new physics.

We showed in Equation 1.27 how Δm_d related to CKM matrix elements. We see that by measuring the B^0 mixing frequency we can constrain the edge of the Bjorken Triangle opposite to the angle γ . What's more, \bar{p} and \bar{q} of Equation 1.16 are also related to the angle β in the Bjorken Triangle through the relationship

$$\frac{\bar{q}}{\bar{p}} = e^{2i\beta}. \quad (1.37)$$

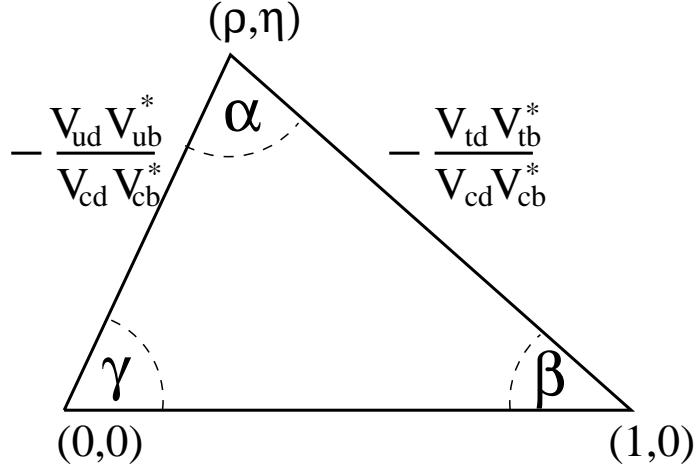


Figure 1-4: The Bjorken Triangle is one of the triangles representing the unitarity of the CKM matrix. The larger the area of the triangle, the greater the CP violating effects.

1.6 Summary

The CKM matrix is a component of the Standard Model which is related to the physics of CP violation and mixing. Much of the physics associated with the CKM matrix is represented graphically in the properties of the Bjorken Triangle, which is derived from a unitarity condition on the matrix. By measuring the frequency of flavor oscillations in the B_d system we constrain one of the edges of the Bjorken Triangle.

Chapter 2

The Experimental Apparatus

In this chapter we present a description of the Fermilab Tevatron and the Collider Detector at Fermilab (CDF). We focus primarily on the subsystems of the CDF detector relevant to this analysis. A detailed description of every component of the detector can be found in reference [17].

2.1 Introduction

The Collider Detector at Fermilab was designed for the study of a wide range of physical phenomena associated with the collisions of protons with antiprotons at very high energies. For this analysis we are specifically interested in the study of B mesons that were produced in those collisions, but CDF has also had great success in exotic, electroweak and strong physics and is responsible for the discovery of the top quark.

The data analyzed for this thesis were collected from the operation of the detector between January 1994 and July 1995. We describe the detector as it was during this data collecting period, called Run 1b. The $p\bar{p}$ collisions were provided by the Tevatron accelerator complex, where protons and antiprotons were grouped, accelerated, and collided. The center-of-mass energy of those collisions was 1.8 TeV, making it the highest energy collider in the world at the time of operation.

2.2 The Accelerator

Figure 2-1 shows the components of Fermilab's accelerator complex. Protons and antiprotons were produced and accelerated in several stages before they were collided in the Tevatron. By doing the acceleration in several stages, smaller rings could be used and a smaller beam profile could be achieved. Figure 2-2 demonstrates the process by which $p\bar{p}$ collisions are produced.

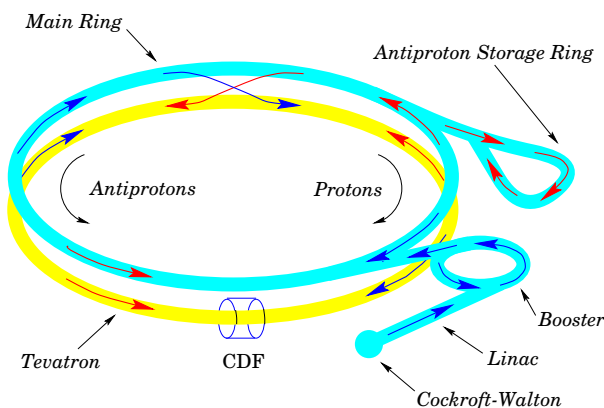


Figure 2-1: The Accelerator Complex at Fermilab.

The first step was to produce a beam of protons. Hydrogen gas was placed in a Cockroft-Walton chamber in which electrons were added to produce H^- ions. A strong static electric field across the chamber accelerated the ions to 750 keV. The ions were then released into a linear accelerator, known as the LINAC, where they were further accelerated to 400 MeV. Finally the negative hydrogen ions were stripped of their electrons by being passed through a carbon foil, leaving a 400 MeV beam of protons.

The proton beam was next sent to a synchrotron accelerator with a radius of 75 meters. This accelerator, known as the Booster, brings the proton beam energy up to 8 GeV and divides the protons into 12 separate bunches, with roughly $N_p \sim 2 \times 10^{11}$ protons per bunch. The proton bunches were passed to another synchrotron accelerator; this one with a radius of 1 km. Here, in the Main Ring, the proton bunches were accelerated to 150 GeV. These proton bunches were either injected into the Tevatron, or used for the production of antiprotons that were in turn injected

into the Tevatron for collisions.

Antiprotons were produced from the proton bunches in the Main Ring by colliding the proton beam with a fixed Tungsten target, in which proton-nucleon scattering left antiprotons in the final state. The antiprotons were cooled in the Debuncher Ring and stored in the Accumulator ring. Once a sufficient number of antiprotons had been accumulated (typically $N_{\bar{p}} \sim 6 \times 10^{10}$ per bunch) the antiproton bunches were sent to the Tevatron where they were accelerated to 150 GeV. Because protons and antiprotons are oppositely charged, they travel in opposite directions in the Tevatron and could be accelerated simultaneously.

Once six proton bunches and six antiproton bunches were orbiting in the Tevatron, they were accelerated to 900 GeV, giving a 1.8 TeV center-of-mass energy of collisions. Each beam was focused to a transverse diameter of about $25 \mu\text{ m}$ at the interaction region for CDF. Each bunch was about 30 cm longitudinally. The two beams collided at two locations, called D \emptyset and B \emptyset , where sit the two detectors, D \emptyset and CDF.

The rate at which events of a given type will be produced from the collisions is given by $\sigma_p \mathcal{L}$, where σ_p is the cross-section for the production of those events and \mathcal{L} is the instantaneous luminosity, defined as

$$\mathcal{L} = \frac{N_p N_{\bar{p}} N_B f}{\sigma_A}. \quad (2.1)$$

N_p is the number of protons in each bunch, $N_{\bar{p}}$ is the number of antiprotons in each bunch, N_B is the number of bunches, f is the frequency of revolution for a bunch, and σ_A is the geometric cross-sectional area of the beam. The average instantaneous luminosity during Run 1b was $1.6 \times 10^{31} \text{ cm}^{-2}\text{s}^{-1}$. The integrated luminosity was roughly 90 pb^{-1} .

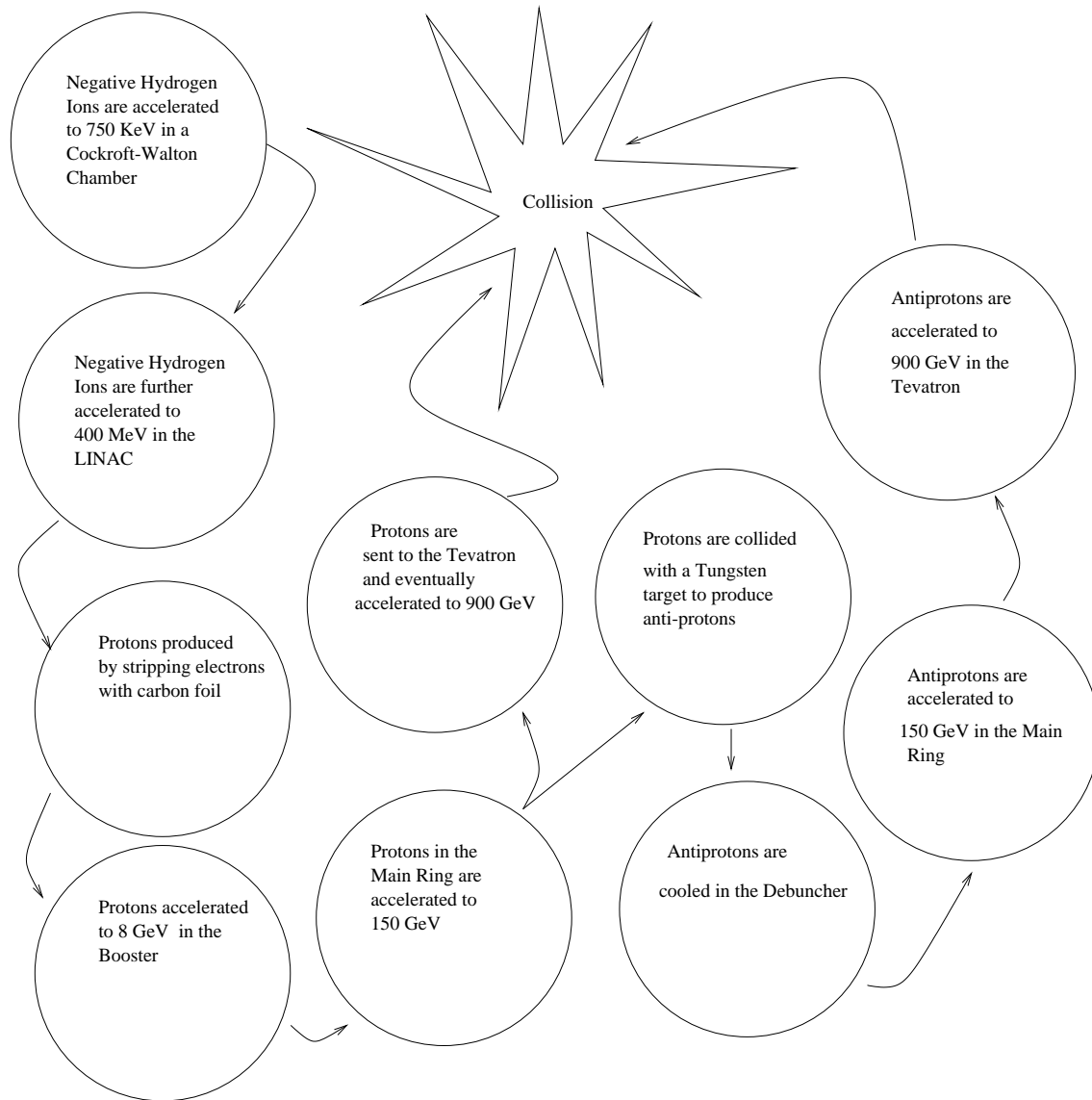


Figure 2-2: A diagram of the process of producing $p\bar{p}$ collisions starting with hydrogen gas.

2.3 The CDF Detector

The CDF detector was the first general purpose detector built to exploit the Tevatron collider. Here we discuss the subsystems of the detector most important to this analysis.

The most basic construct for us is a *track*, which is an estimate of the path taken by a charged particle in the detector. Tracks were measured with three *tracking detectors*, called the SVX, VTX, and CTC, placed in a 1.4 T magnetic field oriented along the beam axis. The curvature of the track is related to the momentum of the particle transverse to the beam axis. Neutral particles which do not decay in the tracking detectors do not leave tracks, and are detected through their energy deposition in *electromagnetic* and *hadronic calorimeters*. We identify muons with the help of the *muon systems*. Before we discuss these detector components we introduce the coordinate system used to describe the geometry of events at CDF and the parameterization of the trajectory of a particle in the detector.

2.3.1 Defining the Coordinate System

Figure 2-3 shows a three-dimensional view of the detector. As can be seen in this figure, the detector has azimuthal and forward-backward symmetry. A cylindrical coordinate system with the z -axis oriented along the proton 3-momentum at the interaction point is therefore a natural choice for the description of the detector. We will refer the radial components of a 3-vector, \vec{V} , by $V_t = \sqrt{V_x^2 + V_y^2}$. The polar angle θ is defined as the angle with respect to the positive z -axis. The azimuthal angle ϕ is measured with respect to the positive x -axis, which is defined in the right handed Cartesian coordinate system with the same z -axis and the y -axis pointing away from the center of the earth at the interaction point.

There is a complication in the choice of natural coordinates for the description of collision remnants at CDF. Although we know the momentum of the protons and antiprotons in each collision very accurately, we do not know the fraction of that momentum carried by the partons involved in the interaction. This fraction

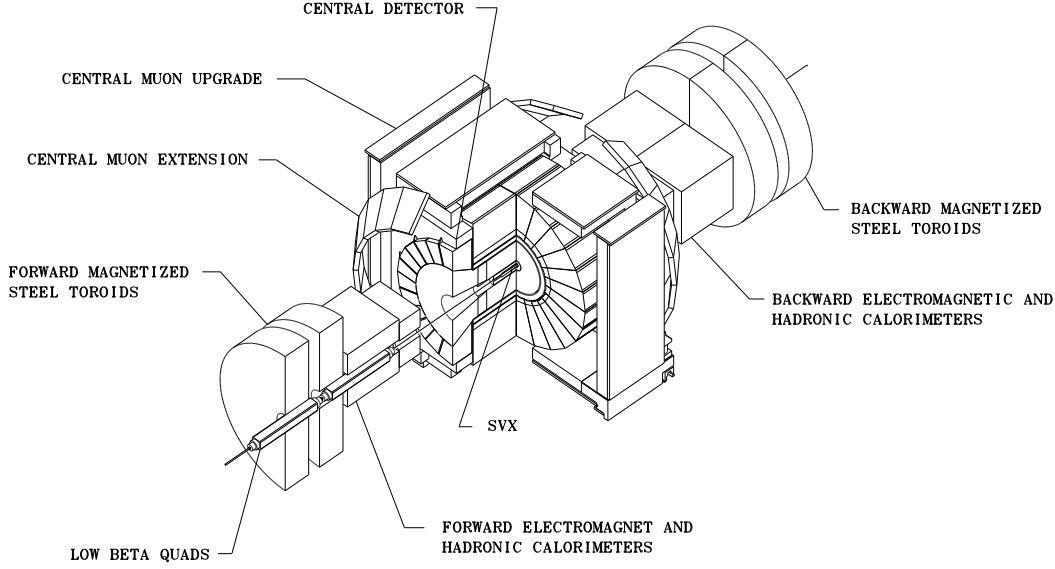


Figure 2-3: The CDF detector

is described by the structure functions of the proton. Typically the fraction of the proton momentum carried by partons in the production of B mesons is small. Because the fraction of momentum carried by the parton in the proton may be different from the fraction of momentum carried by the parton in the antiproton, the parton-parton interaction does not occur at rest in the laboratory reference frame. Additionally, the boost will vary from event to event and is unknown. Consequently we are interested in constructing physical variables that are invariant under boosts along the beam axis. The transverse projection of vectors obviously satisfies this requirement, but there is another variable, called the rapidity, which is also useful. The rapidity of a track, defined by

$$y \equiv \frac{1}{2} \ln \left(\frac{E + p_z}{E - p_z} \right), \quad (2.2)$$

has a convenient transformation under boosts, β_z , in the z direction:

$$y \rightarrow y + \tanh^{-1} \beta_z. \quad (2.3)$$

Therefore, the difference of rapidities of two tracks is invariant with respect to boosts in the z direction:

$$\Delta y' = (y'_1 - y'_2) = (y_1 + \tanh^{-1} \beta_z) - (y_2 + \tanh^{-1} \beta_z) = (y_1 - y_2) = \Delta y. \quad (2.4)$$

When the energy of a particle is much greater than the mass of the particle (typical for the high energy particles produced in $p\bar{p}$ interactions) we can approximate the rapidity with the pseudorapidity, defined as

$$\eta \equiv \frac{1}{2} \ln \left(\frac{p + p_z}{p - p_z} \right) = -\ln \tan \frac{\theta}{2}. \quad (2.5)$$

2.3.2 Parameterizing a Track

A charged particle traveling with a fixed energy in a uniform magnetic field will undergo a helical trajectory. Any helix can be uniquely determined by five independent parameters. We will describe charged particle tracks with the following five parameters:

- The momentum transverse to the z -axis: p_t ,
- The pseudorapidity: η (sometimes we use $\cot(\theta)$ instead),
- The shortest distance between the beam-line and the helix: d_0 ,
- The azimuthal angle at the point of closest approach: ϕ_o ,
- The z -coordinate of the point on the helix when closest to the z -axis: z_0 .

2.3.3 Overview of the Detector

Figure 2-4 is a cross-sectional view of the CDF detector with the major detector components labeled. We used only the central region of the detector, $|\eta| < 1.1$ for this analysis. Starting at the collision point and moving radially outward, a particle first finds the Silicon Vertex detector, a high precision tracking detector used to measure the location of tracks near the interaction point in the transverse plane. Next is a vertex time projection chamber called the VTX, which provides tracking information in η and is used to determine the z location of the primary vertex. The Central Tracking Chamber (CTC) is the main tracking detector and is situated next. All three tracking chambers are in a 1.4 T magnetic field oriented along the incident proton beam direction. The electromagnetic and hadronic calorimeters are situated outside

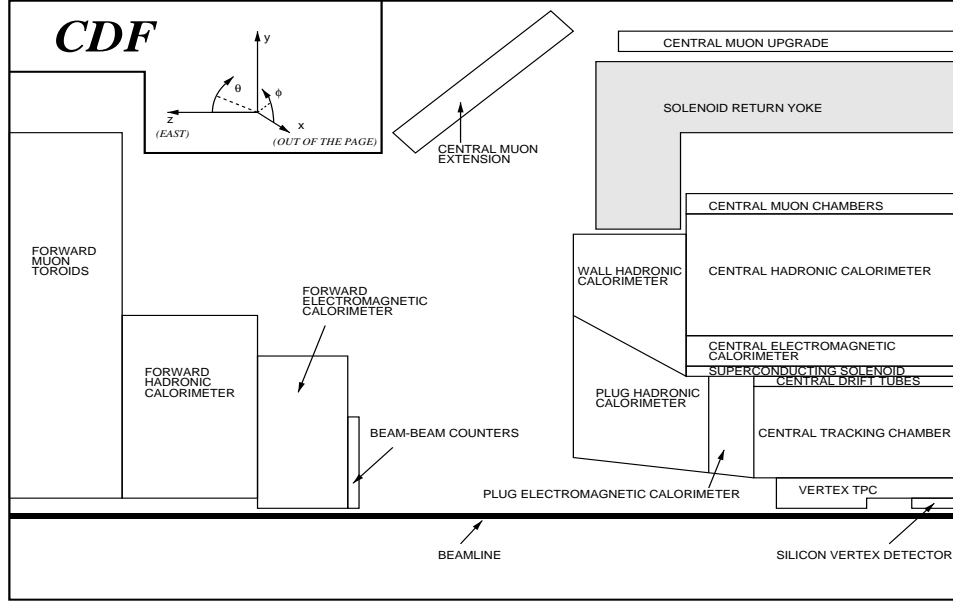


Figure 2-4: A cross-section of the CDF detector with the coordinate system indicated in the top left corner.

of the CTC. In this analysis we use the calorimeters to identify electrons. Outside of the hadronic calorimeter are two muon chambers, the Central Muon Chamber (CMU) and the Central Muon Upgrade (CMP).

2.3.4 The Silicon Vertex Detector

The Silicon Vertex Detector is a barrier-layer solid state detector. This detector provides a precise measurement of the position of tracks close to the interaction point because it is made of microstrip detectors with spacing of less than $100 \mu\text{m}$. A secondary vertex is a track vertex displaced from the primary vertex by a distance that is consistent with being the decay products of a long-lived particle. We use the SVX to identify secondary vertices corresponding to B decays.

An isometric view of the SVX can be seen in Figure 2-5. The active region of the SVX is 51 cm, made up of two cylindrical barrels of equal length with a gap of 2.15 cm at the center of the detector. Each barrel consists of four concentric layers at radii of 2.94 cm, 4.37 cm, 5.84 cm, and 8.07 cm. Each layer consists of twelve plane sections oriented to form a dodecagon in a transverse cross-section. These

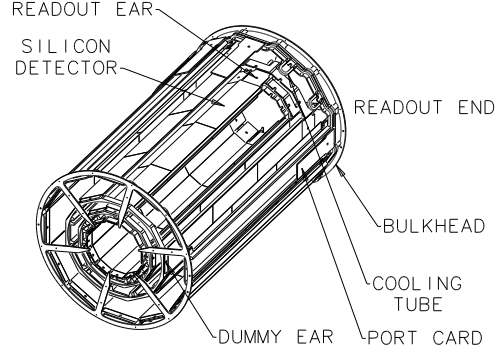


Figure 2-5: An isometric view of one barrel of the Silicon Vertex Detector.

planes, called “ladders,” have three silicon wafers with microstrips oriented along the z -axis. Figure 2-6 shows a depiction of a ladder in the SVX. The spacing between the microstrips is 60 microns for the first three layers and 55 in the fourth, giving a total of 256, 384, 512, and 768 strips in the four layers. Because the microstrips

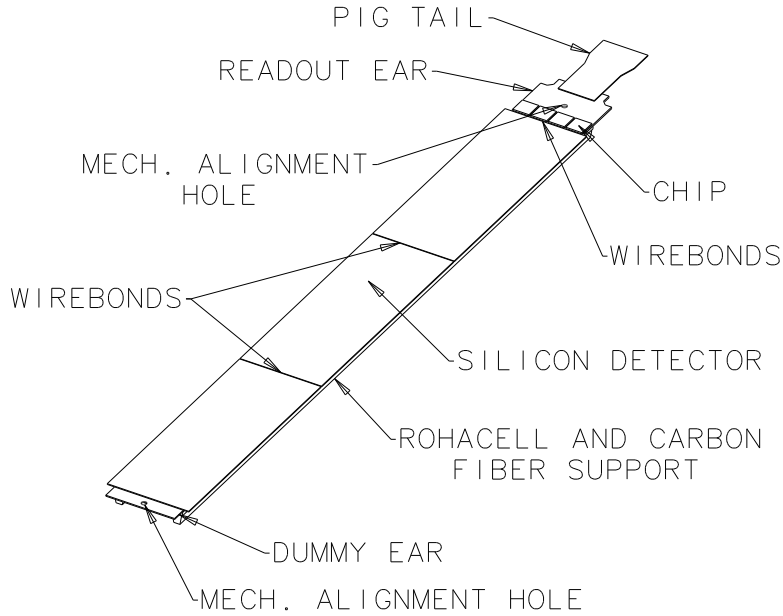


Figure 2-6: An SVX ladder.

are oriented along the z direction and the readout from the detector is always on the same end of each ladder, there is no useful η information in the location of SVX hits, and the detector is only useful for the measurements of track positions in the $r - \phi$

plane.

Tracks in a secondary vertex should have a non-zero distances of closest approach to the z -axis (d_0). The resolution in d_0 as a function of p_t is shown in Figure 2-7. When all four silicon layers have hits, the resolution is even better, reaching 16 microns at $p_t > 5.0$ GeV.

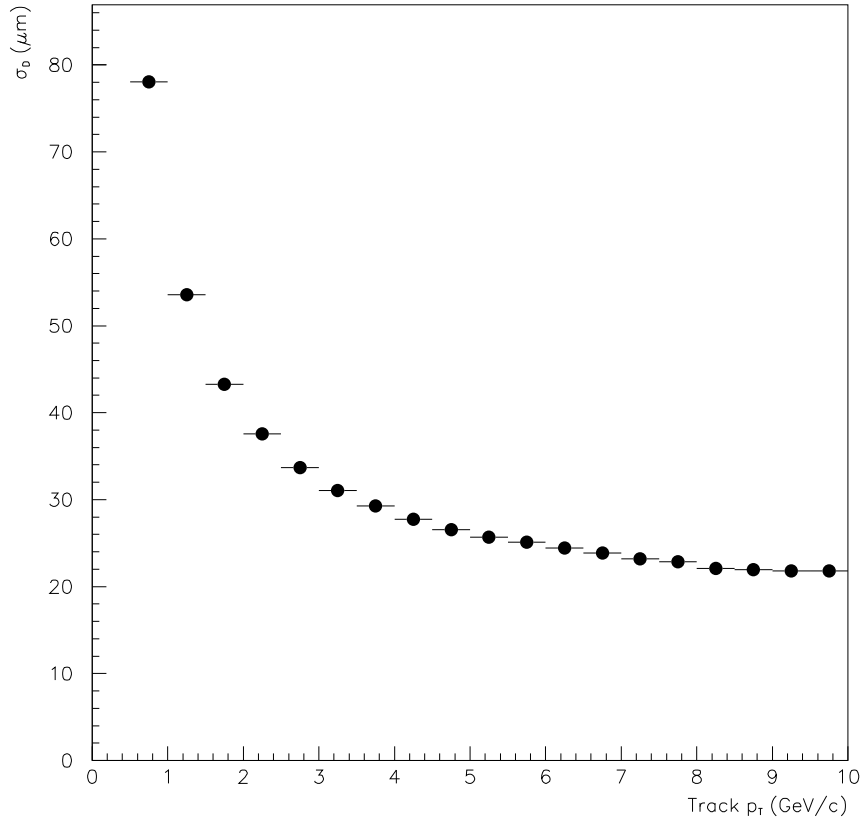


Figure 2-7: The resolution in the impact parameter in the SVX as a function of the transverse momentum of the tracks. The tracks were not required to have hits in all four silicon layers.

Figure 2-8 shows a display of an event in the CDF detector. As can be seen in the inset image, there are two secondary vertices reconstructed in the SVX, one corresponding to a $B \rightarrow J/\psi K^*$ (with the J/ψ decaying to two muons and the K^* decaying to a charged kaon and a charged pion) and the other corresponding to the decay of the other b hadron. The muons formed an invariant mass equal to the J/ψ

mass, the K, π provided a K^* , and the four tracks in that vertex form an invariant mass equal to the B mass. The SVX is a powerful tool in the identification and study of B mesons by allowing us to identify tracks displaced from the primary vertex.

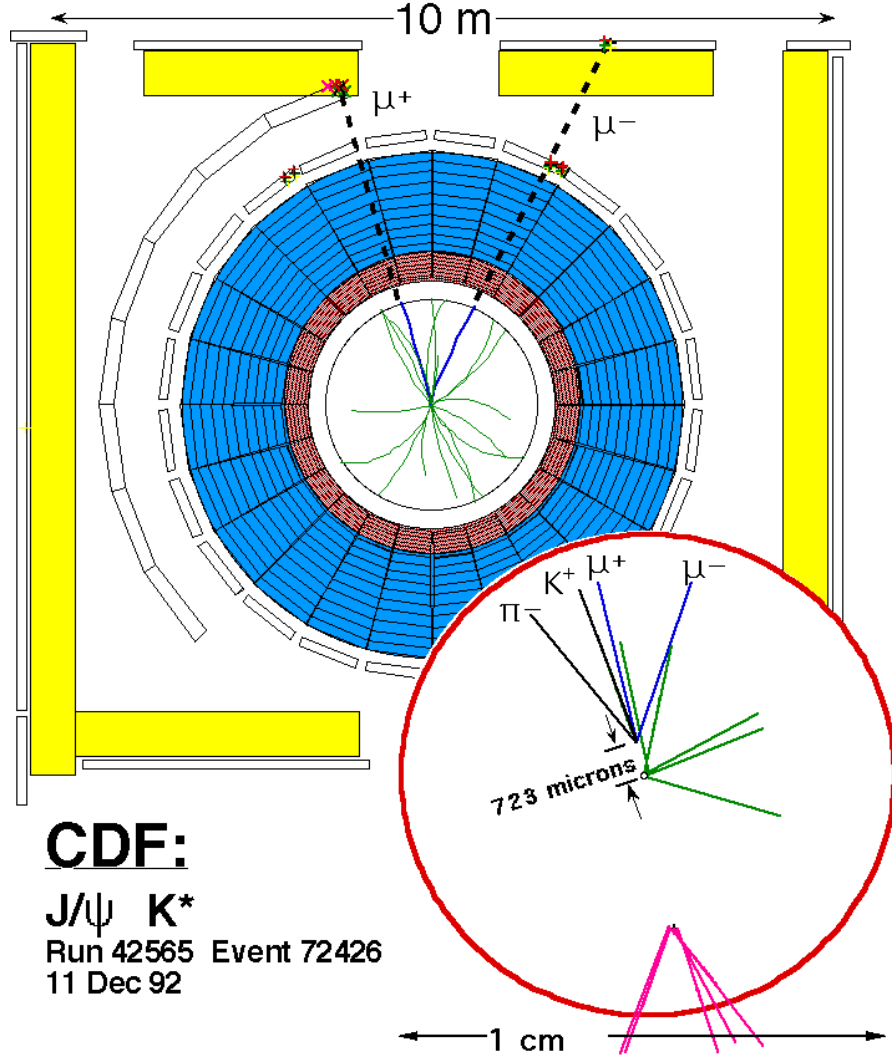


Figure 2-8: A CDF event with two B meson secondary vertices reconstructed in the Silicon Vertex Detector.

2.3.5 The Vertex Time Projection Chamber

As mentioned before, the collisions between protons and antiprotons are distributed about 0.0 in the z direction with a relatively large width of 30 cm. The purpose of the VTX is to help determine the location in z of the primary interaction. Roughly 5 percent [18] of the tracks in reconstructed B events are actually due to $p\bar{p}$ interactions different from the one that produced the $b\bar{b}$ pair. These “pile-up” tracks can be identified using the VTX, since the unwanted $p\bar{p}$ interaction is separated from the one of interest in z .

This time projection chamber consists of eight modules situated end-to-end along the z -axis covering a regions of $|\eta| < 3.25$. Each module is divided into two 15.25 cm long drift regions by a central high voltage grid. The chambers are filled with equal parts of argon and ethane. When a charged particle traverses the chamber, the gas is ionized. Electrons drift away from the center grid to a cathode grid and then to a proportional chamber in the endcaps. Each endcap is divided into eight octants which contain twenty-four sense wires and cathode pads. The sense wires are oriented transversely to the \hat{r} and \hat{z} directions. The arrival times of electrons at the sense wires provide an $r - z$ projection of a track.

The resolution in z of the measured position of the primary vertex depends on the number of tracks in the vertex, and typically ranges between one and two millimeters.

2.3.6 The Central Tracking Chamber

The CTC is a cylindrical drift chamber which extends 3.214 m in the z direction and 1.011 m in the radial direction, starting at a radius of 0.309 m. Like the VTX, the CTC is filled with an argon-ethane mixture of gas which is ionized by charged particles. There are 36504 wires oriented along the z direction connecting the endplates of the CTC. Most of these wires serve to produce an electric field in which the electrons formed in the ionization of the argon-ethane gas are accelerated. Some of them, however, are sense wires used to collect the electrons and provide a location measurement of the charged particle. The sense wires have a much smaller diameter than the other wires (40 microns compared to a few hundred microns), allowing the electric field to get very strong near the wire. This strong field causes drifting electrons to accelerate strongly near the wire and, through interactions with gas in the vicinity, cause even more ionization, a process known as “gas amplification.”

Figure 2-9 is a view of one of the endplates. The general structure is that of 9 concentric rings called “superlayers.” Each ring consists of a series of slots. The endpoints of the wires that are strung between the two endplates connect to the endplate uniformly along these slots. Taken as a whole, the set of wires belonging to the same slot form a planar strip traversing from one endplate to the other. Along the radial direction, the wires are all at the same voltage. Along the $\hat{\phi}$ direction, the voltage on the wires alternate in sign going from slot to slot. If the CTC were not in a magnetic field and the slots were radial, the direction of electron drift in the chamber would be along the electric field, in the $\hat{\phi}$ direction. Since the chamber is in a 1.4 T magnetic field oriented along the z -axis, the slots are tilted (by roughly 45°) to compensate. In this way, the drift direction is still azimuthal, which is optimal for the measurement of the positions of radial (“stiff”) tracks.

We use the CTC to measure several basic properties of tracks. Like the SVX, the position measurements of tracks help us to determine the impact parameter, d_0 and azimuthal angle ϕ_o . In the transverse plane, the charged particle (helical) trajectories are simply circles. The radius of the circle is determined by the transverse momentum

of the particle and the strength of the magnetic field transverse to the plane:

$$\frac{1}{2R} = \frac{cB}{2p_t} \times 10^{-9}, \quad (2.6)$$

where the speed of light, c , is measured in m/s, $B = 1.4$ T, and p_t is the transverse momentum of the track measured in GeV/c. We can therefore measure the p_t of a particle from the curvature of a reconstructed track in the CTC. The wires in the outermost superlayer, and in every alternate superlayer, are “axial”, meaning that they are aligned with the z -axis. There are twelve axial sense wires in each slot. The sense wires in the other superlayers are tilted $\pm 3^\circ$, so that measurements of the position in the $r - z$ plane can be made. There are six such “stereo” wires in each slot in these superlayers. The η (which can be expressed in terms of $\cot(\theta)$) and z_0 of tracks are measured with the stereo sense wires.

The resolution in p_t depends on the value of p_t since softer (low momentum) tracks have more curvature than stiff (high momentum) tracks. The resolution is given by

$$\frac{\delta p_t}{p_t} = 0.002 \times p_t \text{ GeV}^{-1}, \quad (2.7)$$

where p_t is measured in GeV/c. The existence of SVX hits constrains the tracks better and provides a combined resolutions that is nearly twice as good:

$$\frac{\delta p_t}{p_t} = \sqrt{0.0066^2 + (0.0009 p_t \text{ GeV}^{-1})^2}. \quad (2.8)$$

The resolution in z_0 is roughly 1 cm, and the resolution in $\cot(\theta)$ is roughly 0.01.

For the sense wires in three of the superlayers the pulse height is also recorded. This provides a measurement of the energy lost by the charged particle through ionization of the gas as a function of distance, $\frac{dE}{dX}$. The Bethe-Bloch formula,

$$-\frac{dE}{dX} = \frac{\alpha}{\beta^2} \left(\log \frac{2m_e \gamma^2 \beta^2 T_{max}}{I^2} - \beta^2 - \frac{\delta}{2} \right), \quad (2.9)$$

gives the energy loss of the particle in the material in terms of α , a constant characterizing the material, I , the mean ionization energy, T_{max} , the maximum kinetic energy that can be imparted to a free electron in a single collisions, δ , a density related correction, and the velocity of the particle, β . Particles with the same momentum

(and thus the same curvature in the tracking chambers) but different masses (and thus different velocities) will therefore lose different amounts of energy traversing matter. We can therefore gain some particle identification information from the $\frac{dE}{dX}$ measurement using the CTC.

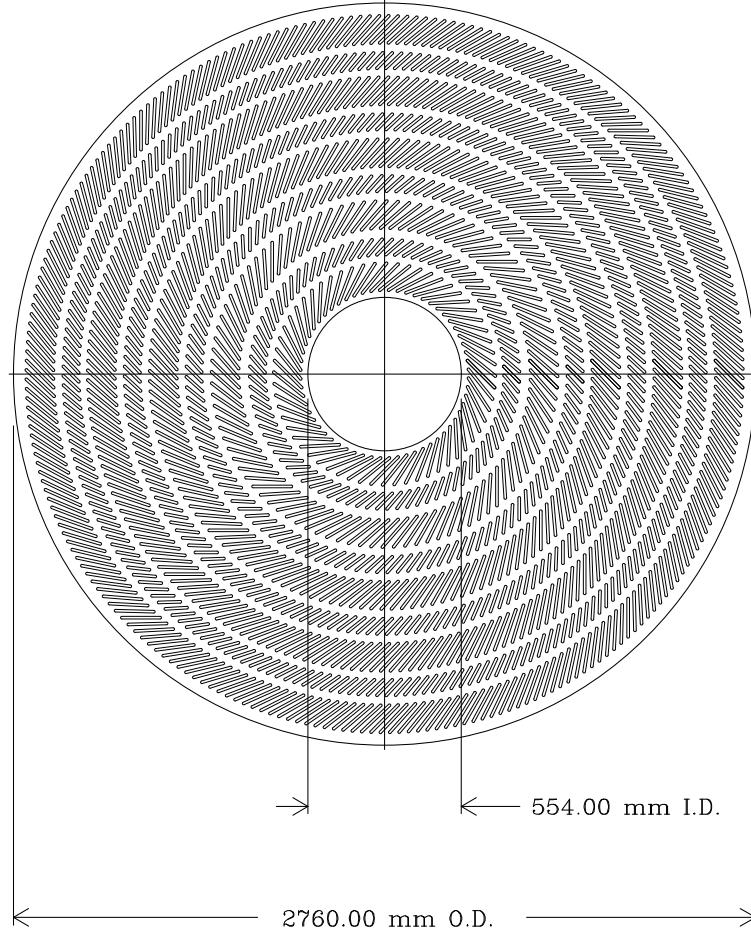


Figure 2-9: One of the endplates of the CTC. The concentric rings, or superlayers, consists of a series of slots where the field and sense wires attach to the endplate. The slots are tilted in order to produce an electric field such that, in the presence of the magnetic field oriented along the z -axis, the electron drift is in the azimuthal direction.

2.3.7 The Central Electromagnetic Calorimeter (CEM)

An electron will radiate photons when passing through a nuclear Coulomb field. This process, called bremsstrahlung, is illustrated by a Feynman diagram in Figure 2-10. These photons can in turn be converted into electron-positron pairs from interaction with matter (see the Feynman diagram in Figure 2-11). A high energy electron passing through matter will therefore produce a “shower” of positrons and electrons through bremsstrahlung and pair production. Eventually the electron energies fall low enough that the dominant energy loss is through ionization and excitation of the material through which it is passing. The electromagnetic calorimeter is designed to measure the ionization shower produced by an electron passing through dense matter. It consists of alternating layers of lead and scintillator. The shower is produced in the lead and detected in the scintillator. As the electrons and positrons pass through the scintillator, they excite molecules which then emit light which is gathered and detected by photo-multipliers. The initial electron energy is proportional to the total light collected by the scintillator.

The shape of the produced shower is characteristic of the incident charged particle. The transverse profile of the shower is measured with the use of a gas chamber with sense wires transverse to the radial direction situated 6 radiation lengths into the calorimeter. We can compare the transverse profile of the shower produced by a charged particle to the shape of the showers produced by known electrons during the test beam operation of the detector in order to distinguish between electrons and other charged particles that may have produced a shower in the electromagnetic calorimeter.

The CEM consists of 480 towers oriented radially. The $\eta - \phi$ projection of a tower is a rectangle of $\Delta\eta = 0.1$ and $\Delta\phi = 15^\circ$. Each tower is roughly 18 radiation lengths deep for an electron. The energy resolution for the CEM is

$$\frac{\delta E}{E} = \sqrt{\left(\frac{0.135 \text{ GeV}^{\frac{1}{2}}}{\sqrt{E}}\right)^2 + 0.0001}. \quad (2.10)$$

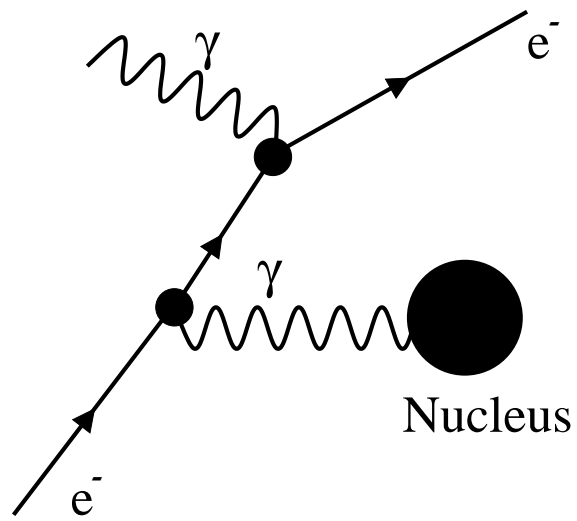


Figure 2-10: Electrons will radiate photons in the presence of nuclear coulomb fields in a process known as bremsstrahlung. Along with photon conversions into electron-positron pairs, the bremsstrahlung process contributes to the generation of electromagnetic showers.

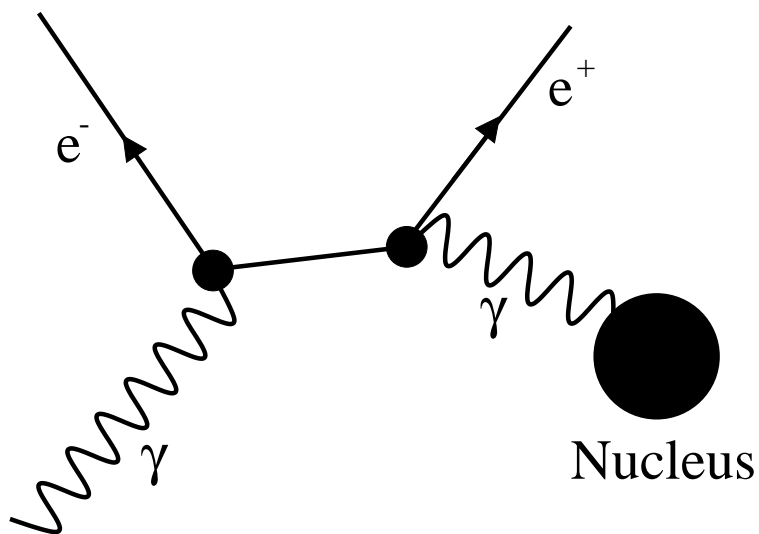


Figure 2-11: Photons can convert into pairs of electrons and positrons.

2.3.8 The Central Hadronic Calorimeter (CHA)

Hadrons generally pass through the electromagnetic calorimeters without significant energy loss since they are much heavier than electrons and thus do not undergo significant bremsstrahlung. Many hadrons are neutral and do not undergo bremsstrahlung at all. The dominant energy loss for hadrons comes from strong nuclear interactions. Hadronic showers are produced in the hadronic calorimeters from the interactions of the incident hadron with nuclei in the material that produce more hadrons. The design of the CHA is similar to the CEM, with a tower in the same $\eta - \phi$ positions behind each CEM tower. The scintillators are alternated with steel plates used to produce the hadronic showers. The CHA is 4.5 hadronic interaction lengths and has an energy resolution of

$$\frac{\delta E}{E} = \sqrt{\left(\frac{0.5 \text{ GeV}^{\frac{1}{2}}}{\sqrt{E}}\right)^2 + 0.0009}. \quad (2.11)$$

In this analysis, we use the hadronic calorimeter in order to reject hadrons that produced an early shower in the electromagnetic calorimeter and therefore appeared to be an electron.

2.3.9 Muon Chambers

Only muons and neutrinos are likely to penetrate through the hadronic calorimeters. The muons make it past the calorimeters since they do not interact strongly and do not lose as much energy to bremsstrahlung as electrons because of their heavier mass. There are muon chambers behind the hadronic calorimeter. The Central Muon System, the CMU, is directly behind the CHA (5.4 pion interaction lengths) while the Central Muon Upgrade, the CMP, is outside the return magnetic yoke (8.4 pion interaction lengths). Both detectors are simply four layers of drift chambers which measure track “stubs” that are then matched to tracks in the CTC. If a track appears to point from the CTC to a stub in the muon systems, it is likely that the track and stub correspond to a muon. The Central Muon Extension (CMX) was added to extend the η coverage of the muon systems, but was not used in this analysis because

of a large background rate due the fact that the beam halo interacted with the beam pipe just below the CMX. Figure 2-12 shows an $\eta - \phi$ map of the muon systems.

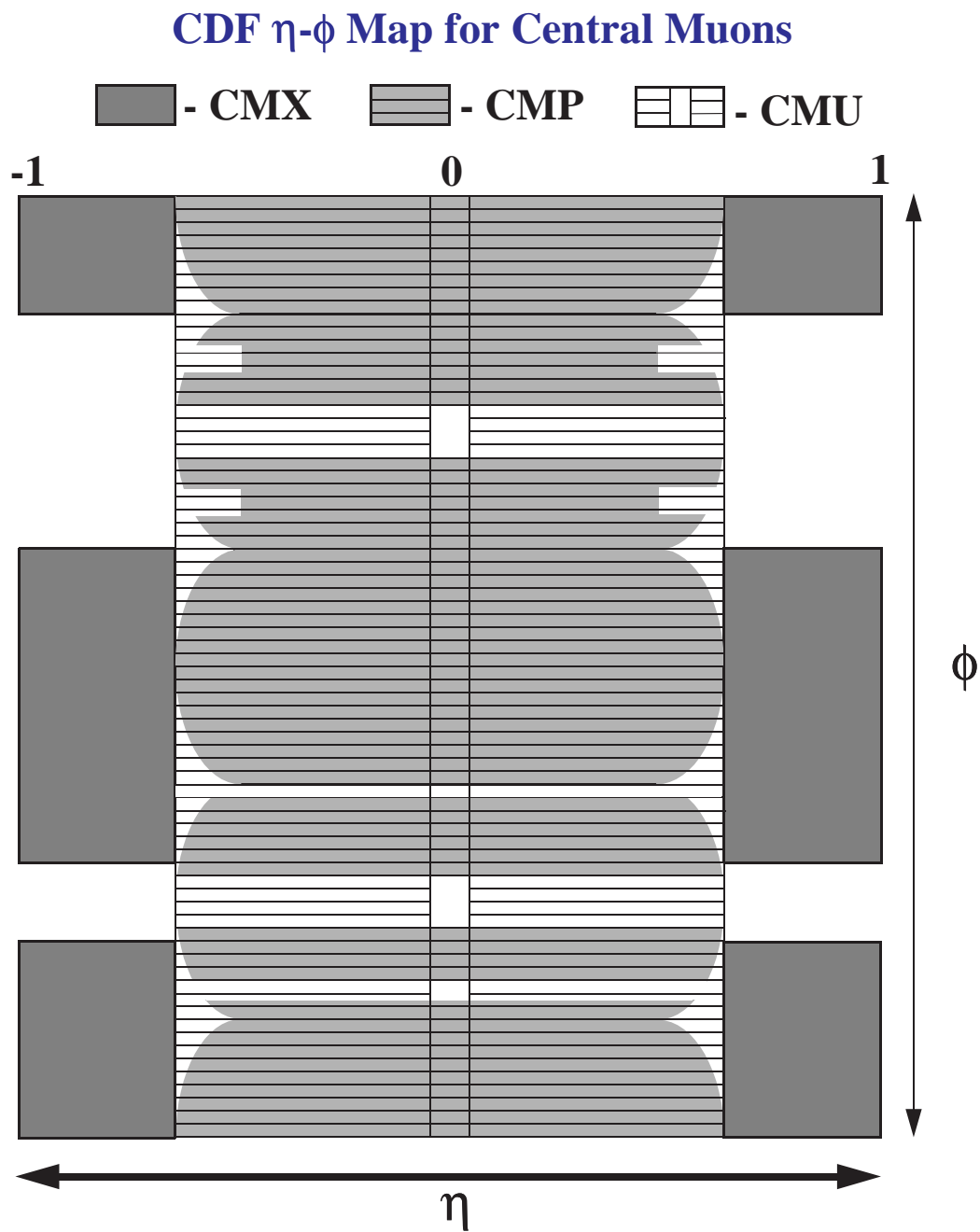


Figure 2-12: An $\eta - \phi$ map of the Muon Systems.

2.4 Data Acquisition

The proton and antiproton bunches crossed ~ 290000 times every second during the operation of the experiment. It was not feasible to record the outcome of each bunch crossing, as this would require prohibitively fast electronics and massive data storage. It would not even be desirable to record every event since the physically interesting physics phenomena, like the production of top quarks or SUSY particles (should they exist), occur very rarely. Once the decision to record an event has been made, it takes ~ 2 ms to actually read out the full detector. It is therefore possible to record at most ~ 500 events every second. Trigger logic is employed to identify the top $\sim 0.2\%$ most interesting events produced.

The purpose of the triggering system is to very quickly determine if an event is worthy of being recorded for analysis. The decision to record an event is made by applying four levels of filters to the data. As an event proceeds through the selection criteria, more computational resources are applied (and more time is spent) in determining if the event is to be recorded.

The first requirement was that an interaction should have occurred between the proton and the antiproton. On average, there were more than one proton-antiproton collision per bunch-crossing, so almost every crossing would satisfy this requirement. Still, the probability that there is no interaction at a beam crossing is governed by Poisson statistics and is not negligible. There are two sets of scintillator planes roughly 6 m on either side of $z = 0$. These “Beam-Beam Counters” (BBC) covered $3.2 < |\eta| < 5.9$. Almost every interaction is accompanied by some particles that are in the fiducial area for the Beam-Beam counters. The requirement that the BBC should have fired is called the “level 0” trigger. The other triggers are numbered 1 through 3.

The level 1 trigger decision was made on the basis of the analog readout of the detector. The raw detector readout is searched for rudimentary evidence of interesting physics, for example large energy deposition in calorimeters, the existence of a muon, or large missing transverse energy. Roughly a few thousand events passed level 1

every second.

The level 2 trigger decision was also made by hardware processors. This trigger took advantage of the Central Fast Tracker (CFT), hardware which used some of the information from the CTC to do first order tracking. Because of the 45° tilt of the slots in the CTC, a high energy track will pass close to at least one CTC sense wire in each superlayer. For such hits, the drift time would be very low since the ionized electrons would not travel a substantial distance. The CFT first searched for these prompt hits. For any sense wire with prompt hits, the CFT looked locally at other sense wires for non-prompt (delayed) hits. The CFT next compared the pattern of found hits (both prompt and delayed) to a look-up table in order to find hit patterns consistent with a track. In this way the CFT very quickly reconstructed some of the tracks in the event, allowing for tracking information to be used in the level 2 decision. The CFT is inefficient for low momentum tracks because it is unable to distinguish patterns when there is significant curvature in the tracks. Most of the events used in this analysis came from level 2 triggers which required an electron or muon candidate with a CFT track of at least 7.5 GeV. If an event passed a level 2 filter, it was written to a staging disk.

The level 3 trigger was an offline software trigger. A streamlined version of the CDF offline event reconstruction was used to analyze the data. Interesting events were eventually classified into “streams” associated with the type of physics identified by the level 3 analysis. The data was then stored and labeled according to its stream. The data of this analysis were taken from the inclusive lepton and inclusive muon level 3 data streams. This sample will be described in detail Chapter 4.

Chapter 3

Overview of Mixing Methods

In this chapter we present a framework for the determination of Δm_d with an emphasis on the techniques used in this analysis.

3.1 Ingredients of a Mixing Measurement

Any measurement of Δm_d must include three basic ingredients. First, a data sample must be selected. Typically B decays are identified through full or partial reconstruction of specific decay modes of B mesons. In order to enhance the statistical power of our measurement we used the semi-leptonic decays of B mesons inclusively. Second, the flavor of B mesons when they decayed must be determined. Third, the flavor of B mesons when they were produced must be determined. By comparing the flavors of B mesons when they were produced with the flavors of the mesons when they decayed, we can determine whether the B mesons mixed before decaying. These ingredients are sufficient to determine Δm_d , but greater statistical precision can be achieved by also determining the time a B meson lived before decaying in the reference frame of the meson. In this analysis we measure this proper time of decay and therefore directly observe the cosine dependence on the proper time of the mixing probability shown in Equation 1.16, from which we extract Δm_d .

3.2 Data Selection

On average, a B meson lives 1.5 ps before decaying. The B mesons that are selected by the inclusive lepton triggers have an average transverse momentum of roughly 20 GeV/c. Therefore, a typical B meson selected by the inclusive lepton triggers travel a few millimeters in the transverse plane before decaying. This is a large enough displacement that we can use the SVX to identify B meson daughter particles. Events with a high p_t lepton and a secondary vertex form a very pure sample of semi-leptonic decays of bottom hadrons. Not all of these bottom hadrons are B^0 's¹, however, and some of the vertices are due to semi-leptonic decays of charm hadrons. We can determine the prompt charm fraction of these events by exploiting the difference in mass between the charm and bottom quarks. There are a few other background sources of high p_t lepton candidates. Electron candidates can be hadrons which fake an electron signature or members of photon conversion pairs. Muon candidates can be hadrons that fake the signature of muons or decay products of kaons or pions. Although in the latter case the candidates are real muons, we still refer to them as “fakes” because they are not the muons for which we are looking. The backgrounds are accounted in the extraction of Δm_d .

3.3 Flavor Tagging

We use the term “flavor tagger” to mean an observable which is correlated to the flavor of a B meson associated with a secondary vertex. When the observable is correlated to the flavor of a B meson at the time of decay, it is called a “decay flavor tagger,” and when the observable is correlated to the flavor of a B meson at the time of production, it is called a “production flavor tagger.” In this section we describe the decay and production flavor taggers used in this analysis as well as those commonly used in measurements of Δm_d .

¹When referring to a particle name, we often mean both the particle and the charge-conjugate. It should be clear from context when the charge conjugate is implied.

3.3.1 Decay Flavor Tagging

In general, it is fairly easy to construct decay flavor taggers since the decay products of the B mesons are available for the construction. In this analysis we have identified as B decay products the tracks in the secondary vertex, including a high p_t lepton. We must use some property of one or more of these tracks in order to identify the flavor of a B^0 meson when it decayed. When a B^0 meson decays semi-leptonically, the b quark decays to a c quark and a charged W boson, which in turn decays to a lepton and a neutrino. The semi-leptonic decays of a B^0 and a \bar{B}^0 meson are depicted in Figure 3-1, in which we can see that a b quark always decays to a negative lepton while a \bar{b} quark always decays to a positive lepton. We therefore use the charge of the high p_t lepton in the secondary vertex as the decay flavor tagger.

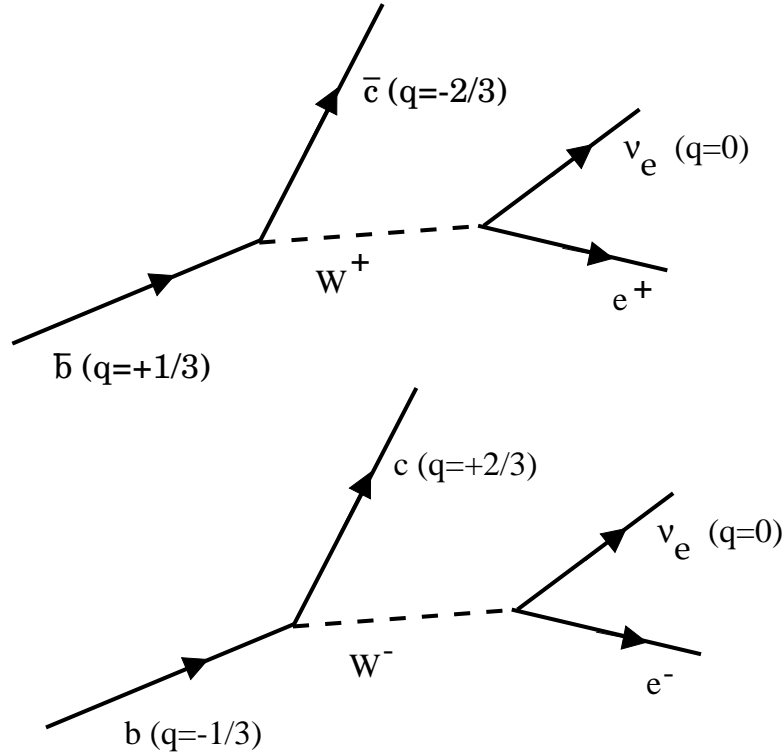


Figure 3-1: The charge of the charged lepton (in this case an electron) from a semi-leptonic b decay is correlated to the flavor of the b quark.

3.3.2 Production Flavor Tagging

It is much more difficult to determine the flavor of a B meson at the time of production since we are not able to directly probe a B at that time. Since no net flavor is produced from the primary interaction, there are two b quarks of opposite flavor in every B^0 event. It is important to distinguish between these two quarks when discussing production flavor tagging. We call the b quark which eventually decayed to the lepton whose track is part of the secondary vertex the “first b quark” and we call the other b quark in the event the “second b quark.” Production flavor taggers are used to determine the flavor of the first b quark.

There are fundamentally two approaches commonly taken to construct a production flavor tagger. The approach that we have taken in this analysis is to exploit the correlations between charged particles produced along with the B meson which contains the first b quark and the flavor of that B meson. Such correlations are expected [19] to arise from the process by which the first b quark becomes part of a B meson and from B^{**} decays. This approach is referred to as “Same Side Tagging” (SST).

The other approach to flavor tagging is to determine the flavor of the second b quark and to infer the production flavor of the first b quark from the fact that the two quarks are produced with opposite flavors. This approach is known as “Opposite Side Tagging” (OST). There are two common opposite side taggers. The Soft Lepton Tagger is simply the semi-leptonic decay flavor tagger described above applied to the second b quark. Jet Charge is a momentum weighted sum of the tracks in the jet containing the second b quark.

We give a general overview of Same Side Tagging and Opposite Side Tagging algorithms here, while we discuss the details of the SST algorithm we used in this analysis in Chapter 6.

Same Side Taggers

There are two sources for the correlations between the charge of some of the particles associated with the primary vertex and the production flavors of B mesons. One

source of this correlation comes from the decay of the B^{**} resonance. The $B^{**+} \rightarrow B^0 \pi^+$ and $B^{*-} \rightarrow \bar{B}^0 \pi^-$ decays will occur while the $B^{**+} \rightarrow \bar{B}^0 \pi^+$ and $B^{*-} \rightarrow B^0 \pi^-$ decays will not. Thus, there is a correlation between the charge of the π and the flavor of the B meson.

Another source of this correlation comes from the physics of fragmentation (sometimes called hadronization), the process by which free quarks form multi-quark bound states. During the fragmentation process of a b , quark-antiquark pairs are created by the color field. Some of these quarks will bind with the b quark to form a b hadron while the others will bind to each other forming other hadrons. Figure 3-2 shows a typical heavy quark hadronization into a meson. In the figure we can see a succession of produced hadrons starting with the one which contains the original heavy quark, Q , and continuing along with quarks produced successively later in the fragmentation process. This is called a fragmentation chain. In the SST algorithm we are interested in the first charged meson in the fragmentation chain of a $b \rightarrow B_d$ hadronization. Gronau, Nippe, and Rosner [19], observed that this first charged particle (usually

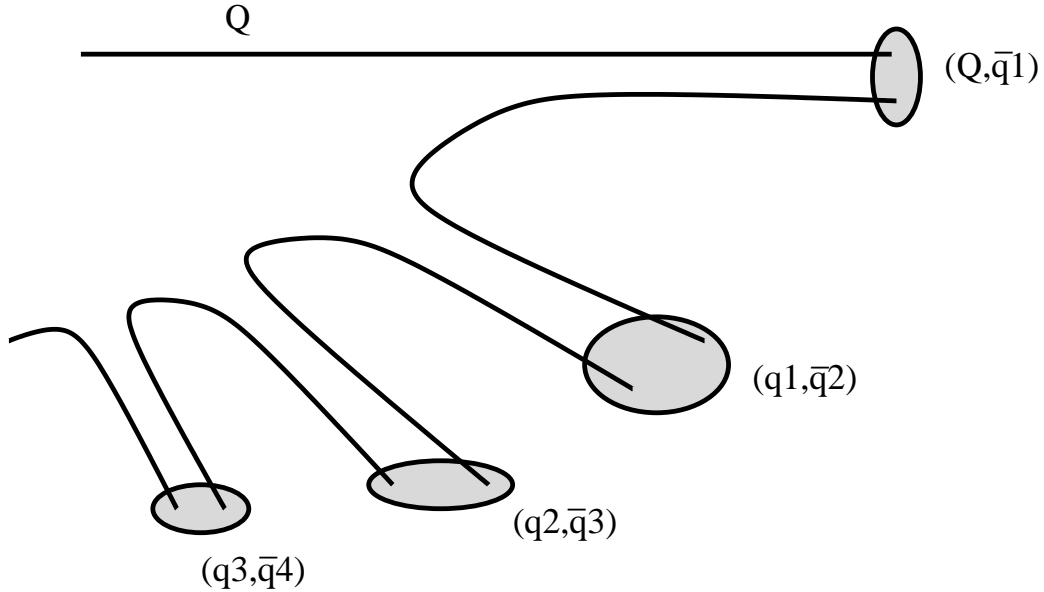


Figure 3-2: A fragmentation chain is produced during the hadronization of a quark, Q .

a pion) in the fragmentation chain is correlated to the charge of the b quark. For

example, a b quark that hadronizes into a \bar{B}^0 must pick up a \bar{d} quark from the fragmentation leaving a d quark to find it's own partner. If this d quark is to become part of a charged meson, that meson will be negative. Luckily this is the same correlation as that from the B^{**} decays and the two effects work in concert. Since the difference between the neutral and charged B meson is the flavor of the spectator quark, and the spectator quark determines the charge of the flavor-correlated charged meson, this correlation is reversed for B^+ relative to B^0 , as can be seen in Figure 3-3.

We exploit the correlation between the charge of charged hadrons that appear to come from the primary vertex and the flavor of B mesons associated with those mesons for the construction of a production flavor tagger used in this analysis.

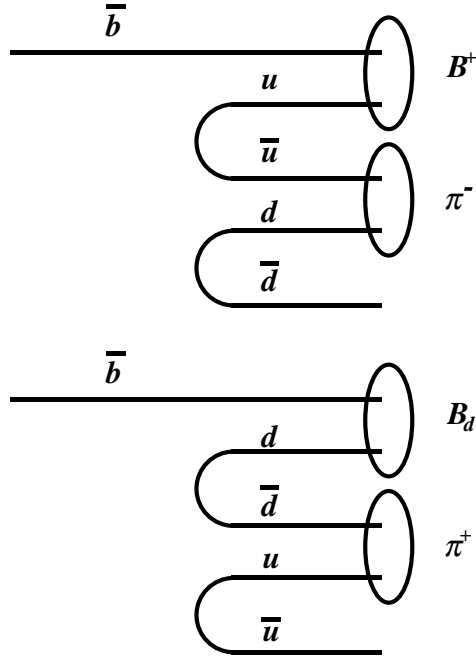


Figure 3-3: The fragmentation of a \bar{b} quark into neutral and charged B mesons. The charged pion produced as the first fragmentation particle have a charge that is correlated to the flavor of the B meson, with the correlation reversing sign depending on whether the \bar{b} quark hadronized into a B^0 or a B^+ .

There are reliable calculations of high momentum scattering production rates for

$b\bar{b}$ because the quarks are effectively free. However, reliable perturbative calculations of the fragmentation process do not exist because it is a low momentum transfer process and therefore the strong coupling constant is not small. Since the fragmentation time is much longer than the production time, the two physical phenomena can be decoupled theoretically. The production of b quarks (calculated perturbatively) is treated independently from the hadronization of b quarks, which is modeled phenomenologically. The fragmentation model ² developed by the Lund group [20] is commonly used for the simulation of the fragmentation process. The Monte Carlo studies we performed in this analysis used the Lund model to describe fragmentation. The Lund model is motivated by the observed fact that the angular momentum of mesons of similar quantum numbers are linearly related to the square of their masses. Such relationships are known as “Regge trajectories” [21]. A simple classical model in which a meson is treated as a rigid rotator exemplifies the model and produces a Regge trajectory. Figure 3-4 shows a massless quark and antiquark connected by a string of length d and tension k . The two quarks are rotating about the center-of-mass of the system at nearly the speed of light. The velocity, v , of a string element

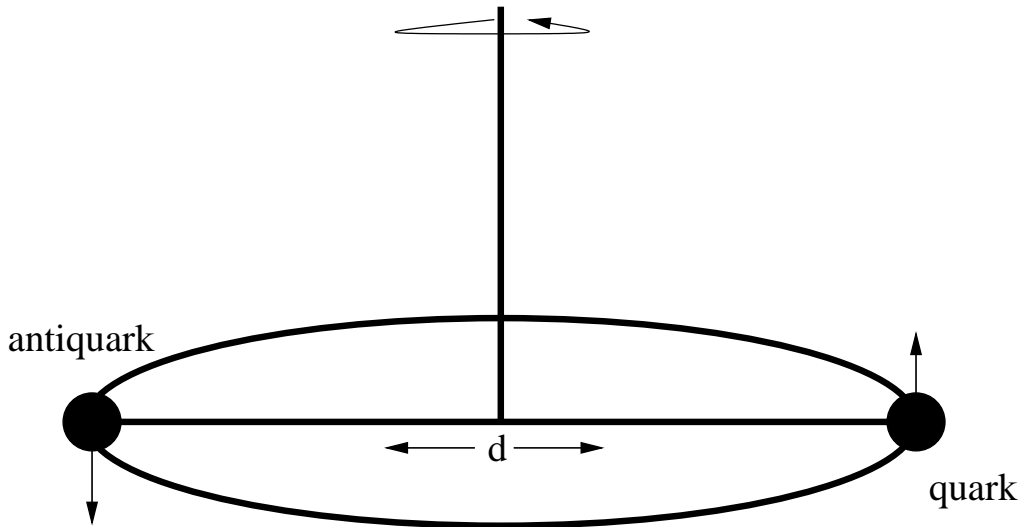


Figure 3-4: A classical rigid rotator model of a meson.

²Sometimes this model is called the 1+1 Dimensional String Model.

a distance r from the center is

$$v(r) = \frac{2r}{d}. \quad (3.1)$$

The mass of the system, M , is therefore given by

$$M = \int_0^{d/2} dr \frac{2k}{(1 - v(r)^2)^{1/2}} = \int_0^{d/2} dr \frac{2k}{(1 - (\frac{2r}{d})^2)^{1/2}} = \frac{\pi k d}{2}, \quad (3.2)$$

while the angular momentum, J , is given by

$$J = \int_0^{d/2} dr \frac{2k v r}{(1 - v^2)^{1/2}} = \frac{\pi k d^2}{8}. \quad (3.3)$$

We therefore find that $J \sim M^2$, as observed experimentally. We are thus motivated to think of the gluon field as a one dimensional energy density between the two quarks. A more sophisticated motivation can be found from an examination of the Wilson operator of QCD [22, 23]. A one dimensional string is a natural choice to describe the energy density in the color field between two quarks since the quarks interact via the exchange of gluons which are also colored and tend to pull the color lines of force together into a tightly bound tube or string.

The tension on the string, k , is determined to be roughly 1 GeV/fm from measured Regge trajectories as well as lattice QCD calculations. As two quarks fly apart the energy between them increases until there is enough energy to produce a quark-antiquark pair. At this point a new quark pair is produced and a string is stretched between them. As this process continues, more and more quarks are produced and these new quarks bind with the old ones to produce hadrons. This process is depicted in Figure 3-5. The Lund model has been very successful at reproducing the kinematic properties of fragmentation particles.

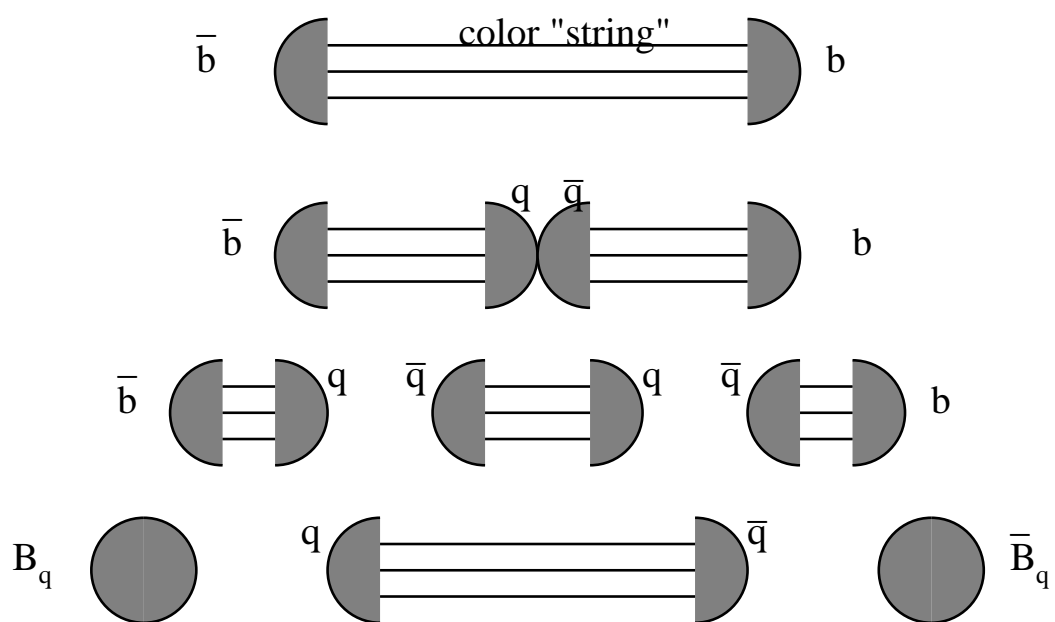


Figure 3-5: The hadronization of a heavy quark in the Lund model.

Opposite Side Taggers

In OST algorithms, the production flavor of the first b quark is inferred from the flavor of the second b quark. Figure 3-6 depicts the opposite side tagging possibilities. When the two b quarks are produced collectively at rest and have no net transverse

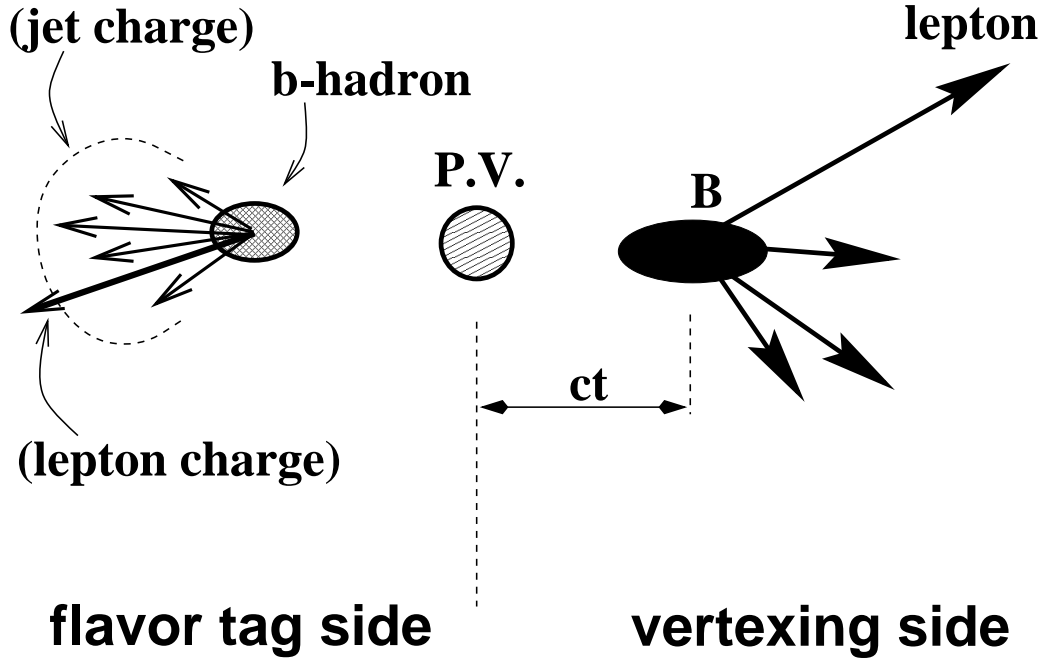


Figure 3-6: For OST algorithms, the flavor of the first b quark is inferred from the flavor of the second b quark.

momentum, they form “back-to-back” jets. The b quarks are in opposite hemispheres of the event, hence the name “opposite side tagging.” At CDF, there are two effects that tend to reduce the angle between the two b jets. The $b\bar{b}$ pair is in general not produced at rest but rather boosted along the z direction, closing the angle between the two jets in the lab frame. Furthermore, the next to leading order $b\bar{b}$ production processes provide roughly the same sized contribution to leading order production processes. Unlike leading order $b\bar{b}$ production processes, in the next to leading order processes the b and \bar{b} are not produced back-to-back since there is a gluon jet that can take some of the momentum from the event. An important consequence of the fact that the b jets are not back-to-back is that when one of the b jets is in the fiducial

region of the central part of the detector, the other is also in the fiducial region of the central part of the detector only $\sim 40\%$ of the time, reducing the opposite side tagging efficiencies. Another disadvantage of opposite side tagging is that when the second b quark fragments into a B_s^0 or B_d^0 , mixing of the second b meson dilutes the correlation between the two b quarks.

The Soft Lepton Tagging method has a low tagging efficiency due to the semi-leptonic branching fraction for B mesons. The soft lepton tagging correlation is also degraded by the potential for confusing semi-leptonic charm decays with semi-leptonic bottom decays.

The correlation between the production flavor of the first b quark and the jet charge may be degraded by the confusion of light quark jets or charged particles from the proton-antiproton remnants with the second b jet.

A significant advantage of opposite-side tagging is that the production flavor tagging performance is independent of the proper decay time of the B meson containing the first b quark.

3.3.3 Time-Integrated Measurements

It is possible to determine Δm_d by measuring the total fraction of B^0 mesons that mixed before decaying. This only requires the three basic ingredients of a mixing measurement: finding B^0 mesons, measuring the decay flavor, measuring the production flavor. The probability that a B meson mixes before decaying is shown in Equation 1.20. The total fraction, χ_d , of B mesons that mix before decaying is given by integrating this distribution:

$$\chi_d = \int dt \frac{\Gamma}{2} e^{-\Gamma t} (1 - \cos \Delta m_d t). \quad (3.4)$$

The value of Δm_d can be extracted from χ_d :

$$\chi_d = \frac{(\Delta m_d / \Gamma)^2}{2[1 + (\Delta m_d / \Gamma)^2]}. \quad (3.5)$$

A number of experiments [24] have been performed in which the mixing probability is averaged over time. When B mesons are produced at rest, it is not possible to

measure the proper time of decay and Δm_d must be extracted from χ_d . However, when the proper time is available, a statistically more precise measurement can be made. In our case, a time dependent measurement simply improves the accuracy of the determination of the mixing frequency, but when trying to determine the mixing frequency of the B_s , a time dependent measurement is essential. This is because the B_s mixing frequency is large ($\Delta m_s > 9.1 \text{ (ps)}^{-1}$ [4]), and thus χ_s is about 0.5. In this case the time-integrated fraction of mixed events is not very sensitive to the mixing frequency.

3.3.4 The Time Dependent Mixing Asymmetry

The B mesons at CDF are not produced at rest, and we can measure the proper time difference between the decay and production of a B meson. We can therefore perform a proper time dependent extraction of Δm_d . The probability densities for finding a mixed (ρ_m) and unmixed (ρ_u) B meson at a proper time t are given by

$$\rho_m = \Gamma e^{-\Gamma t} (1 - \cos \Delta m_d t) \quad (3.6)$$

$$\rho_u = \Gamma e^{-\Gamma t} (1 + \cos \Delta m_d t). \quad (3.7)$$

The “mixing asymmetry” is defined as

$$A \equiv \frac{\rho_u(t) - \rho_m(t)}{\rho_u(t) + \rho_m(t)} = \cos \Delta m_d t. \quad (3.8)$$

In this analysis we extract the value of Δm_d from the time dependence of the mixing asymmetry. There are a few complications that arise in this procedure:

- The production and decay flavor taggers do not always identify the flavor of the B meson correctly.
- The proper time of decay is not determined with perfect accuracy.
- There are secondary vertices that are not due to B^0 decays in the event sample.

We describe how each of these complications are dealt with in this analysis.

Imperfect Flavor Taggers

In order to construct the mixing asymmetry, we need to measure the number of neutral B mesons that mixed before decaying as a function of the proper time of the decay. Because the decay and production flavor taggers occasionally give an incorrect identification of the flavor of a B , we can only measure a parameter proportional to the mixing asymmetry rather than the mixing asymmetry directly. We define a “positive correlation event” to be an event in which the production flavor tagger and the decay flavor tagger agree about the flavor of the b quark. Conversely, a “negative correlation event” is one in which the production and decay flavor taggers disagree. The best estimate for the number of events that mixed at a particular proper time is given by the number of negative correlation events (N) while the best estimate for the number of events that did not mix is given by the number of positive correlation events (P). The measured mixing asymmetry is given by

$$A^{meas} = \frac{P - N}{P + N}. \quad (3.9)$$

Our production flavor tagger has some probability p_w^{SST} of being wrong when assigning the production flavor. The decay flavor tagger also has a probability p_w^{lep} of getting the decay flavor wrong. We can relate the number of mixed, M , and unmixed, U , neutral B mesons to the number of positive correlation and negative correlation events as follows:

$$\begin{aligned} P &= [(1 - p_w^{SST})(1 - p_w^{lep}) + p_w^{SST} p_w^{lep}]U + [p_w^{SST}(1 - p_w^{lep}) + p_w^{lep}(1 - p_w^{SST})]M \\ N &= [(1 - p_w^{SST})(1 - p_w^{lep}) + p_w^{SST} p_w^{lep}]M + [p_w^{SST}(1 - p_w^{lep}) + p_w^{lep}(1 - p_w^{SST})]U. \end{aligned} \quad (3.10)$$

The measured asymmetry is thus

$$A^{meas} = (1 - 2p_w^{SST})(1 - 2p_w^{lep}) \cos \Delta m_d t. \quad (3.11)$$

We can see that the amplitude of the oscillation is reduced by the mistag rates for production and flavor tagging. We define the production flavor and decay flavor

dilutions as

$$D_{SST} = 1 - 2p_w^{SST} \quad (3.12)$$

$$D_{lep} = 1 - 2p_w^{lep}, \quad (3.13)$$

so that the measured asymmetry is expressed as

$$A^{meas} = D_{SST} D_{lep} \cos \Delta m_d t. \quad (3.14)$$

If the mistag probabilities were $\frac{1}{2}$ (the worst flavor tagger possible is one which selects the flavor at random - succeeding $\frac{1}{2}$ of the time), then the dilutions would be 0.0 and there would be no measured asymmetry and thus nothing from which to extract Δm_d . In this analysis we determine the decay flavor tagging dilution from the sample composition of the data, while we measure the production flavor tagging dilution simultaneously with the measurement of Δm_d .

The Proper Time Resolution

The proper time of decay for a B meson can be determined from the velocity of the meson, the boost, and distance between the primary vertex, where the B meson was produced, and the secondary vertex, where the B meson decayed. Because of the detector design and the fact that there is an unknown boost for each event in the z direction, we only have physical quantities transverse to the beam axis at our disposal in reconstructing the proper time of decay. We call the distance traveled by the B meson in the transverse ($r - \phi$) plane L_{xy} . Figure 3-7 shows a sketch of the definition of this variable. We can express the proper time of decay in terms of L_{xy} and the transverse momentum of the B meson. If the total distance in three dimensions between the primary vertex and the secondary vertex is L_{xyz} and the particle has a velocity v and boost γ , then the proper decay time is simply $\frac{L_{xyz}}{\gamma v}$. Multiplying the numerator and denominator by $\sin \theta$ where θ is the angle between the vector pointing from the primary vertex to the secondary vertex and the z -axis, we get

$$t = \frac{L_{xy} M_B}{p_t(B)}, \quad (3.15)$$

where M_B is the mass of the meson, $p_t(B)$ is the transverse projection of the momentum of the B , and we have used the relationship $p = M_B v \gamma$. Unfortunately we can not determine L_{xy} and $p_t(B)$ with perfect accuracy. We distinguish the measured transverse distance L_{xy}^{meas} from the true quantity L_{xy} with a superscript on the variable. The measured proper time can differ from its true value for a variety of reasons, including the inclusion of tracks not associated with the B in the secondary vertex, a large flight distance of the D from a B decay, the lack of inclusion of some of the decay products of the B , and most importantly, an imperfect reconstruction of the tracks in the event. We don't know the momentum of the B , $p_t(B)$, sufficiently well either. Since we do not do a reconstruction of the B in this analysis, we don't know with any certainty, other than for the tracks in the secondary vertex itself, which tracks correspond to daughters of the B decay. We take the momentum of the B jet projected into the transverse plane, $p_t(jet)$, as an approximation for $p_t(B)$. In terms of these measured quantities we can define the pseudo-proper time, t' as

$$t' = \frac{L_{xy}^{meas} M_B}{p_t(jet)}. \quad (3.16)$$

The pseudo-proper time is the best estimate for t using only measured quantities. The mixing probability distributions shown in Equation 3.7 and the asymmetry in Equation 3.14 are functions of the proper time but we can only measure functions of the pseudo-proper time. We therefore need to relate functions of the proper time to functions of the pseudo-proper time. We use the Monte Carlo to determine the convolution functions that relate the expected asymmetry as a function of proper time, t , to the expected asymmetry as a function of pseudo-proper time, t' .

Background Particle Species

So far we have only discussed the asymmetry due to B^0 mesons. The b quark may also hadronize into other b hadrons. In some cases the event is really a $c\bar{c}$ event which has been mis-identified as a $b\bar{b}$ event. The asymmetries due to these other particle

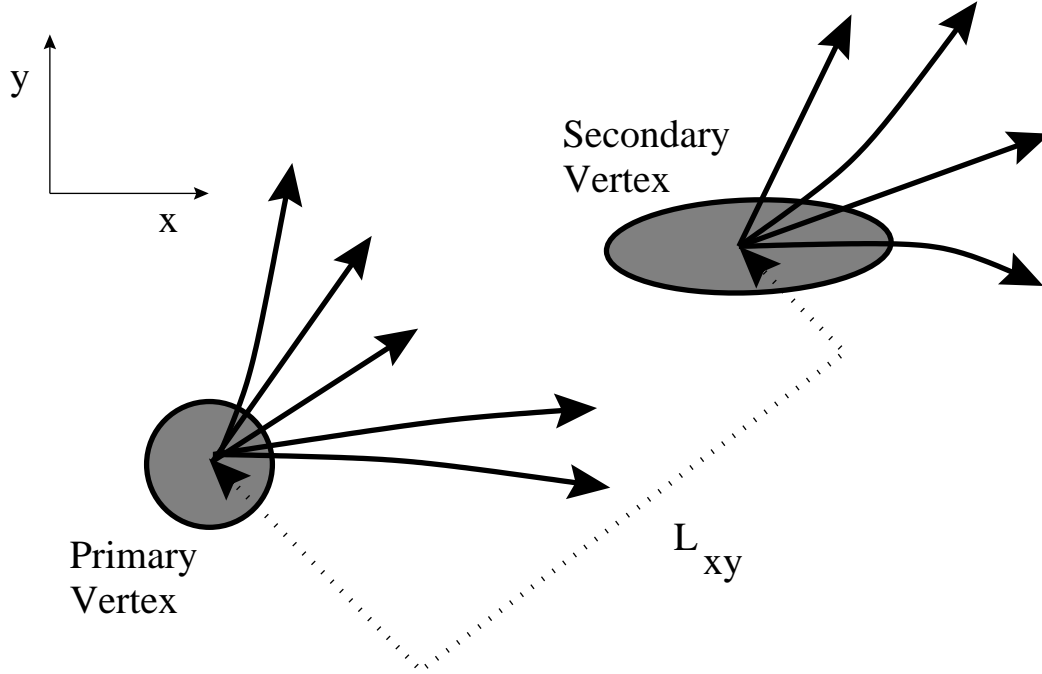


Figure 3-7: L_{xy} is the distance between the primary vertex (where the B meson is produced) and the secondary vertex (where the B meson decayed) in the transverse plane.

species are much simpler since they do not mix.³ We measure the production flavor tagging dilution for B^0 and B^+ directly in the data, and we use the Monte Carlo for the determination of the flavor tagging dilution for the other particle species on which we tag. The procedure for doing this will be discussed in detail in Chapter 7. For each particle species we compute a positive correlation probability density function $\rho_P^{particle}$ and a negative correlation probability density function $\rho_N^{particle}$. The overall probability density functions are then

$$\rho_P(t') = \sum_{particle} \rho_P^{particle} f_{particle} \quad (3.17)$$

$$\rho_N(t') = \sum_{particle} \rho_N^{particle} f_{particle}, \quad (3.18)$$

³The B_s oscillates as well, but with a period that is small compared to the proper time binning, thus averaging out over any given bin. The D^0 also oscillates, but very slowly on our time scale.

where $f_{particle}$ is the fraction of Secondary vertices that are due to the decay each particle species. We define the χ^2 to be:

$$\chi^2 = \sum_i \frac{(\frac{\rho_P(t'_i) - \rho_N(t'_i)}{\rho_P(t'_i) + \rho_N(t'_i)} - A_i^{meas})^2}{\sigma_i^2} \quad (3.19)$$

where σ is the error on the measured asymmetry and the sum is over pseudo-proper time bins for the electron and muons samples. We minimize this χ^2 with respect to the parameters we wish to determine (including Δm_d).

3.4 A Note About SST Algorithms Used with Inclusive Lepton Data

Since we do not reconstruct the decays of the B mesons in our sample, there are B daughter tracks which have not been included in the secondary vertices and therefore are not identified with the B meson decays. Such tracks, having come from the decays of B mesons, can have no information about the production flavor of B mesons. These tracks will appear to have come from the primary vertex and are likely to be mistaken for the intended SST charged tracks. When the rate of such mistakes is high, there is a substantial degradation of the flavor tagging power of the SST algorithm. It is therefore important to find ways to distinguish such missed B daughter tracks from primary tracks and thus to keep them from contributing to the determination of the production flavor. We do this by identifying track properties which are sufficiently different for these two classes of tracks and compute the probability, as a function of these track properties, of being a missed B daughter for every track in the event. Only those tracks with a small probability of being a B daughter are used in the determination of the production flavor.

3.5 Summary of Methods in This Analysis

The main ingredients to this mixing measurement are:

- Identify $b\bar{b}$ events by finding secondary vertices with high p_t leptons.
- Determine the production flavor of a B meson by using a form of the same-side tagging method.
- Determine the decay flavor of a B meson by exploiting the correlation between the charge of the lepton from semi-leptonic decays of the B and the decay flavor of the B .
- Reconstruct the proper time of the decay using the L_{xy}^{meas} , $p_t(jet)$ and a Monte Carlo simulation.
- Compute the expected asymmetry due to B^0 mesons and backgrounds as a function of t' and find the Δm_d which minimizes the χ^2 function shown in Equation 3.19.

Chapter 4

Data and Monte Carlo Samples

In this chapter we describe the event selection criteria applied to the data and the determination of the sample composition. The Monte Carlo sample used in this analysis is also described.

The data sample consists of events in which a secondary vertex that includes a high p_t lepton has been reconstructed. We present the lepton selection criteria in section 4.1. Next, we describe the secondary vertex finding algorithm in section 4.2. In section 4.3 we discuss the Monte Carlo samples which are used throughout this analysis. Finally, in sections 4.4-4.8, we present the determination of the sample composition, which is done in part with the use of the Monte Carlo samples.

4.1 Lepton Selection Criteria

We call the highest p_t lepton candidate in an event the trigger lepton, since most of the time this is the track which satisfied the inclusive lepton trigger requirements. We used the trigger lepton to seed the b jet finding algorithm. Secondary vertices were searched for inside of candidate b jets. We say that a track is a member of a secondary vertex if it is one of the tracks used by the vertexing algorithm to define the secondary vertex. The trigger lepton was required to be a member of the secondary vertex.

4.1.1 Electron Selection Criteria

The signature of an electron is a CTC track which points to a shower in the electromagnetic calorimeter. We required that the electron candidates be within the fiducial volume of the SVX, since they are required to be a member of a secondary vertex. We also made kinematic requirements based on the transverse momentum, p_t , transverse energy, E_t (the energy in the calorimeters weighted by $\sin\theta$ of the calorimeter tower), and the ratio of hadronic to electromagnetic energy, $\frac{E_{had}}{E_{em}}$ (since electrons shower in the electromagnetic calorimeter and not in the hadronic calorimeter). In addition to these kinematic requirements, the transverse profiles of the shower shapes in the central electromagnetic calorimeter are required to be consistent with the expectations based on test-beam measurements of known electrons. Finally, the electron track is required to extrapolate into the center of the electromagnetic shower. Electron candidates were required to satisfy the following requirements:

- $p_t > 6.0$ GeV,
- $E_t > 7.5$ GeV,
- $\frac{E_{had}}{E_{em}} < 0.04$,
- Shower Profile matches test-beam electrons profiles, as measured by a χ^2 comparison,
- Δz between extrapolated track and shower wire < 3.0 cm,
- Δx between extrapolated track and shower wire < 1.5 cm.

4.1.2 Muon Selection Criteria

The signature of a muon is a reconstructed CTC track that extrapolates into the muon chambers close to the hits in those chambers, consistent with errors in the track parameters and deflections of the muon path due to multiple scattering. Muons candidates must be within the SVX fiducial volume and to have hits in the CMU and in the CMP chambers. The only kinematic requirement on the muon candidate is

applied to the transverse momentum. Muon candidates were required to satisfy the following:

- $p_t > 6.0$ GeV,
- Muon candidates are required to have hits in the Central Muon Chamber (CMU),
- Muon candidates are required to have hits in the Central Muon Upgrade Chamber (CMP),
- The CTC track extrapolates to the CMU hits,
- The CTC track extrapolates to the CMP hits.

4.2 Secondary Vertex Finding

Once a trigger lepton was identified, we looked for secondary vertices that included the trigger lepton. The algorithm [25] that we used to find secondary vertices looks within candidate B jets for sets of tracks which form a vertex that is significantly displaced from the primary vertex. The first step toward finding secondary vertices is therefore to find candidate B jets. For our purposes, a jet is a collection of tracks directed in the same solid area region. The measure of solid angle that we use is $\Delta R = \sqrt{\Delta\eta^2 + \Delta\phi^2}$. Note that by using this definition the solid angle is invariant with respect to boosts in the z direction. Tracks that are within ΔR of an axis are said to fall within a cone of radius ΔR about that axis. Figure 4-1 is a depiction of a ΔR cone about a jet axis, the vector sum of the momenta of the tracks which comprise the jet. The jet finding algorithm [26] iteratively merges candidate jets until all jets are separated in ΔR . In this analysis we used cones with a radius of 1.0 to define jets. The initial seeds for the jets are single tracks with $p_t > 1$ GeV/c. The merging proceeds from the highest to the lowest p_t tracks, starting with trigger lepton. Once the iterative merging is complete, lower p_t tracks are added to jets according to the

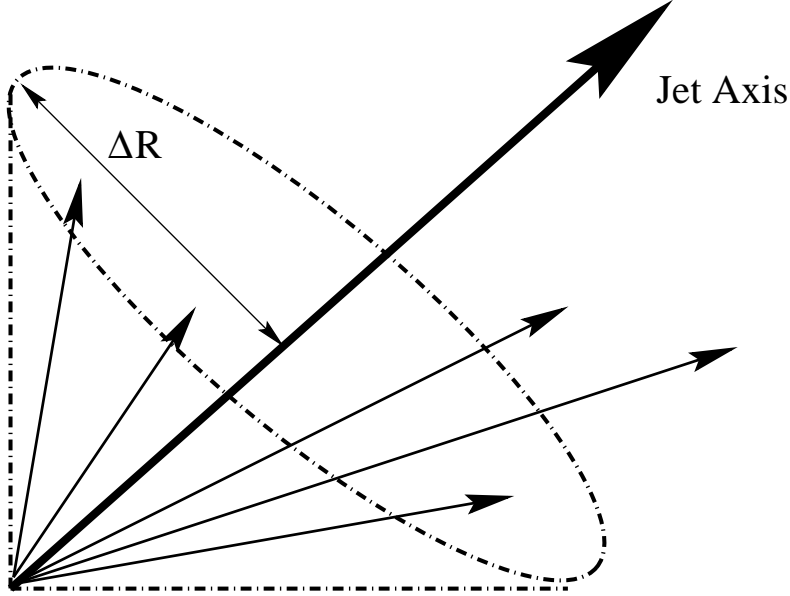


Figure 4-1: The tracks in a jet are all inside a cone defined by the jet axis and ΔR .

cones in which the low p_t tracks fall within. All tracks in a jet are required to have a transverse momentum of at least 400 MeV/c.

Once we had candidate B jets we looked for secondary vertices in the jet which contained the trigger lepton. The secondary vertex algorithm applies two passes to the jet. In the first pass, it looks for vertices with three or more tracks while in the second pass it looks for vertices with two tracks. In either case the trigger lepton is required to be one of the tracks in the vertex. The distance in the transverse plane between a track and the primary vertex at the point of closest approach, the impact parameter with respect to the primary vertex, is a useful quantity when distinguishing primary from secondary tracks. This quantity, d_{pv} , is depicted in Figure 4-2. The error on the impact parameter with respect to the primary vertex, σ_{pv} , is largely determined from the SVX resolution. Every track in the secondary vertex must have an impact parameter significance, d_{pv}/σ_{pv} , of at least 2.0. Tracks are added to a secondary vertex only if they are inside a cone with a radius of $\Delta R = 0.7$ of the vector pointing from the primary vertex to the secondary vertex. In the first pass, tracks with at least 500 MeV/c are considered for vertexing while for the second pass, only tracks with at least 750 MeV/c are allowed to be a part of the vertex. Note that since the trigger lepton

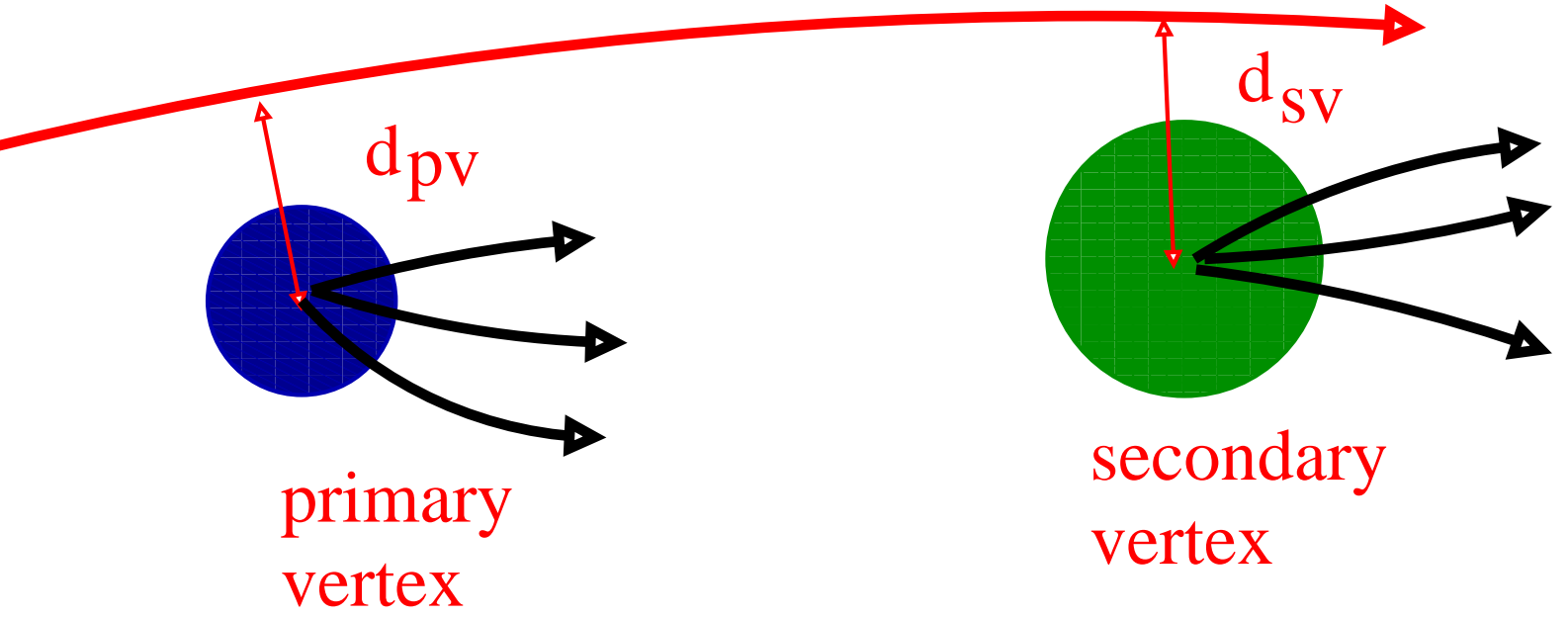


Figure 4-2: The impact parameter, d_{pv} , is the distance of closest of approach to the primary vertex.

is required to be in the secondary vertex, at least one of the tracks has a transverse momentum of at least 6 GeV/c. We required the L_{xy} significance, $L_{xy}/\sigma_{L_{xy}}$, to be at least 1.5. We also required the L_{xy} to be at least 1.2 mm. The decays of K_s mesons and Λ baryons were removed from the sample of vertex candidates. Both particles decay to two oppositely charged tracks: $K_s \rightarrow \pi^+\pi^-$, $\Lambda \rightarrow p\pi^-$. A track is considered part of a K_s or Λ vertex if it forms a vertex with an oppositely charged track that has a mass consistent with the K_s (within 10 MeV/c) or Λ (within 6 MeV) mass. Tracks that are considered part of a K_s or Λ decay are not considered by the vertex finding algorithm.

When the secondary vertex consists of all of the daughters from a B decay, the invariant mass of the vertex equals the B mass. The neutral daughters of the B do not leave tracks, however, and some of the daughter tracks are not part of the vertex so in general the invariant mass of the vertex will be less than the B mass. We define the “secondary vertex mass” to be the invariant mass of the tracks in the secondary vertex assuming each track corresponds to a particle with the pion mass

and 3-momentum \vec{p}_i :

$$M_{vertex}^2 = \left(\sum_i (m_\pi^2 + \vec{p}_i \cdot \vec{p}_i)^{\frac{1}{2}} \right)^2 - \left(\sum_i \vec{p}_i \right) \cdot \left(\sum_i \vec{p}_i \right). \quad (4.1)$$

We required $M_{vertex} < M_B$. After applying these requirements we found 59881 B candidates with a semi-leptonic electron decay and 63674 candidates with a semi-leptonic muon decay.

4.3 Monte Carlo Samples

The Monte Carlo was used in several aspects of this analysis. The fraction of prompt charm in the electron and muon inclusive lepton data samples are determined from the Monte Carlo shapes of the secondary vertex mass distributions for prompt charm and bottom events. The resolution of the observed proper time, depending on the L_{xy} resolution and the estimation of the transverse momentum of the B via the measurement of the transverse momentum of the B jet, is also determined from Monte Carlo. Furthermore, the fraction of trigger leptons due to sequential decays of the b quark is determined from the Monte Carlo. The model of SST tagging of B daughters is based on Monte Carlo results. Finally, the SST algorithm was optimized using Monte Carlo studies, but the performance of the algorithm is measured in the data.

We used version 5.7 of the Pythia Monte Carlo [20] to generate inclusive lepton bottom and charm samples. The Lund string model is used to simulate fragmentation by this generator. Several parameters used in Pythia were tuned [27] so that distributions related to B fragmentation generated by the Monte Carlo matched those measured at CDF. These data/Monte Carlo comparisons were done in a reconstructed $B^+ \rightarrow \nu l^+ \bar{D}^0, D^0 \rightarrow K^+ \pi^-$ sample. The tracks in the event were separated into “near” and “far” regions with respect to the B decay. Tracks in a cone of radius 1.0 about the vector sum of the momenta of the tracks identified with the B decay by a reconstruction algorithm were considered to be near tracks while tracks outside of this cone were considered far region tracks. Tracks in the far region are predominately

due to the underlying event while tracks in the near region are due to the underlying event or the B jet.

First, in the far region, the p_t and track multiplicity as a function of $\Delta\phi$ (between the track and the reconstructed B momentum vector) distributions were tuned. Once these underlying event distributions were modeled well, the multiplicity in the near region was tuned. This tuning process was iterated until the distributions from the Monte Carlo matched the data in both the near and far regions. Results of this tuning can be seen in reference [27].

Hadrons decays were simulated using the QQ Monte Carlo [28] which uses ISGW** [29] matrix elements to model semi-leptonic heavy flavor decays.

We used the QFL' CDF detector simulation [30] to simulate the detector response to generated events. Tracks in the CTC are created by smearing generated particle paths by parameterized resolution functions. A better tracking generation model is used for the SVX in which hits are simulated and the standard SVX pattern recognition algorithm is deployed to reconstruct tracks.

In order to ensure similar kinematics between the Monte Carlo and the data, we re-weighted Monte Carlo events in such a way as to reproduce the data trigger lepton p_t distribution, as shown in Figures 4-3. The weights were determined by taking the ratio of histograms of the lepton p_t distributions of data to Monte Carlo results and using a look-up table based on the p_t bin that a trigger lepton fell into. The shape of the lepton p_t spectrum was sculpted on the basis of the p_t dependence of the inclusive lepton trigger efficiencies, which is difficult to model in the Monte Carlo.

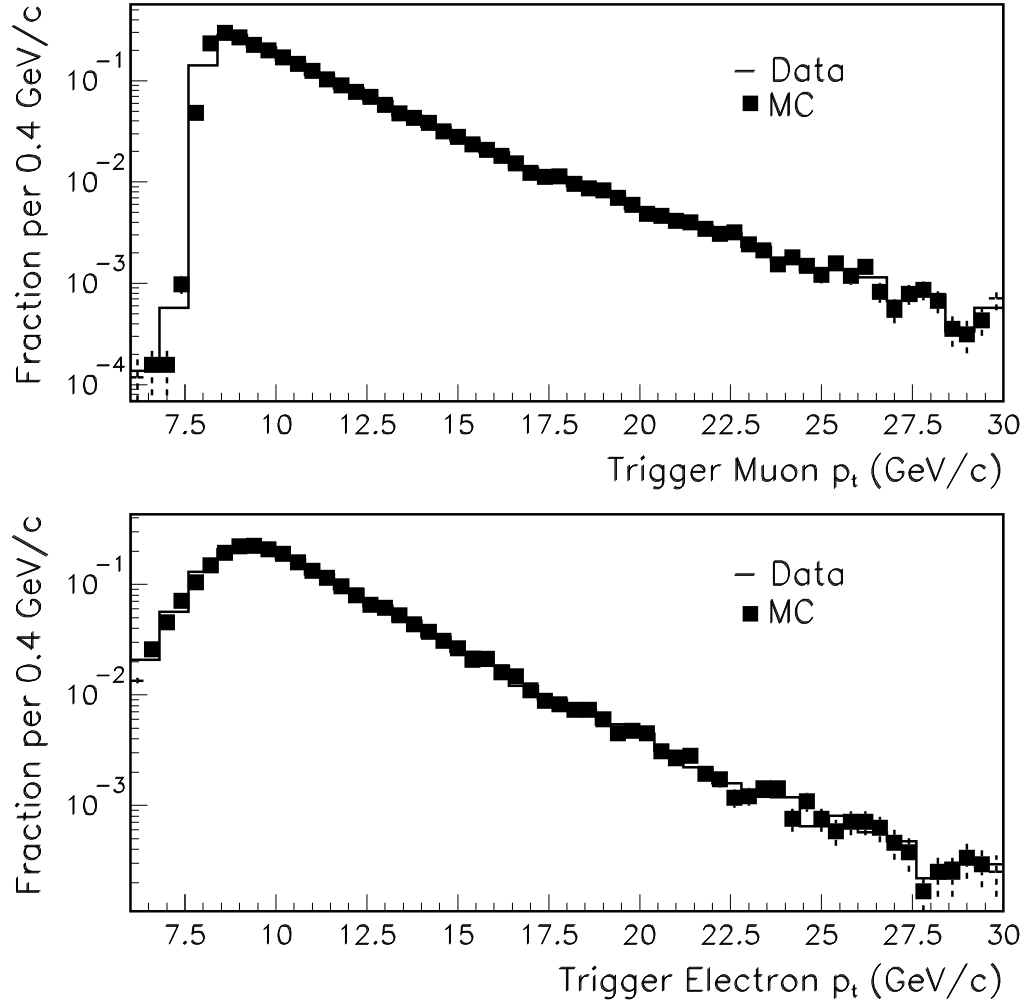


Figure 4-3: Comparison between Monte Carlo and data of the muon p_t (top) electron p_t (bottom) after weighting (they are forced to agree).

4.4 Fake Electron Trigger Fraction

Some of the trigger electrons are actually hadrons that pass the electron selection criteria. We can determine the fraction of trigger electrons candidates that are not real electrons by fitting the ionization energy loss, $\frac{dE}{dX}$, distribution for the electron, pion, kaon, and proton fractions.

As mentioned in section 2.3.6, the most probable value of energy loss due to ionization for a charged particle is a function of the velocity of the particle. A simultaneous measurement of the $\frac{dE}{dX}$ (and thus velocity) and the momentum of a particle provides a determination of the mass of the particle and hence a particle identification. Figure 4-4 shows the expected value of energy loss, as measured in nanoseconds¹ for electrons, pions, muons, kaons, and protons as function of momentum. The average separation, in $\frac{dE}{dX}$, between electrons and hadrons for the trigger electron p_t spectrum are as follows:

$$\left\langle \frac{\frac{dE}{dX}_e - \frac{dE}{dX}_\pi}{\sigma} \right\rangle = 0.7 \quad (4.2)$$

$$\left\langle \frac{\frac{dE}{dX}_e - \frac{dE}{dX}_K}{\sigma} \right\rangle = 1.7 \quad (4.3)$$

$$\left\langle \frac{\frac{dE}{dX}_e - \frac{dE}{dX}_p}{\sigma} \right\rangle = 2.3, \quad (4.4)$$

where $\frac{dE}{dX}_e, \frac{dE}{dX}_\pi, \frac{dE}{dX}_K$, and $\frac{dE}{dX}_p$ are the $\frac{dE}{dX}$ values for electrons, pions, kaons, and protons respectively. These separations are large enough to distinguish the electron fraction from the other components.

For each trigger electron we determined the $\frac{dE}{dX}$ for the track as well as the expected $\frac{dE}{dX}$ under the hypotheses that the track belongs to an electron, pion, kaon, and proton. Since the electron candidate does not have hits in the muon chambers and since the muon and pion $\frac{dE}{dX}$ distributions are so similar, we do not include a muon component. The probability of observing $\frac{dE}{dX}_i$ for the i^{th} event is given by

$$\rho\left(\frac{dE}{dX}_i\right) = \sum_p \rho\left(\frac{dE}{dX}_i; p\right) f_p, \quad (4.5)$$

¹ $\frac{dE}{dX}$ is determined from the digital pulse width between leading and trailing edge times for CTC hits in superlayers three through eight.

where $\rho(\frac{dE}{dX_i}; p)$ is the probability of finding $\frac{dE}{dX_i}$ given the track is a particle of type p and f_p is the fraction of events due to particle p . The probability $\rho(\frac{dE}{dX_i}; p)$ is given by

$$\rho\left(\frac{dE}{dX_i}; p\right) = \frac{e^{(\frac{dE}{dX_i} - \frac{dE}{dX}|_p)^2 / 2\sigma_i^2}}{\sqrt{2\pi\sigma_i^2}}, \quad (4.6)$$

where $\frac{dE}{dX}|_p$ is the expected $\frac{dE}{dX}$ under the hypothesis that the track corresponds to a particle of type p and σ_i is the width on the expected value. We modify Equation 4.5 so that we can fit for the total number of events as well by releasing the condition that $\sum_p f_p = 1$ and replacing it with $n = N \sum_p f_p$ where n is the number of fit events and N is the number of observed events. Then we have

$$\rho\left(\frac{dE}{dX_i}\right) = \frac{\sum_p \rho(\frac{dE}{dX_i}; p) f_p}{\sum_p f_p}, \quad (4.7)$$

and we have for the likelihood

$$\mathcal{L} = \frac{N^n e^{-N}}{n!} \prod_i \rho\left(\frac{dE}{dX_i}\right). \quad (4.8)$$

We minimized $-\log \mathcal{L}$ to determine the particle fractions. We required that the number of CTC hits be greater than 24 in order to ensure that the distributions are properly Gaussian (to eliminate the tails). We find that the non-electron components to the fit is extremely small:

$$f_{fake}^e = 0.004 \pm 0.002. \quad (4.9)$$

Figure 4-5 shows the $(\frac{dE}{dX_i} - \frac{dE}{dX_p})/\sigma_i$ distribution for all of the trigger electrons with a central Gaussian super-imposed.

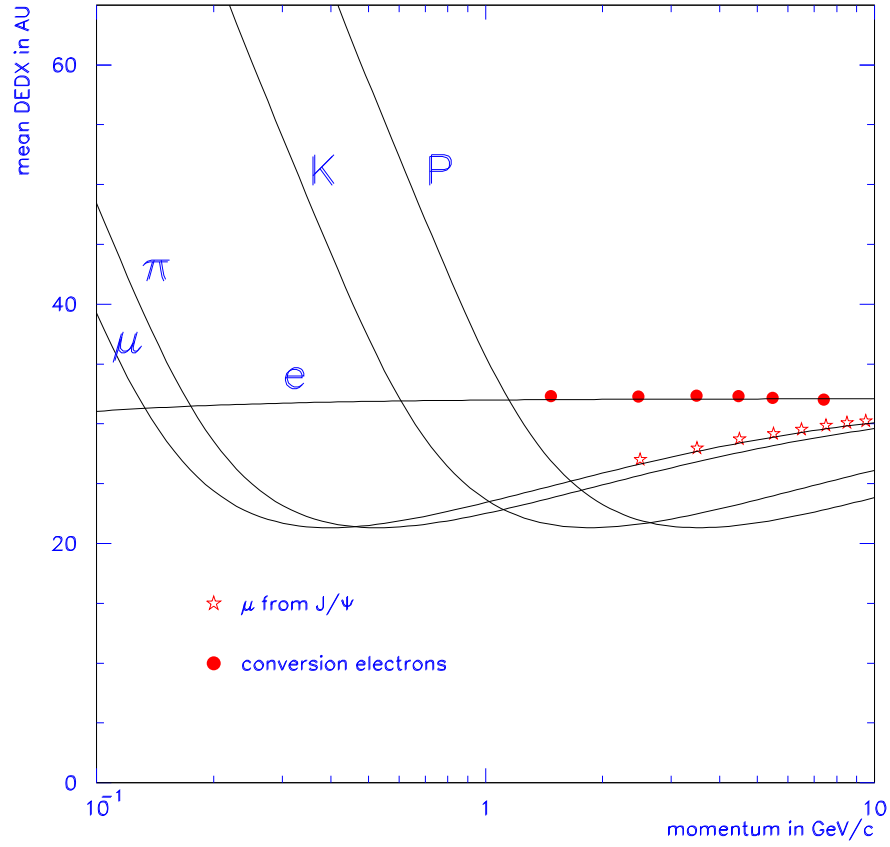


Figure 4-4: The expected $\frac{dE}{dX}$ as a function of track momentum for muons, pions, electrons, kaons, and protons.

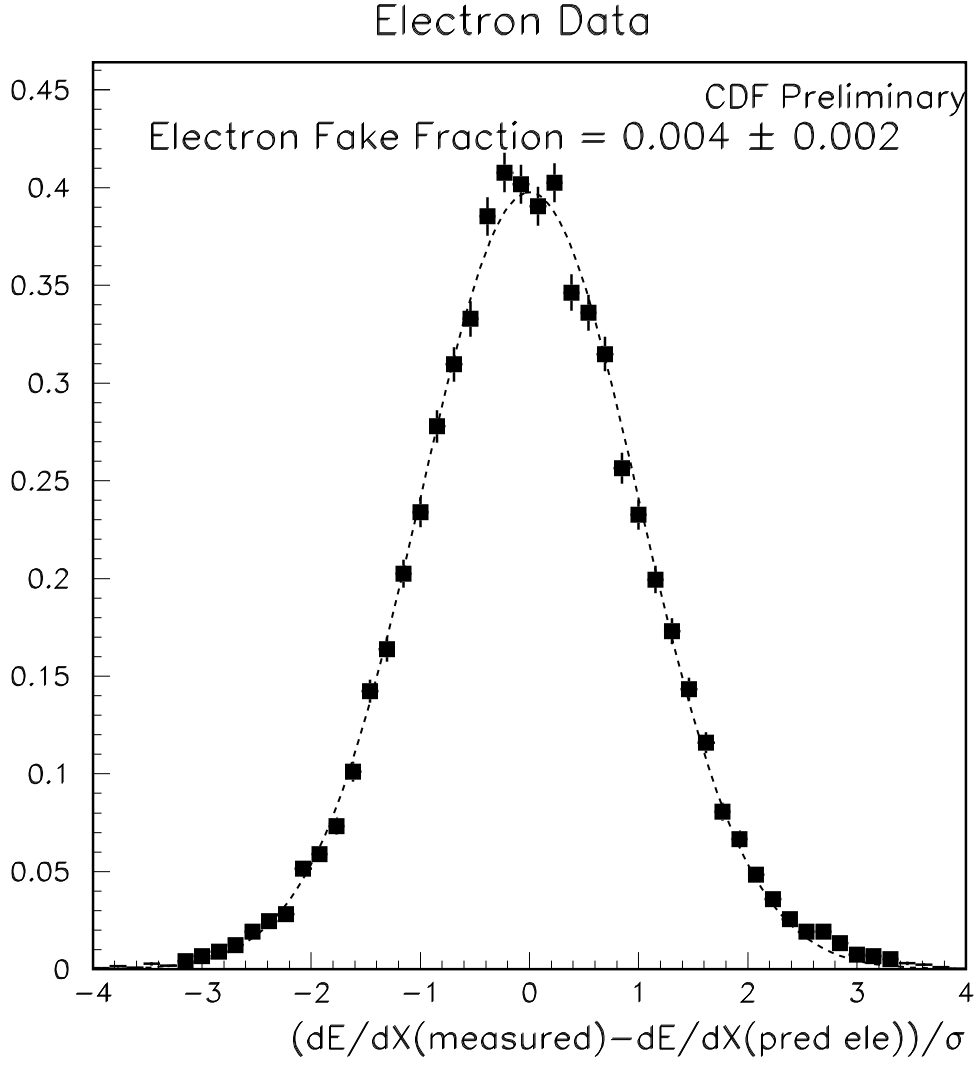


Figure 4-5: The $(\frac{dE}{dX}_i - \frac{dE}{dX}_e)/\sigma_i$ distributions for the trigger electrons, with a central Gaussian corresponding to the electron contribution super-imposed.

4.5 Electron Conversion Fraction

A fraction of the trigger electrons are actually electrons from photon conversions ($\gamma \rightarrow e^+e^-$) rather than heavy flavor decays. Figure 2-11 is the Feynman diagram for photon conversions. We can determine the fraction of electron conversions by searching for a conversion partner for each trigger electron. Conversion partners can be identified by the fact that conversion pairs come from a massless particle (a photon) and thus there should be no opening angle between the tracks. At the point of conversion, the two tracks should just barely touch. In order to find all of the conversions pairs for which the trigger lepton's conversion partner is reconstructed, we use very loose requirements on the conversion partner.

In this case, most of the conversion partners are really combinatorially dominated hadrons rather than electrons. We use the $\frac{dE}{dX}$ spectrum for the partner candidates to identify the fraction that are really electrons. If we were fully efficient at reconstructing tracks then the ratio of the total number of conversions to the number of conversion candidates would simply be the electron fraction found by fitting the $\frac{dE}{dX}$ spectrum. We are not, however, fully efficient at reconstructing low p_t tracks, and we must correct for this inefficiency, which we do using a method similar to that found in reference [31]. We estimate the efficiency for reconstructing low p_t conversion partners by fitting the p_t spectrum at high p_t to an exponential distribution. We assume that the p_t distribution at low p_t is also governed by this exponential and compute the efficiency from the data p_t distribution.

Every track in the event is tested for the hypothesis that the track and the trigger electron form a conversion pair. A track is accepted as a conversion pair candidate if the following conditions are met:

- $r\text{-}\phi$ Separation at tangent point < 0.5 cm,
- $\Delta\cotan(\theta) < 0.06$,
- z Mismatch at tangent point < 5 cm,
- -10 cm $<$ radius of conversion < 50 cm,

- $\Delta\phi < 0.05$,
- Pointing residual to origin < 1.0 cm.

Figure 4-6 shows the $(\frac{dE}{dX}_i - \frac{dE}{dX}_e)/\sigma_i$ distribution for the conversion candidates. We can see that the distribution is dominated by non-electron tracks. After requiring that

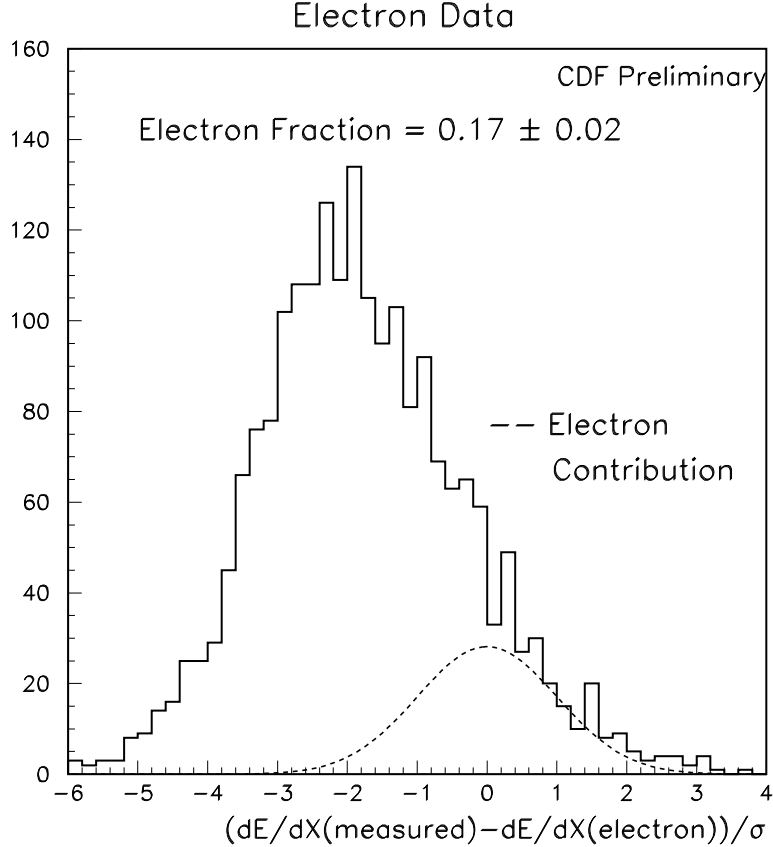


Figure 4-6: The histogram is the $(\frac{dE}{dX}_i - \frac{dE}{dX}_e)/\sigma_i$ distribution for the conversion partner candidates. The super-imposed function shows the electron contribution.

there be at least twenty-four CTC hits, we used the likelihood function of Equation 4.8 to determine that the electron fraction of the conversion candidates is 0.17 ± 0.02 . Figure 4-7 shows the p_t distribution for the conversion candidates. The ratio of areas of the histogram and the exponential fit gives an efficiency of $\epsilon = 0.77 \pm 0.02$. The conversion fraction is given by $f_{conv} = \frac{f_e N_{loose}}{\epsilon N_{tot}}$ where f_e is the electron fraction of the conversion candidates, N_{loose} is the number of events with a conversion candidate

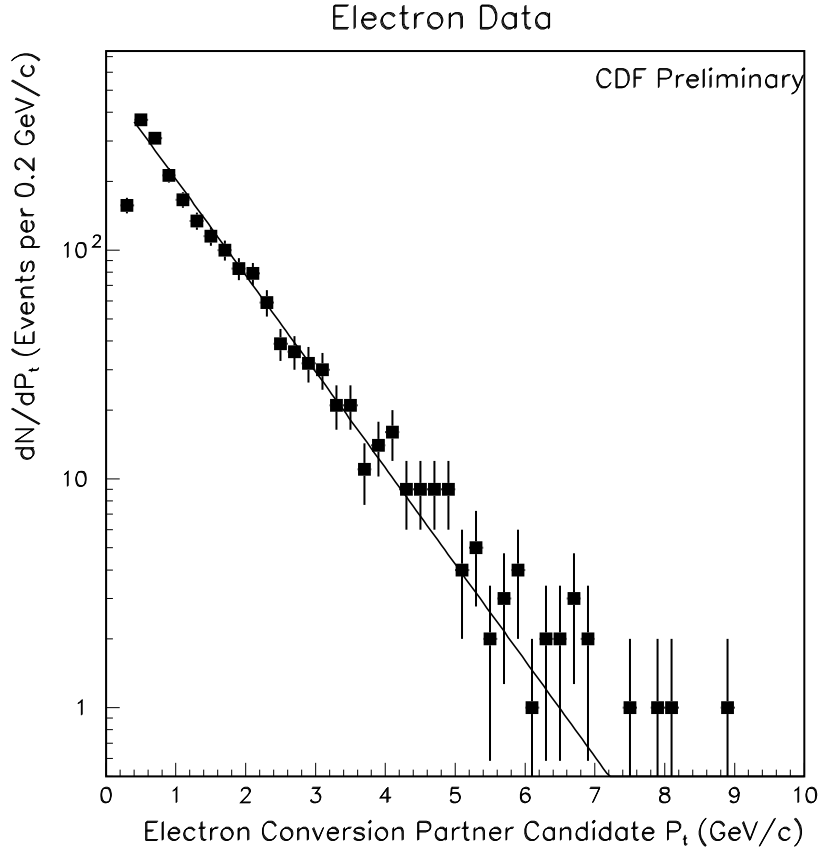


Figure 4-7: p_t spectrum for the conversion candidates with an exponential fit used to determine the p_t efficiency.

using the loose criteria, and N_{tot} is the total number of events. We measure:

$$f_{conv} = 0.008 \pm 0.001. \quad (4.10)$$

4.6 Electron Prompt Charm Fraction

We use the mass of the secondary vertex, as defined in Equation 4.1, in order to discriminate between vertices due to prompt charm decays and vertices due to b hadron decays. The mass of the b quark is sufficiently heavier than the c quark to allow for a separation of the two samples. The events for which the trigger lepton is really a hadron or conversion candidate still have secondary vertices due to heavy flavor decays, and thus have secondary vertices with masses which discriminates between prompt charm and prompt bottom decays. Since the fake and conversion fractions are so small, we are justified in fitting the secondary vertex mass distribution with bottom and charm templates only anyway. We therefore use templates from the Monte Carlo for the secondary vertex mass distribution for charm and bottom events. We perform a binned histogram fit in which the normalization of $b\bar{b}$ template was allowed to float and the bottom and charm contributions were constrained to be 100%. Figure 4-8 shows these distributions. The $b\bar{b}$ fraction was determined to be

$$f_{bb}^e = 0.96 \pm 0.01. \tag{4.11}$$

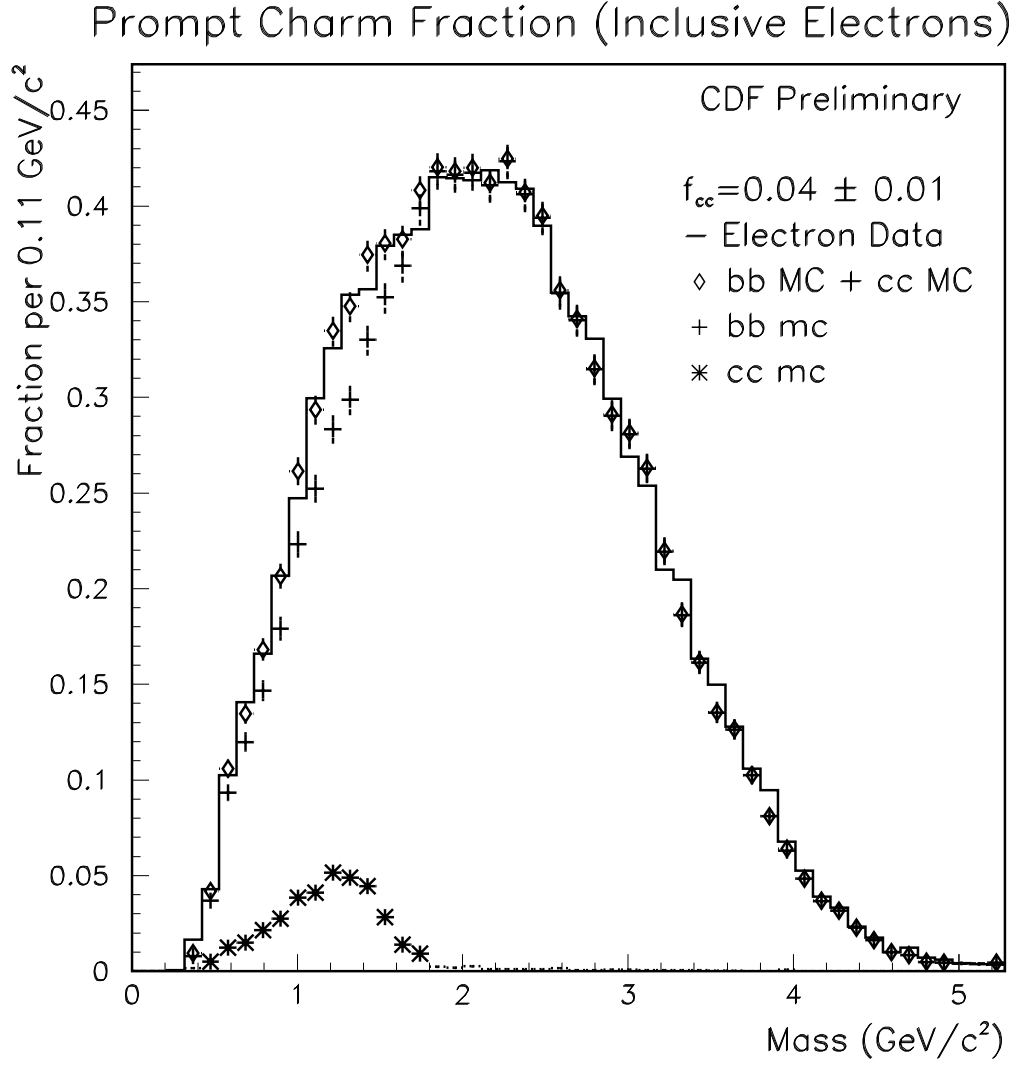


Figure 4-8: The secondary vertex mass distribution for the electron data with Monte Carlo templates used to fit the $b\bar{b}$ fraction.

4.7 Muon Fake Fraction

Some fraction of the trigger muon candidates are hadrons masquerading as trigger muons. Because we can not separate muons from pions using $\frac{dE}{dX}$ (see Figure 4-4) we must employ another method to determine this fraction. Furthermore when a pion or kaon decays to a muon in flight, we would still consider this muon to be a fake since it is not the B decay product with the proper charge correlation to the B flavor.

We are only concerned when the trigger muon candidate is a “fake” and has a charge which is not properly correlated to the decaying B flavor. When the charge of the fake muon properly identifies the decay flavor of the B meson, we may treat the fake muon as if it were a real muon. We must determine, therefore, the fraction of trigger muon candidates which have the wrong charge-flavor correlation. We call this fraction the wrong-sign muon fake fraction, $f_{ws-fake}^\mu$.

Since the production flavor tagging (SST) is completely uncorrelated to the decay of the B meson, the SST dilutions in the electron and muon samples are the same. The decay flavor tagging dilution depends on the sample composition, which is different between the electron and muon samples. We determine all of the sample composition fractions in both samples except the wrong sign fake fraction, which we can therefore determine from a comparison of the production and decay flavor tagging dilutions. This will be discussed in greater detail in Chapter 7, when the construction of the fitter is presented. The wrong-sign fake fraction is determined to be

$$f_{ws-fake}^{\mu} = 0.02_{-.02}^{+.03}. \quad (4.12)$$

The total muon fake fraction is twice this value, or $0.04_{-.04}^{+.06}$.

4.8 Muon Prompt Charm Fraction

We determine the muon charm fraction using the same method as was used to determine the electron charm fraction. Monte Carlo templates of the secondary vertex mass distributions for $b\bar{b}$ and $c\bar{c}$ are used to fit the secondary vertex mass distribution in the data. Figure 4-9 shows the result of this fit.

We determined the $b\bar{b}$ fraction to be

$$f_{bb}^{\mu} = 0.92 \pm 0.01. \quad (4.13)$$

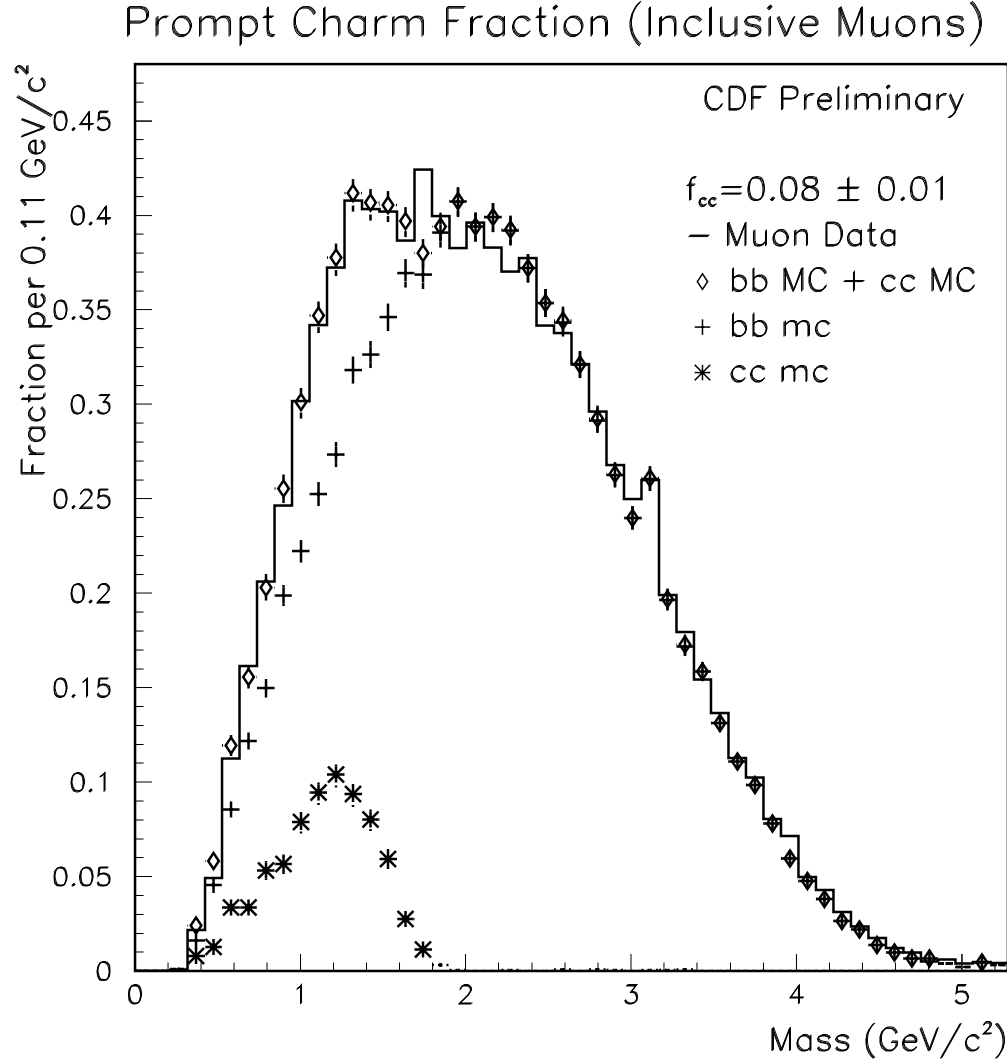


Figure 4-9: The secondary vertex mass for the muon data with Monte Carlo templates used to fit the $b\bar{b}$ fraction. One can see a peak in the Monte Carlo and data due to $\psi \rightarrow \mu\mu$ where there are two tracks in the secondary vertex.

4.9 $b\bar{b}$ and $c\bar{c}$ Particle Species

Bottom and charm quarks can fragment into a variety of long-lived hadrons whose decays provide secondary vertices in our electron and muon samples. From bottom quarks, we find B^0 , B^\pm and B_s mesons as well as Λ_b baryons. From charm quarks, we find D^0 , D^\pm , and D_s mesons. Λ_c is not included because we find in the Monte Carlo that we rarely reconstruct a secondary Λ_c vertex. This is unsurprising given the short lifetime of the Λ_c ($\tau_{\Lambda_c} = 0.206\text{ps}$ [4]). We expect all of these hadrons to contribute to the measured asymmetry and we therefore account for them in the determination of Δm_d .

Chapter 5

The Proper Time of Decay

In this chapter we present the reconstruction of the proper time of decay for B mesons. Because of imperfect reconstruction of the distance traveled before decay and imperfect determination of the B momentum, we are not able to reconstruct the proper time perfectly. The method for handling these resolutions is presented.

5.1 Proper Time Reconstruction

For a B meson which travels during its lifetime a distance L_{xyz} in the lab frame at a velocity v (with a momentum of $p = M_B v \gamma$), the proper time, t , is given by

$$t = \frac{L_{xyz}}{\gamma v} = \frac{L_{xyz} \sin(\theta)}{\gamma v \sin(\theta)} = \frac{L_{xy} M_B}{p_t(B)}, \quad (5.1)$$

where θ is the angle between the momentum of the particle and the z axis in the lab frame, L_{xy} is the distance in the lab frame traveled by the particle transverse to the z axis, and $p_t(B)$ is the momentum of the B meson transverse to the z axis. We are not able to reconstruct the proper decay time perfectly, and thus measure distributions as a function of the reconstructed pseudo-proper time, t' :

$$t' = \frac{L_{xy}^{meas} M_B}{p_t(Jet)}, \quad (5.2)$$

where L_{xy}^{meas} is the measured distance between the primary and secondary vertices and $p_t(Jet)$ is the transverse momentum of the secondary vertex tagged B jet. We

compute $p_t(Jet)$ as the total transverse component of the vector sum of the momenta of the tracks that make up the jet ¹:

$$p_t(Jet) = |(\sum_i \vec{p}_i) \times \hat{z}|. \quad (5.3)$$

The mixing probability density functions are computed from basic physical principles as functions of proper time (see Equation 1.20). In order to extract the value of Δm_d from the data we need to determine the functions in terms of the pseudo-proper time. The transformation from a function of the proper-time to a function of the pseudo-proper time is called the “smearing” of the function. We consider two independent sources for smearing a function of proper time, the B momentum resolution and the L_{xy} resolution.

Suppose we know the conditional probability function, $\bar{\rho}(t'; \Delta m_d)$, of the pseudo-proper time t' . In order to incorporate the effect of an imperfect determination of the B momentum, we define a scale factor for the reconstructed momentum:

$$k = \frac{p_t(Jet)}{p_t(B)}. \quad (5.4)$$

We define the k -factor distribution, $D(k)$, to be the probability density that $\frac{p_t(Jet)}{p_t(B)}$ takes on the value k . We can write $\bar{\rho}(t'; \Delta m_d)$ as an expansion integral over the different k possibilities:

$$\bar{\rho}(t'; \Delta m_d) = \int dk D(k) \bar{\rho}(t'; k, \Delta m_d), \quad (5.5)$$

where $\bar{\rho}(t'; k, \Delta m_d)$ is the conditional probability distribution given k and Δm_d as a function of t' . We have used the fact that the k -factor distribution does not depend on Δm_d . Next we expand, in a similar fashion, over the true proper time. The probability density for finding an event with a true proper time, t , conditioned upon Δm_d , is $\rho(t; \Delta m_d)$. It is the function $\rho(t; \Delta m_d)$ that we can compute from physical principles. We have

$$\bar{\rho}(t'; \Delta m_d) = \int dk D(k) \int dt \bar{\rho}(t'; \Delta m_d, k, t) \rho(t; \Delta m_d). \quad (5.6)$$

¹Recall that the tracks that comprise a jet are those that fall inside a cone of radius 1.0 about the jet axis.

We can rewrite this as a convolution over a resolution function by applying a variable transformation $\bar{\rho}(t'; \Delta m_d, k, t) \rightarrow R(t' - t/k)$. The resolution function, R , does not depend conditionally on k since it has been normalized out in t/k . We therefore have

$$\bar{\rho}(t'; \Delta m_d) = \int dk D(k) \int dt R(t' - t/k) \rho(t; \Delta m_d). \quad (5.7)$$

Equation 5.7 shows the smearing transformation from $\rho(t; \Delta m_d)$ to $\bar{\rho}(t'; \Delta m_d)$ in terms of the probability distribution over $t' - t/k$, and the probability distribution over k . Both the resolution function, R , and the k -factor distributions, D , are determined from Monte Carlo.

5.2 k -Factor Distributions

The transverse momentum of the secondary vertex tagged jet is not equal to the transverse B momentum because the jet momentum determination is susceptible to errors in the measurement of tracks in the jet, the lack of inclusion of neutral B daughters, and the inclusions of non- B daughter tracks associated with the fragmentation leading to the B and the underlying event.

The $p_t(Jet)$ distributions for electron data and Monte Carlo are shown in Figure 5-1. The distributions for the muon data and Monte Carlo is shown in Figure 5-2. We can see that the Monte Carlo does very well at simulating the observed jet p_t spectrum.

Every particle species has a different decay multiplicity and different kinematics. We therefore used different Monte Carlo derived k -factor distributions for each particle species. Figure 5-3 shows the k -factor distributions for electron and muon $b\bar{b}$ Monte Carlo and Figure 5-4 shows the k -factor distributions for electron and muon $c\bar{c}$ Monte Carlo.

b-Tagged Jet P_t (Electron Data and Monte Carlo)

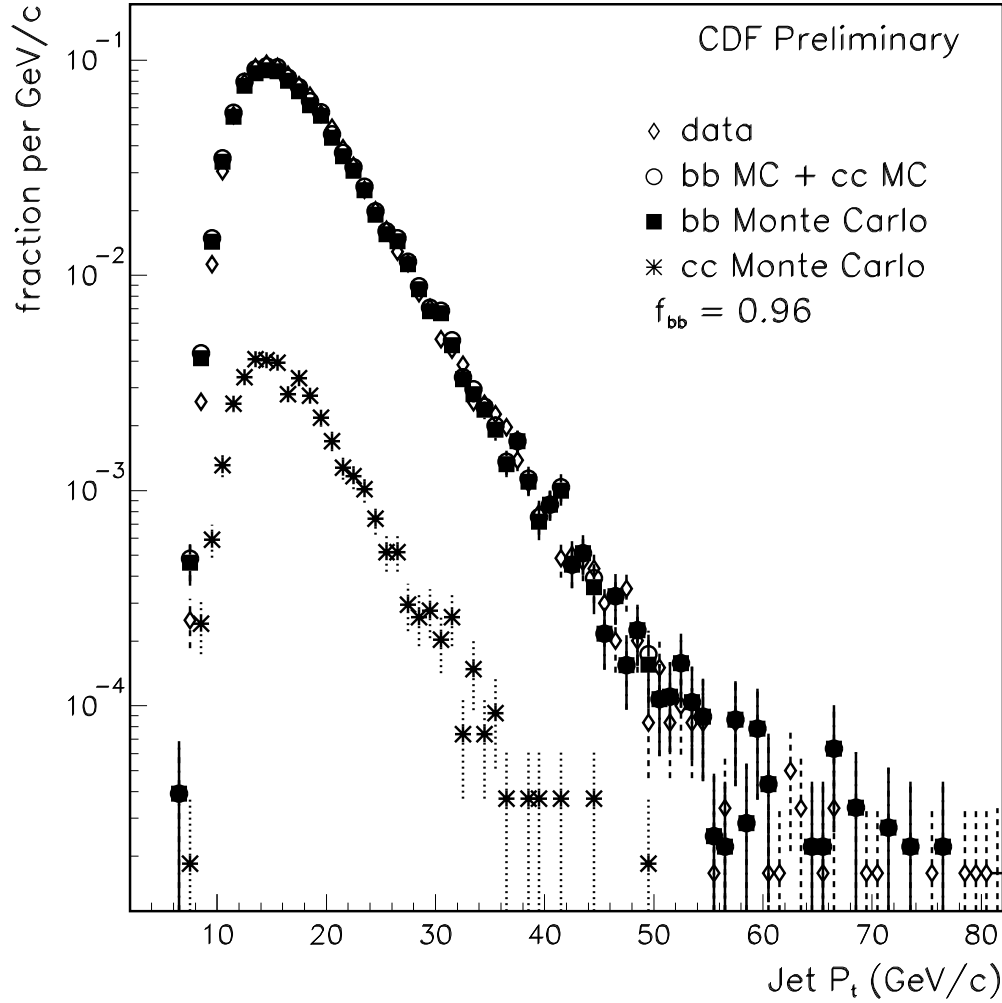


Figure 5-1: The transverse momentum for secondary vertex tagged jets from electron data and Monte Carlo samples.

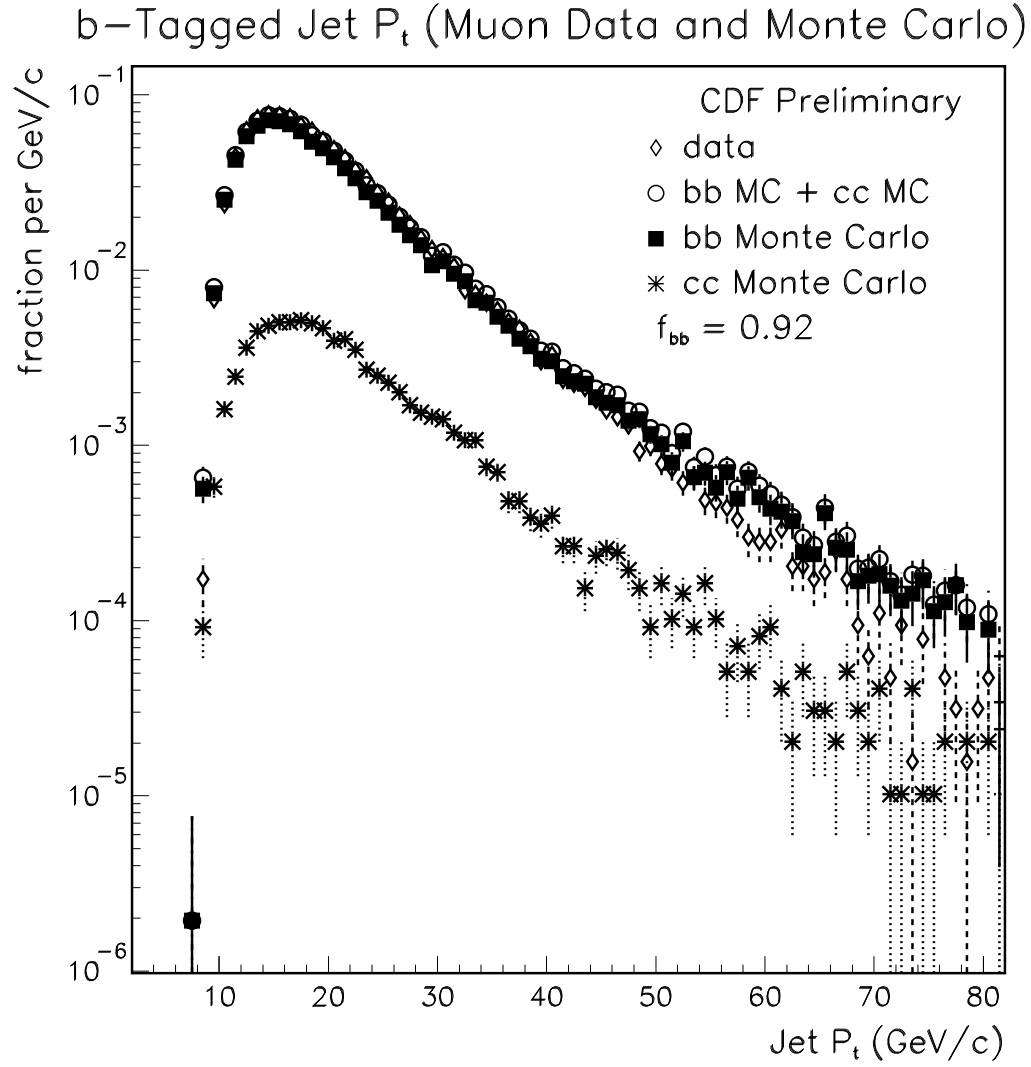


Figure 5-2: The transverse momentum for secondary vertex tagged jets from muon data and Monte Carlo samples.

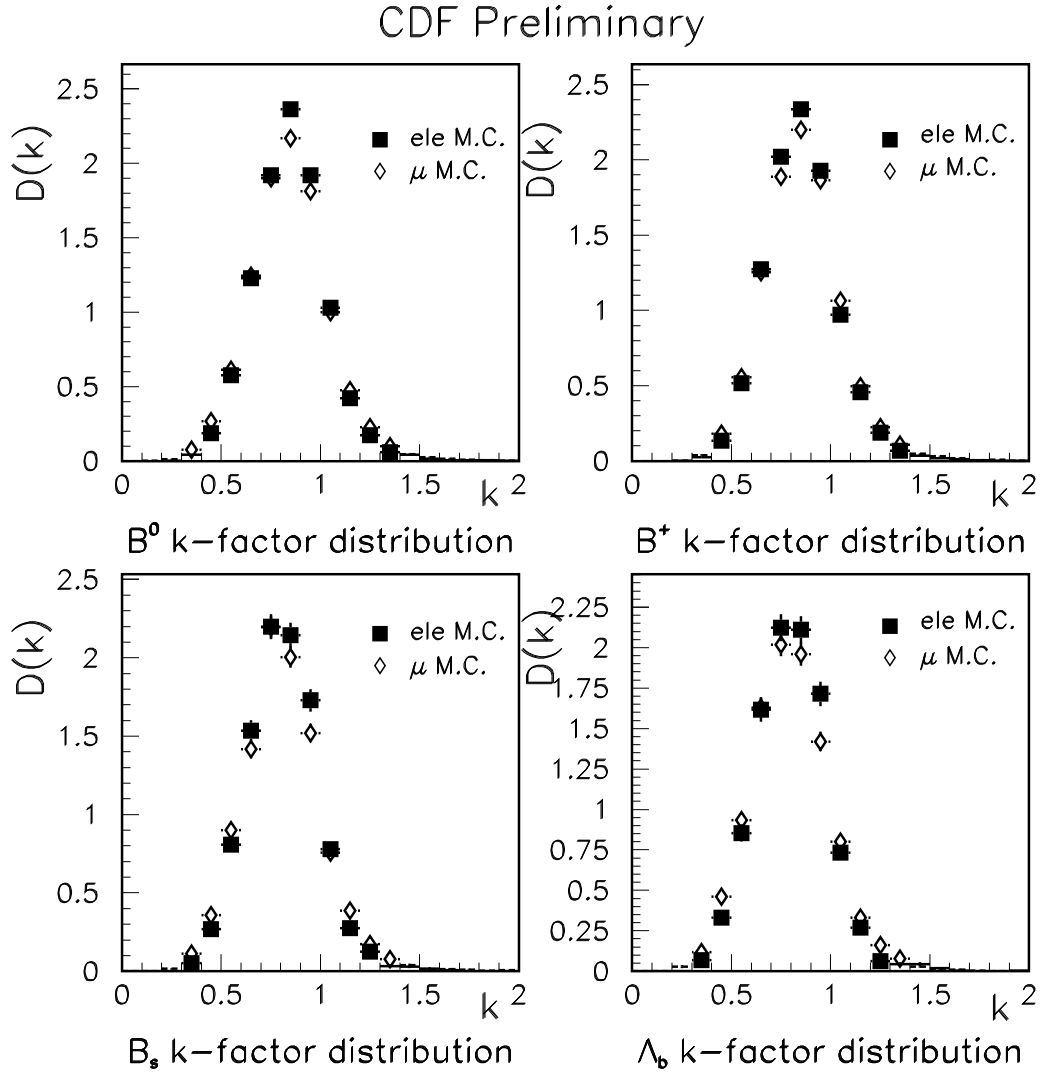


Figure 5-3: Binned k -factor distribution from the electron and Muon Monte Carlo samples for the $b\bar{b}$ particle species.

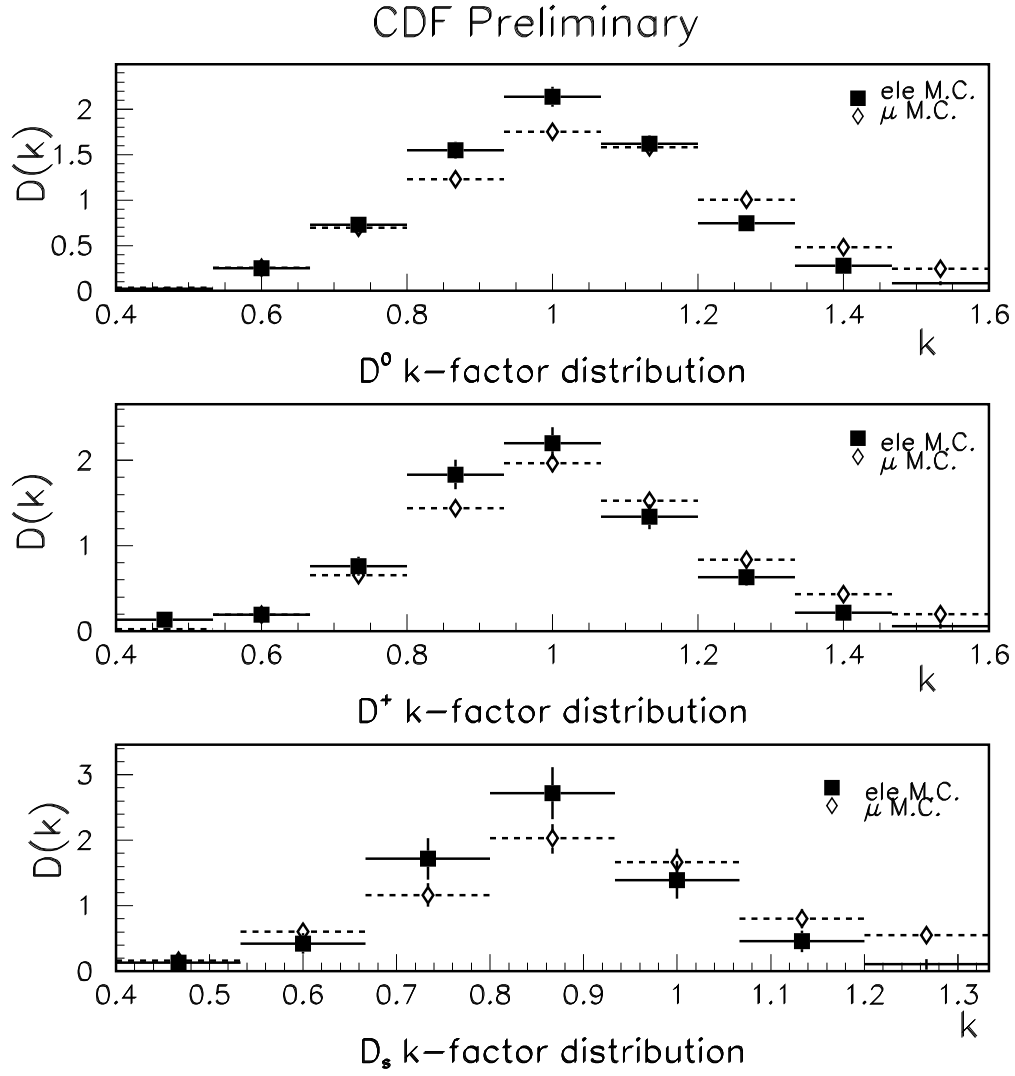


Figure 5-4: Binned k -factor distribution from the electron and muon Monte Carlo samples for the $c\bar{c}$ particle species.

5.3 The Proper Time Resolution

We determined the resolution function $R(t' - t/k)$ from the Monte Carlo. The proper time resolution is determined by the L_{xy} resolution and the observed jet p_t spectrum:

$$R(t' - t/k) = R\left(\frac{M_B}{p_t(jet)} \Delta L_{xy}\right). \quad (5.8)$$

We saw in Figures 5-1 and 5-2 that the Monte Carlo reproduces the jet p_t spectrum well. Figures 5-5 and 5-6 show that the Monte Carlo also reproduces the observed L_{xy} spectrum accurately. Finally, the Monte Carlo pseudo-proper time distribution also matches well with the data for electrons and muons, as can be seen in Figure 5-7 and 5-8. We therefore have confidence in using the Monte Carlo in determining the proper time resolution function.

We parameterized the resolution function with a central Gaussian, two negative exponential tails, and three positive exponential tails. This arbitrary parameterization is the same for the muon sample and the electron sample. Figure 5-9 shows the resolution function parameterization super-imposed over the proper time resolution determined from the electron Monte Carlo. Figure 5-10 shows the same resolution function parameterization super-imposed over the proper time resolution determined from the muon Monte Carlo.

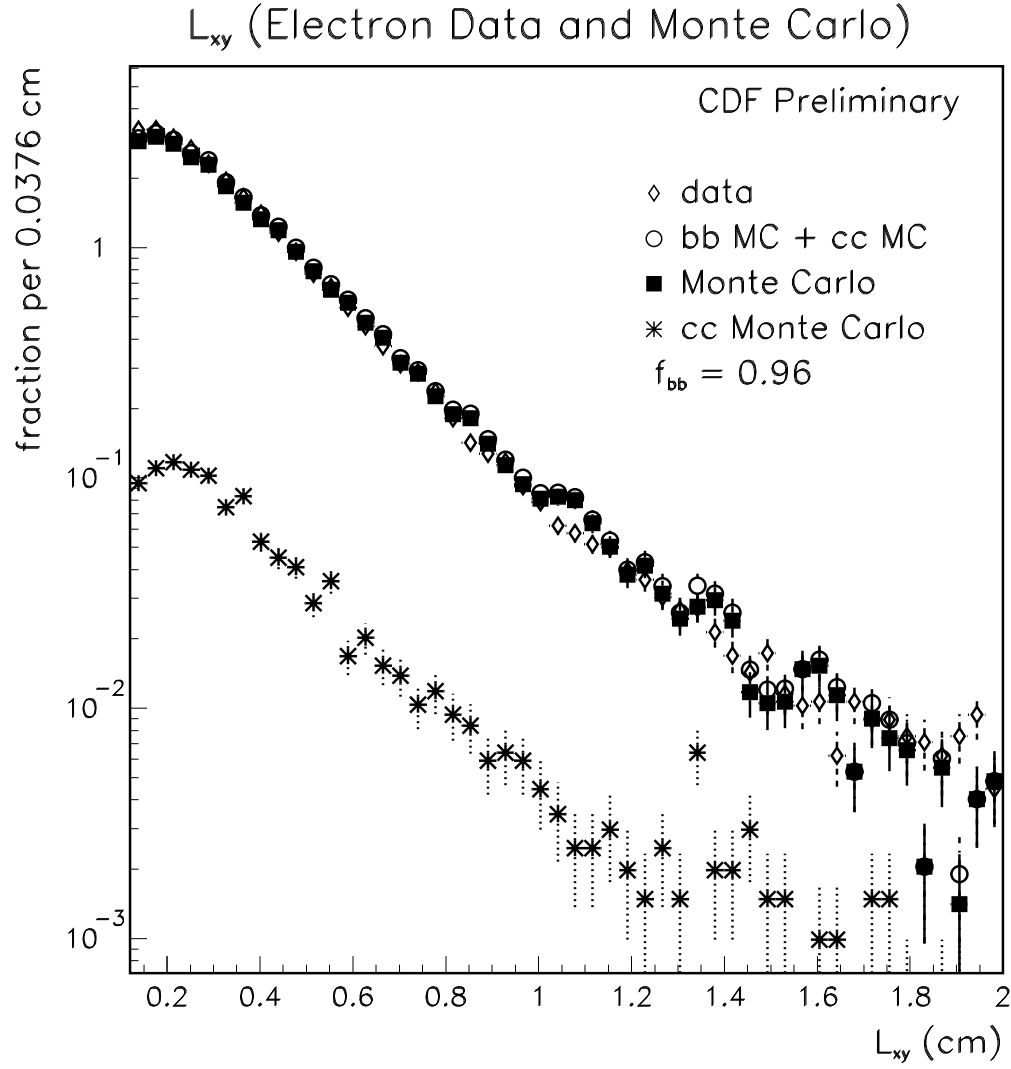


Figure 5-5: A comparison of the L_{xy} distributions from the electron data and the electron Monte Carlo samples.

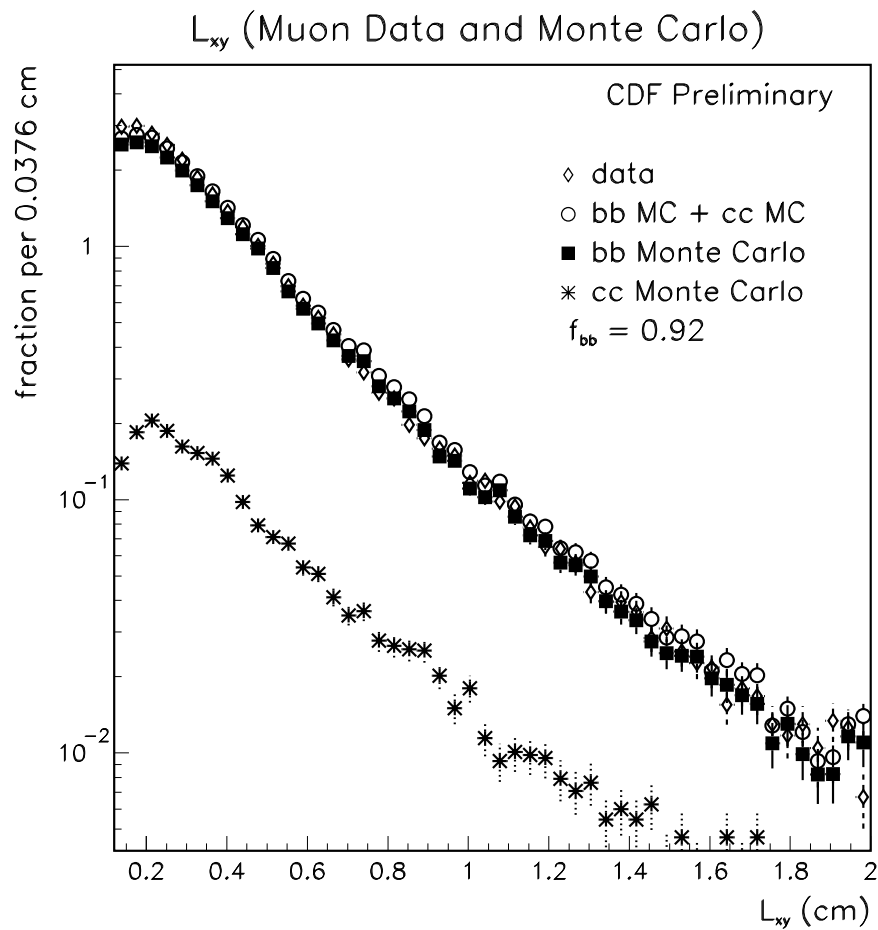


Figure 5-6: A comparison of the L_{xy} distributions from the muon data and the muon Monte Carlo samples.

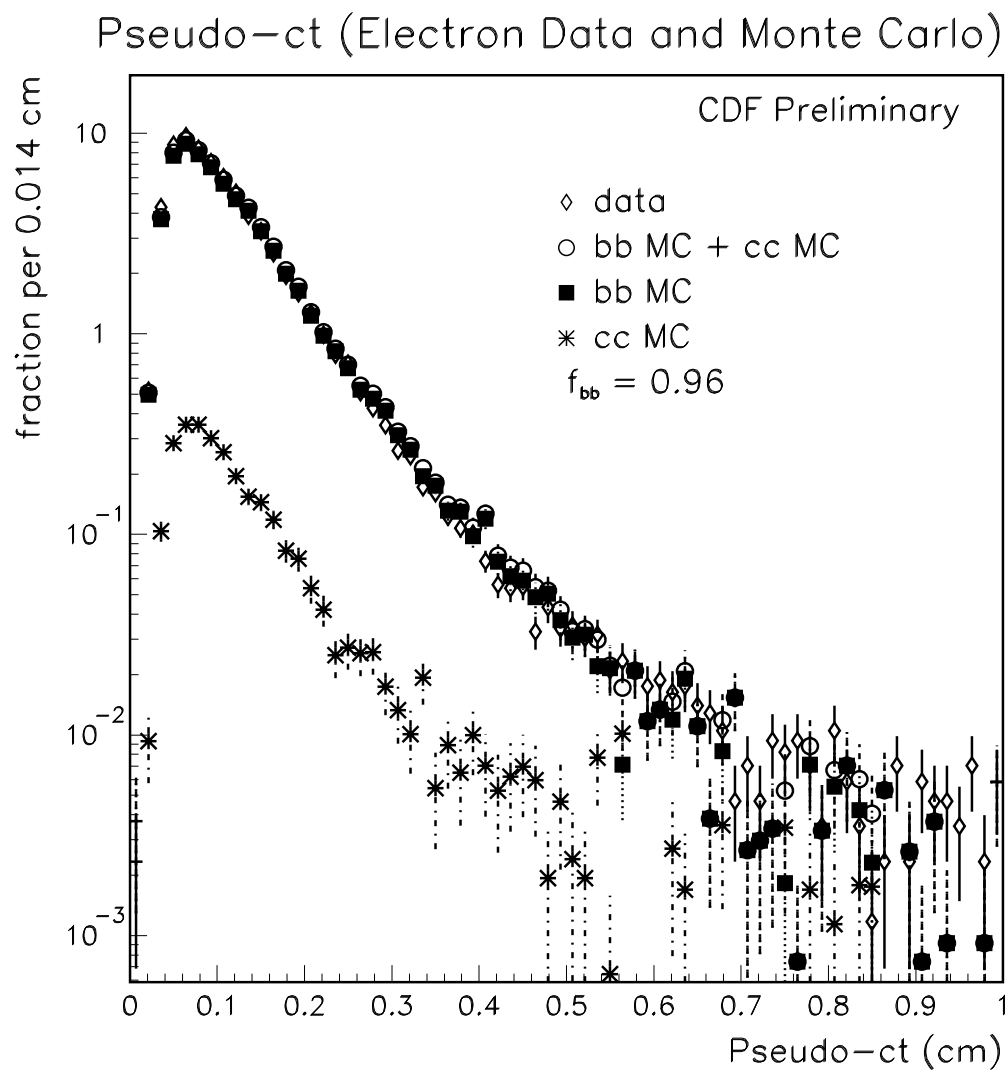


Figure 5-7: A comparison of the pseudo-proper time distributions from the electron data and electron Monte Carlo samples.

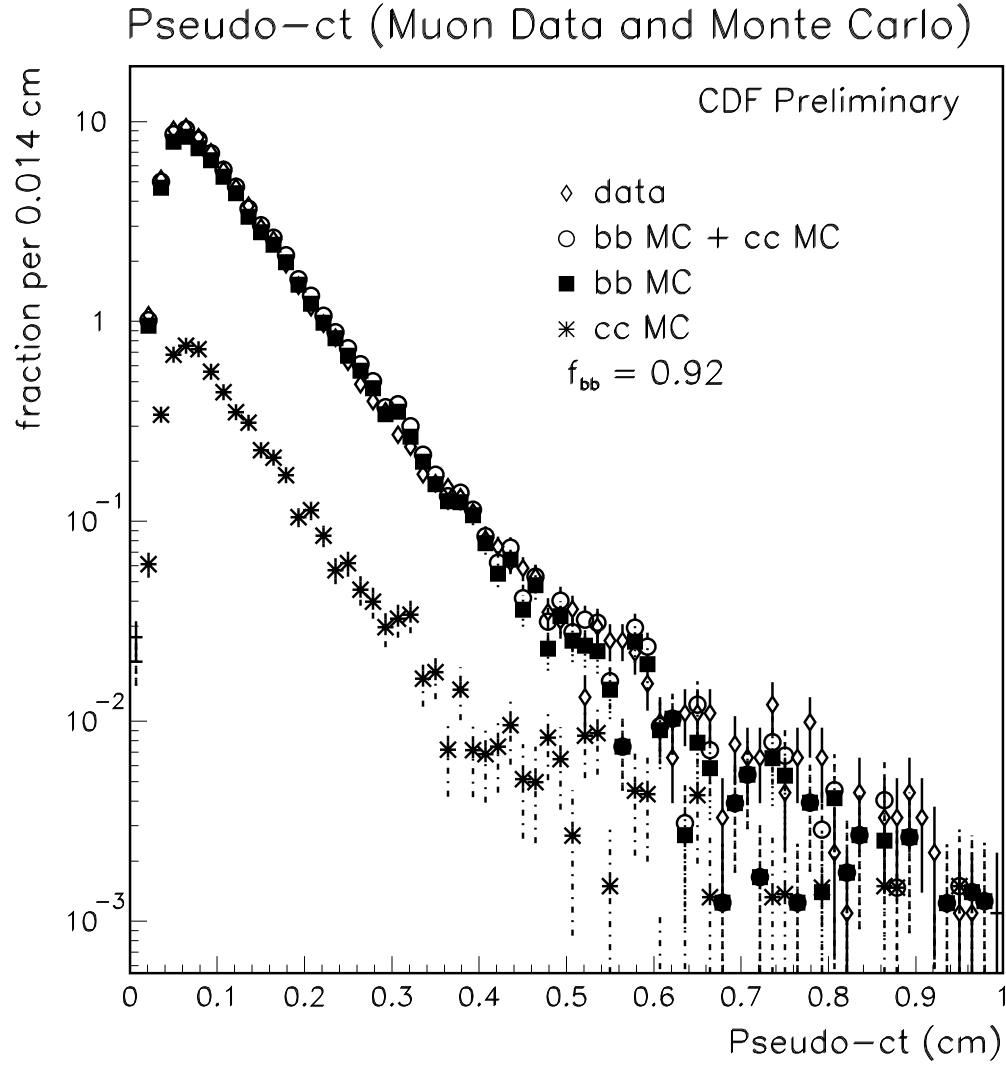


Figure 5-8: A comparison of the pseudo-proper time distributions from the muon data and muon Monte Carlo samples.

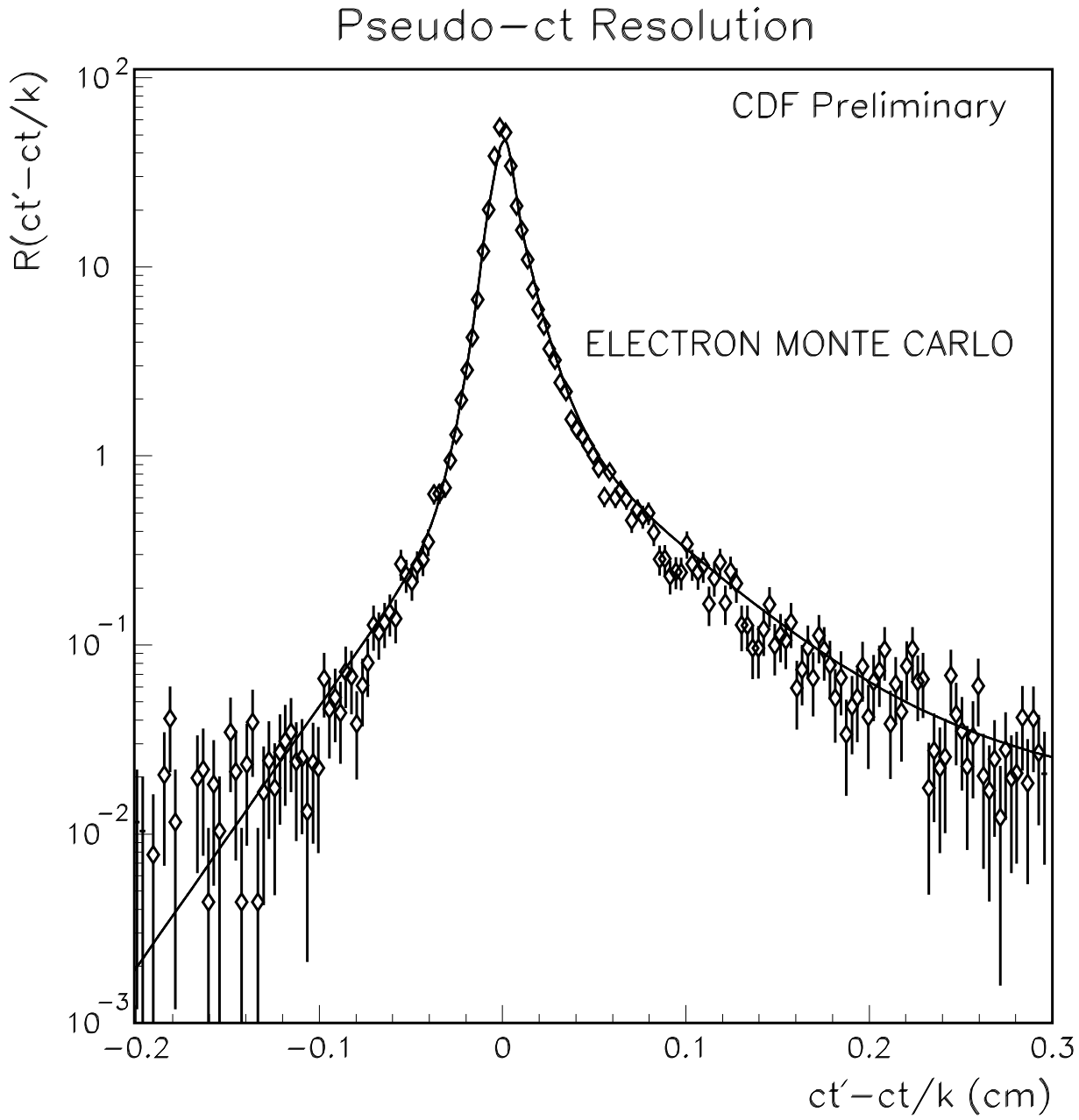


Figure 5-9: The resolution in proper time determined from the electron Monte Carlo with the parameterization, $R(t' - t/k)$, super-imposed. The distribution is asymmetric since the D vertex pulls the L_{xy} to larger values.

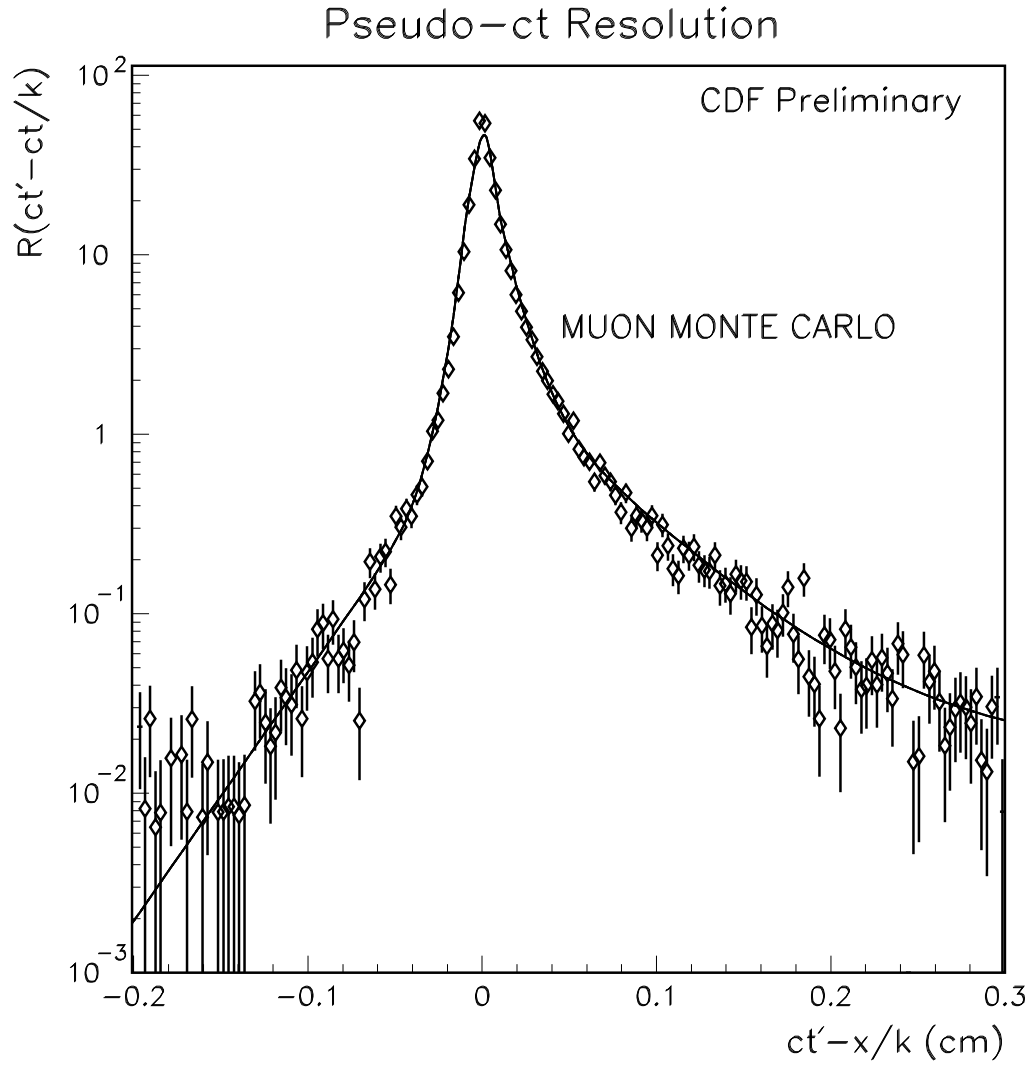


Figure 5-10: The resolution in proper time determined from the muon Monte Carlo with the parameterization, $R(t' - t/k)$, super-imposed. The distribution is asymmetric since the D vertex pulls the L_{xy} to larger values.

Chapter 6

Flavor Tagging

In this chapter we present the decay and production flavor tagging algorithms. In section 6.1 we discuss the performance of decay flavor tagging when using the charge of the trigger lepton as the tagger. In section 6.2 we introduce the Same Side Tagging algorithm used in this analysis for the determination of the production flavor of B mesons. The use of SST in an inclusive lepton environment is complicated by the potential of confusing B daughters with charge-flavor correlated tracks. The SST algorithm used in this analysis is constructed so that the effect of this confusion is small. In section 6.2.6 we describe the residual effects of tagging on B daughters on the determination of Δm_d . In section 6.3 we present the pseudo-proper time dependent asymmetries measured in the electron and muon samples.

6.1 Decay Flavor Tagging

When the trigger lepton is a decay product of the bottom quark of a B meson, the charge of the trigger lepton is perfectly correlated to the flavor of the decaying B meson, as explained in section 3.3.1. Because the trigger lepton can also come from other sources, the decay flavor tagging dilution is less than 1.0. We determine the decay flavor mistag rate from the sample composition.

There are four sources for trigger electrons:

- The trigger electron is the lepton from a $b \rightarrow cl\nu$ decay.

- The trigger electron is really a hadron (a fake).
- The trigger electron comes from a photon conversion.
- The trigger electron is from a c quark which is itself a decay product of the b quark (a sequential decay product).

The fake and conversion fractions are measured from the data and the sequential fraction is determined from the Monte Carlo. The probability that an electron candidate has the wrong charge is given by $p_{w-e}^{fake} = f_{fake}^e/2$ when the trigger electron is a fake and by $p_{w-e}^{conv} = f_{conv}/2$ when the trigger electron is from a photon conversion. Recall that the descriptions of the determination of the fake fraction in the electron sample, f_{fake}^e , is shown in section 4.4 and the determination of the conversion fraction in this sample, f_{conv}^e , is in section 4.5. We determined the wrong-sign sequential fraction, the fraction of trigger electrons that are due to sequential c decays with a charge different from the lepton expected from the decay of the b quark that produced the c quark, from the Monte Carlo to be $p_{w-e}^{seq} = 0.06 \pm 0.01$. The total probability that the trigger electron is the wrong charge is given by

$$p_{w-e} = p_{w-e}^{seq}(1 - p_{w-e}^{conv})(1 - p_{w-e}^{fake}) + p_{w-e}^{conv}(1 - p_{w-e}^{fake})(1 - p_{w-e}^{seq}) + p_{w-e}^{fake}(1 - p_{w-e}^{conv})(1 - p_{w-e}^{seq}), \quad (6.1)$$

where we have used the fact that the different categories of wrong-sign leptons are mutually exclusive.

Trigger muon candidates can come from all of the same sources as the electron candidates except photon conversions. For muons we have the analogous case for fakes, $p_{w-\mu} = f_{ws-fake}^{muon}$. The wrong sign sequential fraction is determined from Monte Carlo to be $p_{w-\mu}^{seq} = 0.085 \pm 0.01$. The total wrong sign probability for muon candidates is given by:

$$p_{w-\mu} = p_{w-\mu}^{seq}(1 - p_{w-\mu}^{fake}) + p_{w-\mu}^{fake}(1 - p_{w-\mu}^{seq}). \quad (6.2)$$

The probability of getting a trigger muon candidate that is a wrong sign fake muon is a free parameter which was determined from the data simultaneously with the charged and neutral B meson flavor tagging dilutions and Δm_d .

6.2 Production Flavor Tagging

In section 3.3.2 we showed that, as was first observed by Gronau, Nippe, and Rosner [19], the flavor of a B meson at the time of production can be inferred from the charges of some of the particles that are produced along with the B meson. This inference is central to the construction of Same Side Tagging algorithms.

The SST method has been shown to work effectively at production flavor tagging of exclusive and partially reconstructed B decays in analyses at CDF (see references [32] and [33]). In those analyses, the charge of a single track was used to infer the production flavor of B mesons. Many different track selection criteria were considered to find a strongly charge-flavor correlated track. The algorithm settled upon in these analyses selects the charge of the track with the smallest momentum transverse to the B momentum vector, p_t^{rel} , from the potential candidate tracks as the production flavor tagger. We refer to this SST algorithm as the “minimum p_t^{rel} SST algorithm.” Figure 6-1 shows the definition of p_t^{rel} . For determining p_t^{rel} in the inclusive lepton environment it is better to use the vector pointing from the primary vertex to the secondary vertex rather than the B momentum vector as the direction of B flight, since the B momentum is not measured accurately without an explicit reconstruction of the B meson. However, the minimum p_t^{rel} algorithm does not work well with an inclusive lepton sample because it tends to select, as the production flavor tag, the charge of B meson daughters when they have not been included in the secondary vertex.

When a charged B meson daughter is not included as part of the secondary vertex, this track has an impact parameter with respect to the primary vertex that is small enough to be considered consistent with coming from the primary vertex. Because the track is a B meson daughter and because of resolution effects, it will also have a small nonzero impact parameter with respect to the secondary vertex, from which the track originates. Such a track, close to both the primary and secondary vertices, will have a small opening angle with respect to the B direction and is therefore likely to have a small p_t^{rel} . The shorter the distance that a B meson travels before decaying, the more

likely a B daughter will have a small impact parameter with respect to the primary vertex and thus the more likely the minimum p_t^{rel} algorithm will select a B daughter as the production flavor tag. When the transverse decay distance is small, more than a third of the minimum p_t^{rel} SST candidates are actually B daughters. Since the decay products of a B meson contain no information about the its production flavor, the rate of such tags should be accounted for and minimized. We therefore abandoned the minimum p_t^{rel} algorithm and constructed a new algorithm which is less sensitive to B daughter tracks.

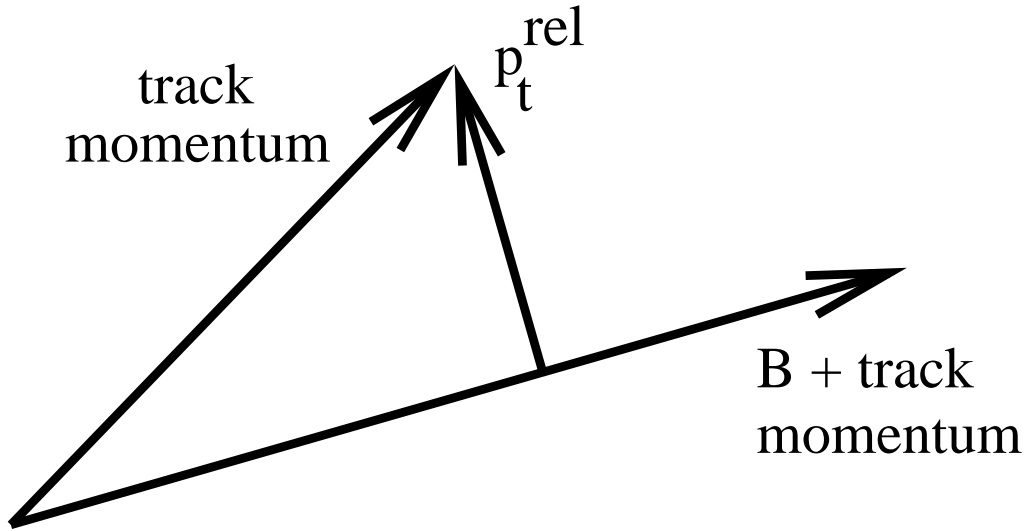


Figure 6-1: p_t^{rel} is the momentum of a track transverse to the vector sum of the B and track momenta.

We made two major modifications in replacing the minimum p_t^{rel} algorithm. Rather than using the charge of a single track as the production flavor tagger, we take the sum of the charge of all of the tracks that satisfy the SST candidate selection criteria. The production flavor determination is more robust with respect to inclusion of B daughters when determined in this way. We call such an algorithm a “Voting SST” algorithm, since each candidate track “votes” its charge, and the majority charge wins. It should be noted that the minimum p_t^{rel} algorithm has a much better performance in the exclusively reconstructed environment as compared to the inclusive environment, but even in reconstructed and partially reconstructed B samples, a Voting SST

algorithm was found to be an improvement over the minimum p_t^{rel} algorithm [34].

We also added a track requirement intended to exclude B daughter tracks from voting. We associated with each track which satisfied the same quality criteria that are used in the minimum p_t^{rel} algorithm, a probability that the track is a B daughter. This probability was computed from the Monte Carlo samples as a function of track parameters which allowed us to distinguish primary tracks from secondary tracks. The flavor tag was determined by the sum of the charges of the tracks with a probability of being a B daughter of at most 0.3:

$$Q_{sst} = \sum_{p_B < 0.3} Q_i. \quad (6.3)$$

The value of the probability cut, 0.3, was determined from optimization in the Monte Carlo. For a meson which is a B^0 at the times of production and decay, $Q_{sst}q_{lep} > 0$, where q_{lep} is the charge of the trigger lepton.

6.2.1 Avoiding Tagging on B Daughters

Primary tracks are tracks that originate from the primary vertex. Tracks of pions from B^{**} decays and tracks of particles that are part of the fragmentation chain of a B meson are primary tracks. In order to distinguish tracks of B daughters from primary tracks we identified physical distributions that separate the two sources of tracks. We considered a large number of distributions and settled on two for this analysis. It is optimal to use all of the variables at once, but accounting for the correlations between the different variables used for the separation of B daughters and primary tracks requires a Monte Carlo sample that grows exponentially with the number of variables used. We used the most effective two variables, r and ΔR .

The probability distributions over these two variables were used to distinguish B daughters from primary tracks in the SST algorithm. We therefore applied the SST track candidate selection criteria, listed in section 6.2.4, to the tracks used in the computation of the probability of finding B daughters as a function of r and ΔR .

The r distribution

Primary tracks should have small impact parameters with respect to the primary vertex and large impact parameters with respect to the secondary vertex, while B daughters should have large impact parameters with respect to the primary vertex and small impact parameters with respect to the secondary vertex. We would therefore expect that the ratio of impact parameters with respect to the primary and secondary vertices should separate B daughter and primary tracks. Even for B daughters that are not included in the secondary vertex because they have relatively small impact parameters with respect to the primary vertex, the particle track should be closer to the secondary vertex than the primary vertex. We weight the impact parameter, d , by the error on the impact parameter, σ , to get the impact parameter significance, d/σ . By using the impact parameter significance rather than the raw impact parameter, we can avoid over-weighting poorly tracks. Also, the primary and secondary vertices are determined to different accuracies. The distance between a track and a vertex is much more significant when the error on a vertex is small as compared to when the error is large. The σ used for the computation of the impact parameter significance combines the vertex and track errors. It is convenient to define r as

$$r \equiv \frac{d_B/\sigma_B}{d_{pv}/\sigma_{pv} + d_B/\sigma_B}, \quad (6.4)$$

where d_{pv} is the impact parameter with respect to the primary vertex, d_B is the impact parameter with respect to the secondary vertex, σ_{pv} is the error of the impact parameter with respect to the primary vertex, and σ_B is the error of the impact parameter with respect to the secondary vertex. See Figure 6-2. This variable is equivalent to the ratio of impact parameters for separating between B daughters and fragmentation tracks with the added benefit that it is bounded between 0.0 (secondary tracks) and 1.0 (primary tracks). The r distribution for B meson daughters and fragmentation tracks are shown in Figure 6-3 for electrons and muons. Tracks included in the secondary vertex do not contribute to these distributions. The probability that a track is a B decay product as a function of r can be computed from these distributions as well as the overall probability that a track is a B decay product,

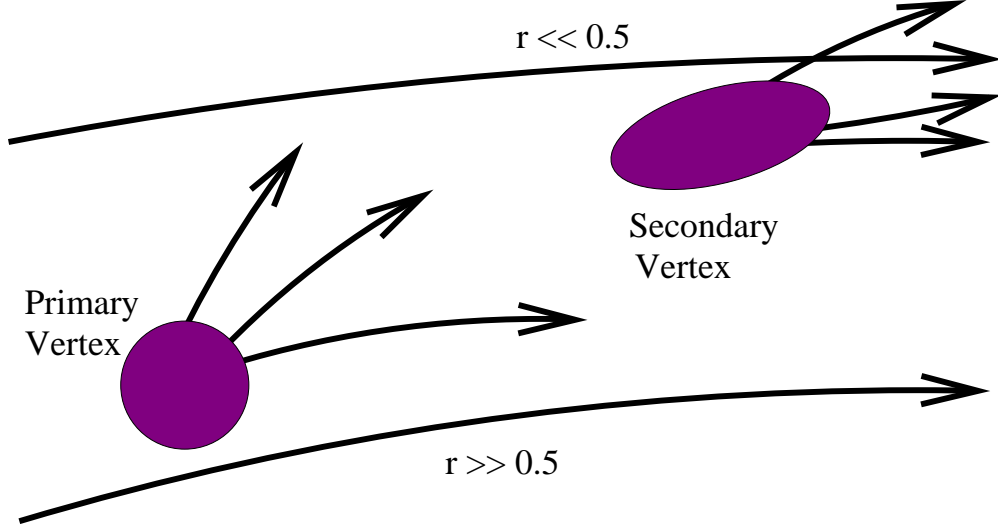


Figure 6-2: Tracks that are closer to the primary vertex have larger values of r than tracks that are closer to the secondary vertex.

$p_B^{tot} = N_B/N_{tot}$, where N_B is the total number of B decay products not included in the secondary vertex and N_{tot} is the total number of tracks:

$$p_B(r) = \frac{B(r)P_B^{tot}}{B(r)P_B^{tot} + F(r)P_F^{tot}}, \quad (6.5)$$

where $P_F^{tot} = 1 - P_B^{tot}$, $B(r)$ is the B distribution shown in Figure 6-3 and $F(r)$ is the distribution for primary tracks shown in Figure 6-3. This probability distribution is shown for electrons and muons in Figure 6-3. We can see that the r distribution will be useful for distinguishing B daughters from primary tracks since $p_B(r)$ has a clear dependence on r .

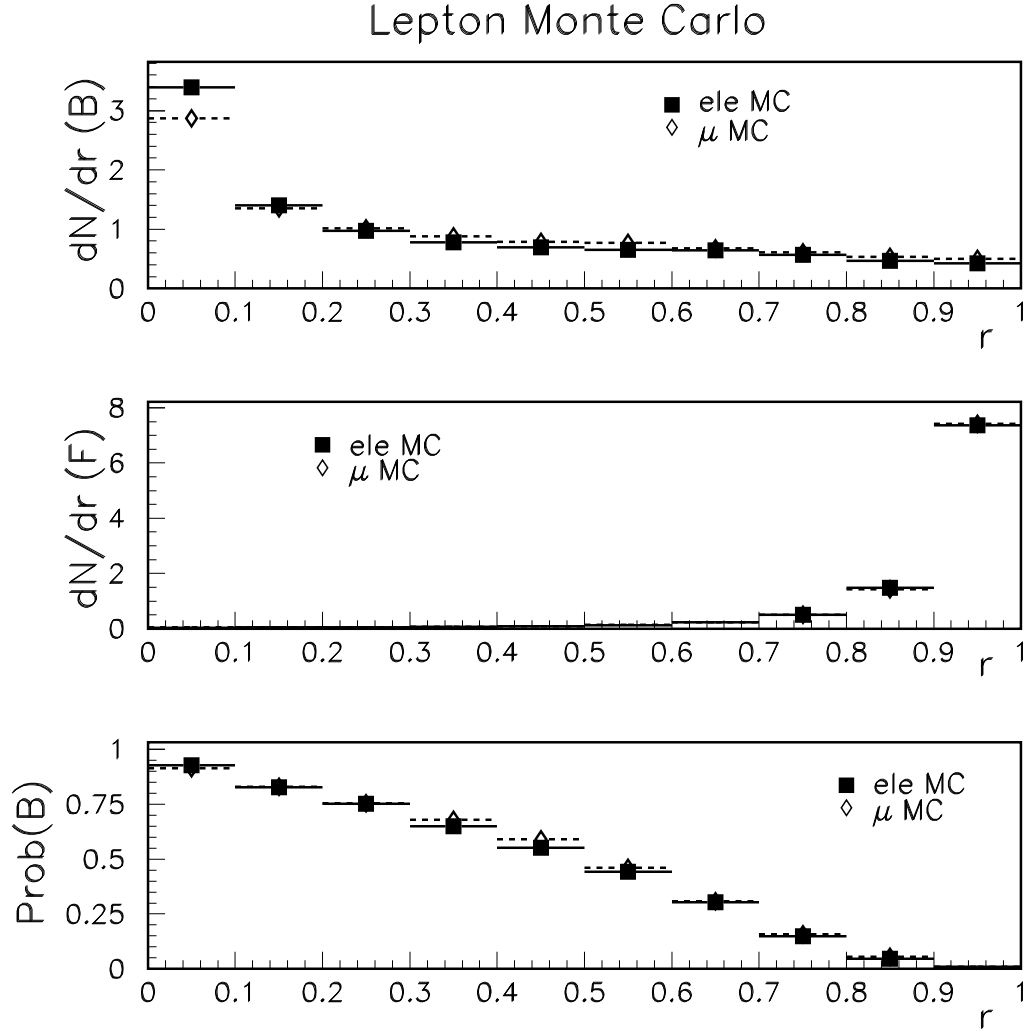


Figure 6-3: The distribution over r for B meson daughters and primary tracks for electron and muon Monte Carlo samples. Tracks in the secondary vertex are not included in the plot. The top plot is the distribution over r for B daughters, the middle plot is the distribution over r for primary tracks and the bottom plot is the probability that a track is a B daughter as a function of r .

The ΔR distribution

The ΔR of a track is the radius of the smallest cone about the vector pointing along the flight direction of a B meson that includes the track:

$$\Delta R \equiv \sqrt{\Delta\eta^2 + \Delta\phi^2}, \quad (6.6)$$

where $\Delta\eta = \eta(track) - \eta(\vec{v})$, $\Delta\phi = \phi(track) - \phi(\vec{v})$, and \vec{v} is an approximation of the B direction of flight defined as:

$$\begin{aligned} v_x &\equiv x_{sv} - x_{pv} \\ v_y &\equiv y_{sv} - y_{pv} \\ v_z &\equiv \frac{\sqrt{v_x^2 + v_y^2}}{\cot(\theta)}, \end{aligned} \quad (6.7)$$

where $x_{sv}(x_{pv})$ and $y_{sv}(y_{pv})$ are the x and y coordinates for the secondary (primary) vertex and θ is the angle between the momentum vector of the secondary vertex tagged jet and the z -axis. Figure 6-4 shows the ΔR distribution for B and primary tracks in the muon and electron $b\bar{b}$ Monte Carlo samples. The ΔR distributions of B decays and primary tracks are clearly different. The shape of the distributions at low values of ΔR are sculpted by the square root in the definition of the variable.

The ΔR distributions for tracks in the inclusive electron sample are different from the distributions for tracks in the inclusive muon sample. In particular tracks tend to be at a larger ΔR in the electron sample as compared to tracks in the muon sample. This is a reflection of the fact that there are different selection criteria for electrons and muons. The electron candidates must satisfy the requirement that there be very little energy deposited near the electron track in the hadronic calorimeter. This requirement effectively isolates the electron track from the hadrons in the event, increasing the ΔR between the electron and the hadrons and thus also increasing, on average, the ΔR between the B flight direction and hadron tracks. In fact we would expect that this same effect would lead to slightly more peaking in the r distribution for B daughters in electron events as compared to muon events, which can also be seen in Figure 6-3.

This effect is small in the probability distributions, especially for the r variable, but more importantly exhibits a correlation between the r and ΔR probability distributions. As will be seen in the next section, we divide the data into ΔR regions and parameterize the probability distributions in r for each region. These parameterized probabilities are the same for muons and electrons. The probability that a track is a B decay product as a function of ΔR is shown in Figure 6-4. Again we see a clear dependence on the probability distribution, allowing us to differentiate B daughters from primary tracks on the basis of ΔR .

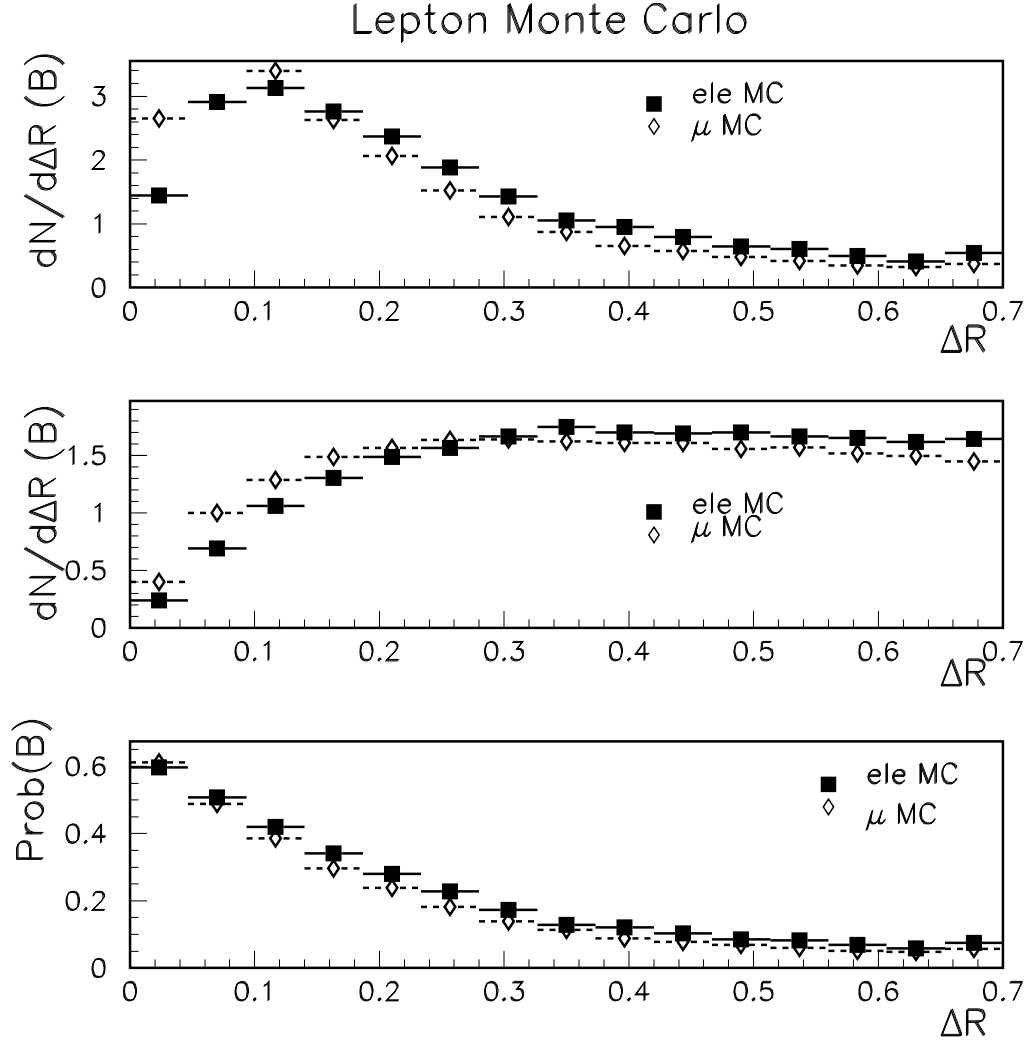


Figure 6-4: The distribution over ΔR for B meson daughters and primary tracks for electron and muon Monte Carlo samples. Tracks in the secondary vertex tag are not included in the plot. The top plot is the ΔR distribution for B daughters, the middle plot is the ΔR distribution for tracks which are not B daughters and the bottom plot is the probability that a track is a B daughter as a function of ΔR .

6.2.2 Parameterization of the Probability Distributions

We divided the electron Monte Carlo into four ΔR regions and computed the probability for a track to be a B daughter as a function of r in each ΔR region. We parameterized these probability distributions by

$$p_B(r; a < \Delta R < b) = \frac{(p_3 e^{-p_1 x^{p_5}} + p_4 e^{-p_2 x^{p_6}})}{(p_3 + p_4)}, \quad (6.8)$$

where p_1, p_2, p_3, p_4, p_5 , and p_6 are fit parameters and the form of the parameterization is arbitrary. The parameterized probability distributions are shown in Figure 6-5. By using a different probability distribution in r for each ΔR region, the correlation between the two variables is accounted for. By using a parameterization, the algorithm is not as sensitive to fluctuations due to binning and finite statistics in the Monte Carlo. We can see that the probability that a track is a B daughter as a function of r is nearly the same for the electron and muon samples in each ΔR region.

Lepton Monte Carlo

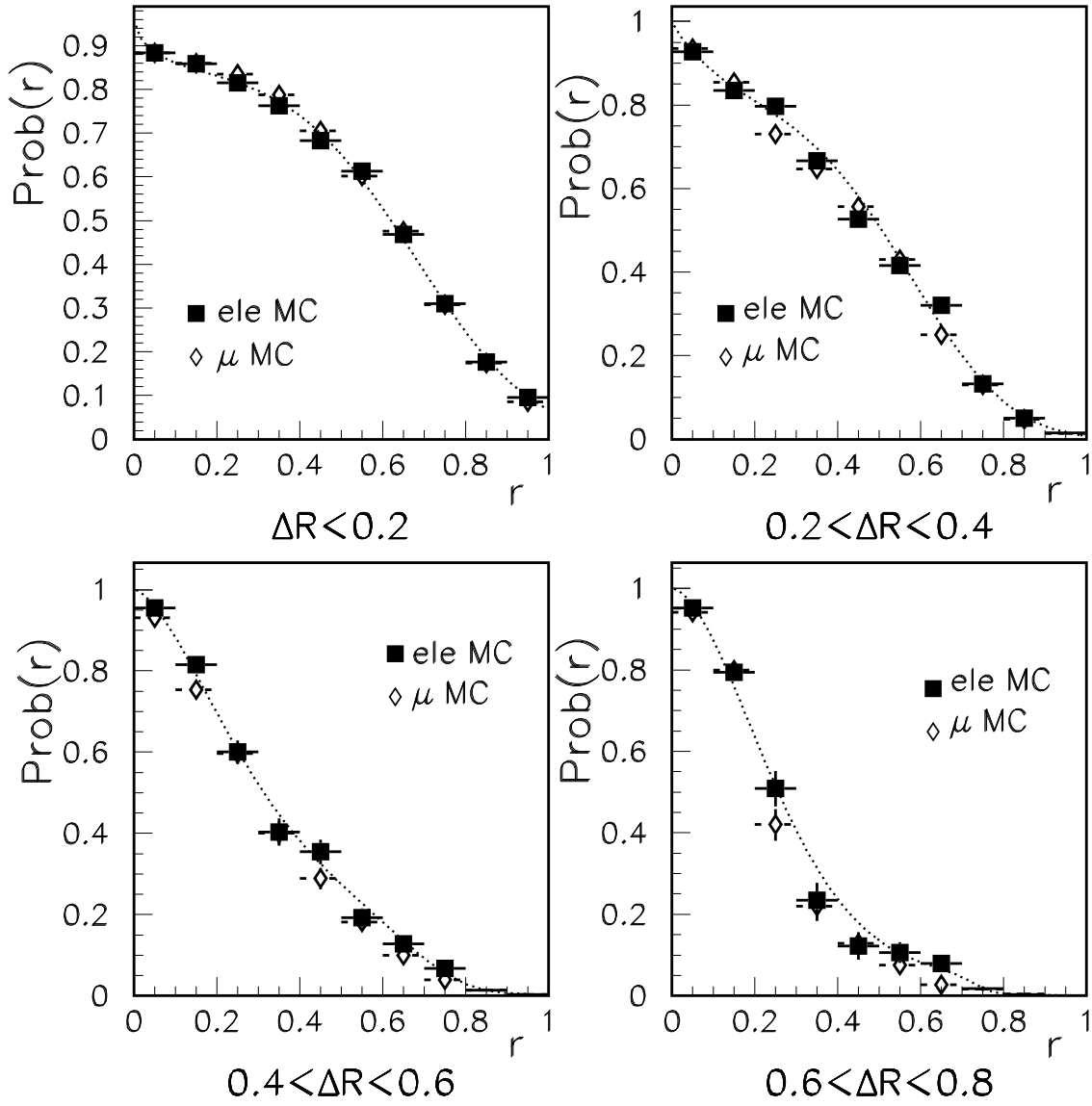


Figure 6-5: The probability that a track is a B daughter as a function of r for four different ΔR regions. The probability distributions determined from the electron and muon Monte Carlo samples as well as the parameterizations are shown.

6.2.3 L_{xy} Dependence of the Probability Distributions

When a secondary vertex is a large distance from the primary vertex in the transverse plane, it is very unlikely that a track originating from one of the vertices will have a small impact parameter with respect to the other vertex. We therefore would expect the r distribution for B daughter tracks and primary tracks to have different shapes at different L_{xy} values. However, Figure 6-6 shows that the distributions in r change in such a way as to leave the probability distribution $p_B(r)$ invariant with respect to large changes in L_{xy} .

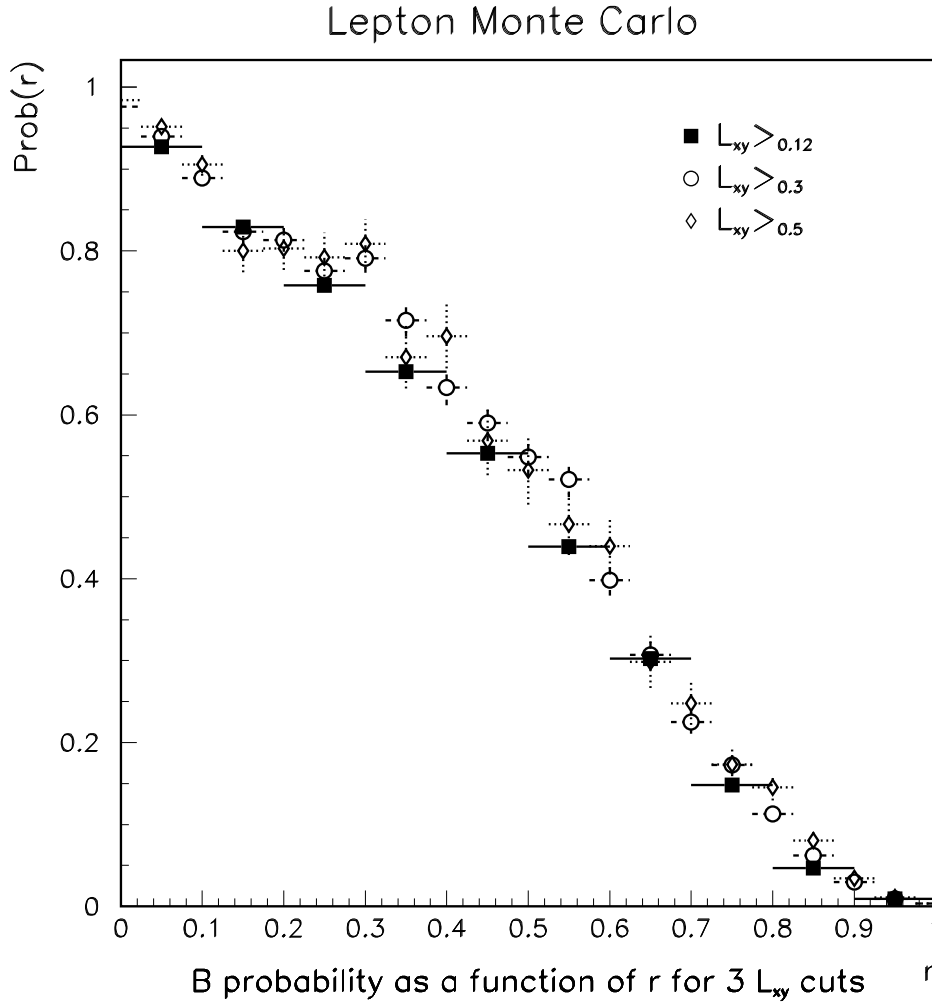


Figure 6-6: The probability that a track is a B daughter as a function of r for three different L_{xy} cuts.

6.2.4 Voting Algorithm

In order to determine the production flavor of a B meson associated with a secondary vertex we consider the collection of tracks within a cone of radius 0.7 about the B flight direction as defined in Equation 6.7. Tracks inside of this cone must satisfy the following requirements in order to be allowed to vote in the SST algorithm:

- The transverse momentum of the track, p_t , must exceed 0.4 GeV.
- There must be at least two hits in the SVX.
- The Impact Parameter Significance of the track with respect to the primary vertex must be less than 3.0.
- The track helix should exit the CTC (the exit radius should be at least 130 cm).
- There should be at least two hits in two axial superlayers and two hits in two stereo superlayers in the CTC.
- The probability that the track is a B daughter, as computed from the r and ΔR value of the track, is less than 0.3.

The sum of the charge of the tracks that satisfy these requirements is the production flavor tag.

As explained in appendix A, the proper measure of the flavor tagger effectiveness is ϵD^2 . We optimized the voting algorithm with respect to the probability cut, p_{cut} , by maximizing ϵD^2 in the Monte Carlo. The Monte Carlo relationship between ϵD^2 and the value of the probability cut is shown in Figure 6-7.

We considered a large number of other SST algorithms including single track algorithms and weighted sum algorithms but found no algorithm that was more effective than the voting algorithm.

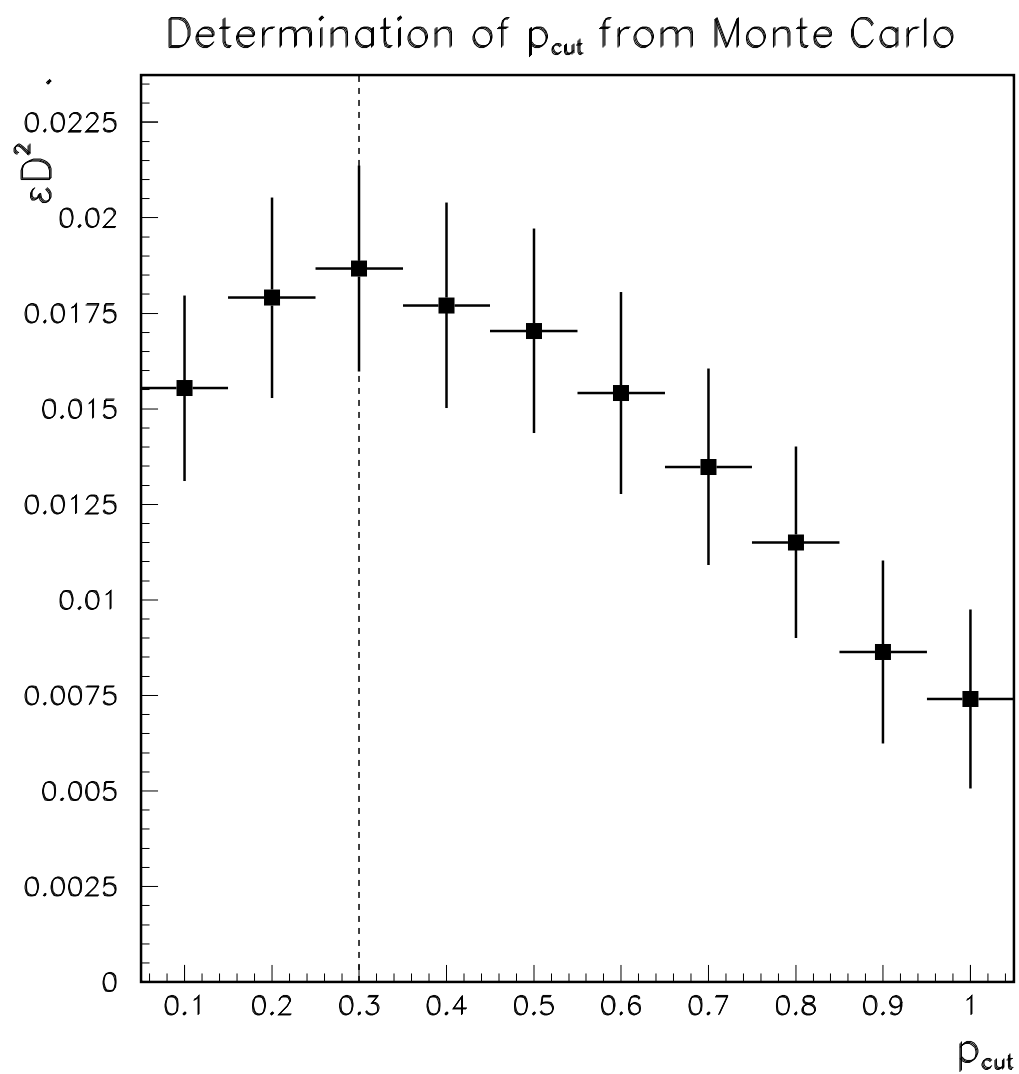


Figure 6-7: The value of the cut on B probability (p_{cut}) was determined by maximizing ϵD^2 in the electron Monte Carlo. The dotted line indicates the value of 0.3 which is used in the voting algorithm.

6.2.5 Charged and Neutral B Mesons and SST

As explained in section 3.3.2, the correlation between the charge of SST tracks and the production flavor of a B meson is reversed for charged B mesons with respect to neutral B mesons. The trigger lepton and SST charge-flavor correlated tracks have the same sign when the secondary vertex is due to the decay of an unmixed neutral B meson while they have opposite signs when the secondary vertex is due to a charged B meson.

The strength of the charge-flavor correlations also depends on the charge of the decaying B mesons. If, during fragmentation, a strange quark rather than a light quark is pulled from the sea, a charged B^+ is produced with a charged fragmentation hadron (K^-) of the proper sign, but a neutral B meson is produced with a neutral K^0 . In this case, the K^0 does not contribute charge to the SST algorithm, and the algorithm is less likely to find reconstructed tracks of the right charge-flavor correlation. Therefore, the dilution for charged B mesons exceeds the dilution for neutral B mesons, as was found in references [32] and [33].

6.2.6 Effect of Tagging on B Daughters in the Voting Algorithm

The probability of tagging on a B daughter is well defined for single track SST algorithms. In our case we must be careful to define what we mean by “tagging on B daughters” and “tagging on primary tracks.” We would like to define these terms so that they are mutually exclusive and B daughters change the outcome of the SST algorithm when tagging on B daughters occurs. We say that we have tagged on B daughters when the sign of the SST tag has been changed by the inclusion of B daughters in the production flavor tag. In other words, it is when the voting SST charge would be a different sign (or there be no flavor tag at all) if the B voters were removed from the sum in Equation 6.3. When we have not tagged on B daughters we say that we have tagged on primary tracks. With these definitions, the two categories are exclusive and the B daughters are considered an issue only when they have an

impact on the tagging. Because the SST algorithm is restricted to tracks with a small probability of being a B decay product, the probability that more than one B daughter contributes to the SST charge is small. When there is only one B daughter included in the SST charge, there are only a few cases in which it will have an impact on the charge determination. If the charges of the other tracks that contribute to the SST algorithm sum to zero, then the B daughter will determine the production flavor tag. In this case there must be either no other tracks or an even number of primary tracks that contribute to the SST algorithm. If there are an odd number of primary tracks that contribute to the SST charge, then the B daughter will have no effect unless the charges of the primary tracks sum to ± 1 and the B daughter is of the opposite charge of the sum. In this case, the B daughter removes the tag.

In Figure 6-8 we show the probability of tagging on a B daughter as a function of L_{xy} for the voting and minimum p_t^{rel} algorithms. The minimum p_t^{rel} algorithm is, as expected, much more likely than the voting algorithm to select the production flavor of B mesons based on daughter tracks.

Because we defined tagging on B daughters and tagging on primary tracks in a mutually exclusive way, we can treat tagging on B daughters as a sample composition issue. Rather than considering four $b\bar{b}$ sources¹ we consider six sources: B_{SST-B}^0 , B_{SST-F}^0 , B_{SST-B}^+ , B_{SST-F}^+ , B_s , and Λ_b . B_{SST-B}^0 denotes neutral B meson vertices for which the production flavor is determined by tagging on B daughters and B_{SST-F}^0 denotes neutral B mesons that are tagged on primary tracks. The charged subsamples, B_{SST-B}^+ and B_{SST-F}^+ , are defined similarly. We have split the neutral and charged B meson sources into two subsources each. Every source can be thought of as contributing, to the measured asymmetry $A^{measured}$, an asymmetry (A_{source}), weighted by a dilution (D_{source}) and the fraction of events (f_{source}) due to that source:

$$A^{measured} = \sum_{sources} A_{source} D_{source} f_{source}. \quad (6.9)$$

The B_{SST-F}^0 sample, for example, contributes the oscillatory asymmetry shown in Equation 3.8. Because the mesons in the B_{SST-F}^0 and B_{SST-F}^+ samples are produc-

¹There are four b hadrons that provide secondary vertices: B^0 , B^+ , B_s , and Λ_b .

tion flavor tagged by primary tracks only, the SST dilutions in these samples are independent of proper time. We absorbed daughter-tagging into the definition of the dilutions for the other particle species, allowing them to have a pseudo-proper time dependence, which we modeled as linear, based on Monte Carlo results, as will be shown in section 7.7. In this section we will concentrate on the asymmetry, dilution, and fraction of events due to B_{SST-B}^0 and B_{SST-B}^+ , the daughter-tagged samples.

The probability of tagging on a B daughter has a pseudo-proper time dependence, as can be seen in Figure 6-9 for neutral and charged B mesons. This dependence is a reflection of the fact that the probability of tagging on B daughters depends on L_{xy} . As the proper decay distance increases, the likelihood that a daughter track points to the primary vertex decreases due to a diminishing phase space. We parameterized the probability of tagging on B daughters as a function of pseudo-proper time as a sum of a decaying exponential with a flat asymptote.

The asymmetries, A_{SST-B^0} for neutral mesons and A_{SST-B^+} for charged mesons, determined as usual by comparing the (daughter-tagged) SST charge with the trigger lepton charge, are negative. We can define the “true asymmetries” for these samples to be given by $A_{SST-B^0}^{true} = -1$ and $A_{SST-B^+}^{true} = -1$. We absorb the pseudo-proper time shapes in the observed asymmetries into definition of the dilutions:

$$A_{SST-B^0} = A_{SST-B^0}^{true} D_{SST-B^0} \quad (6.10)$$

$$A_{SST-B^+} = A_{SST-B^+}^{true} D_{SST-B^+}. \quad (6.11)$$

It is convenient to make this definition when constructing the fitter. The daughter tagging dilution is therefore given by $D_{SST-B^0} = -A_{SST-B^0}$ and $D_{SST-B^+} = -A_{SST-B^+}$. Figure 6-10 shows A_{SST-B^0} and A_{SST-B^+} as determined from the electron and muon Monte Carlo samples.

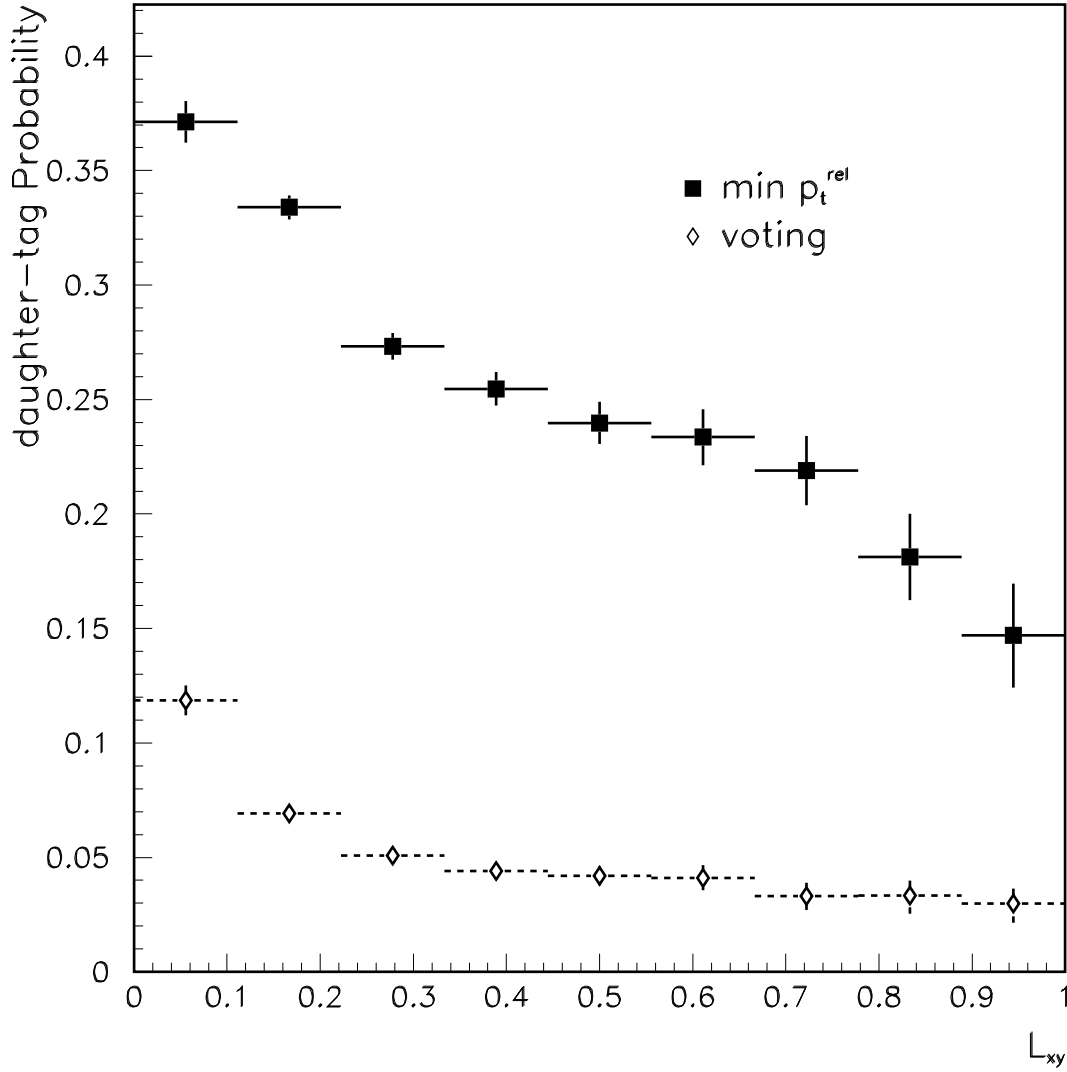


Figure 6-8: The squares are the probability, as a function of L_{xy} , that the track selected by the minimum p_t^{rel} algorithm as the SST flavor tagger is really a B daughter and not a primary particle, determined from the inclusive electron Monte Carlo. The diamonds are the probability that a SST charge in the voting algorithm is determined by B daughters as a function of L_{xy} .

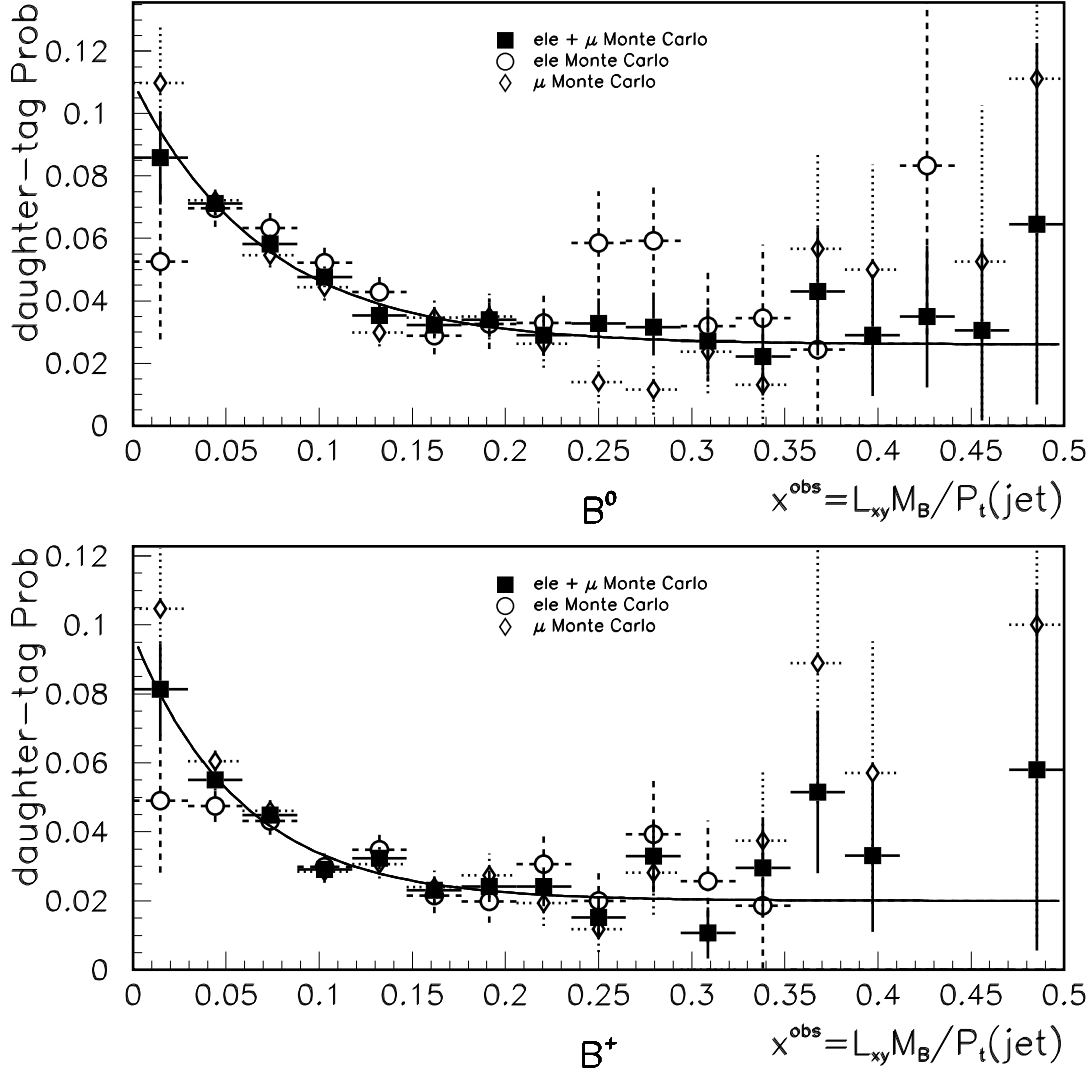


Figure 6-9: The probabilities of tagging on a B daughter as a function of pseudo-proper time given that the SST tag is associated with a B^0 (top) and B^+ (bottom) meson.

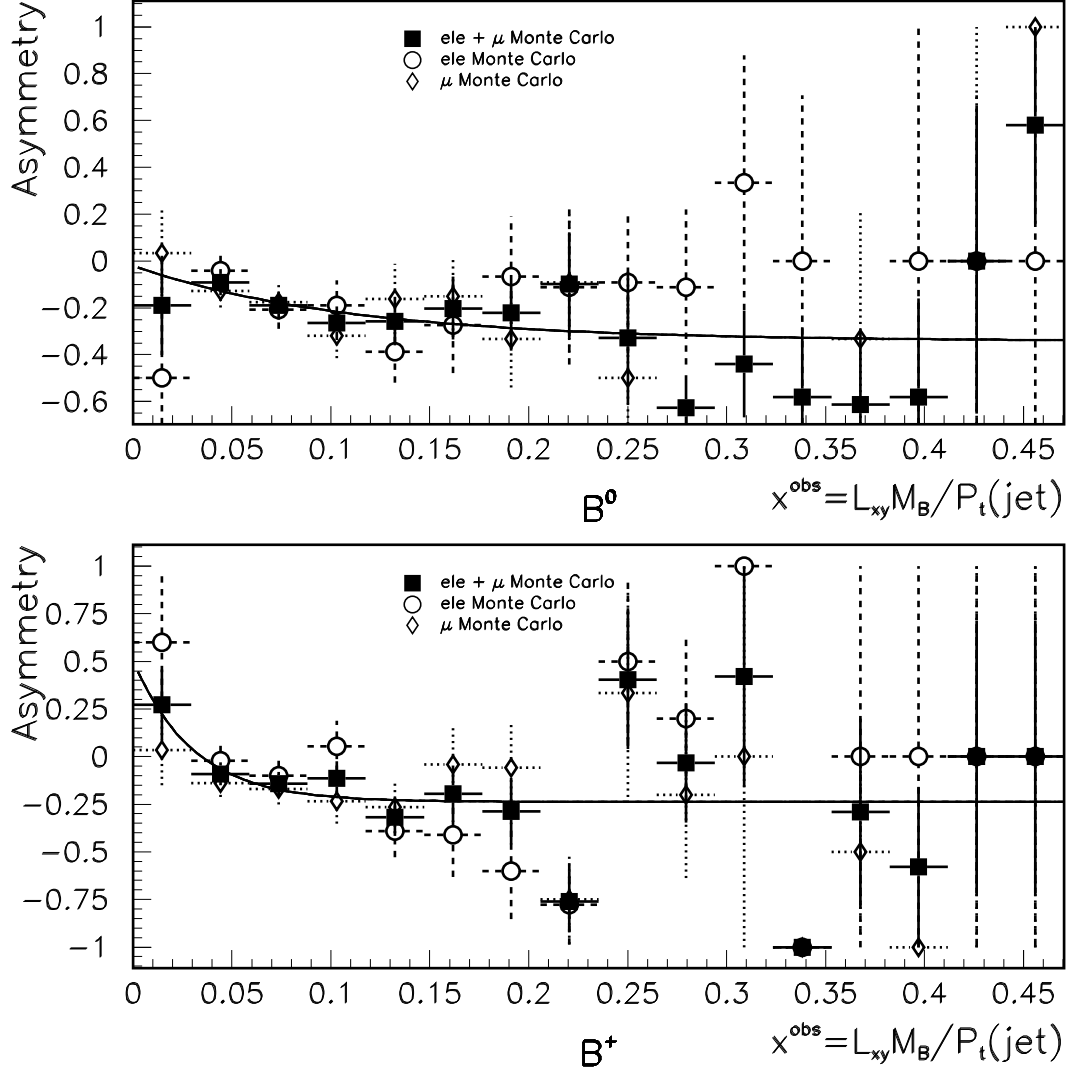


Figure 6-10: The asymmetry for daughter-tagged B^0 (top) and B^+ (bottom) events in the lepton Monte Carlo as a function of pseudo-proper time. The fits, an exponential added to a constant, were used as the shape for the fitter that we used to determine Δm_d .

6.3 Measured Asymmetries

We applied the voting algorithm to the electron and muon data samples in order to determine a measured asymmetry as a function of pseudo-proper time. The measured asymmetries can be seen in Figure 6-11. A clear neutral B oscillation can be seen in both data samples.

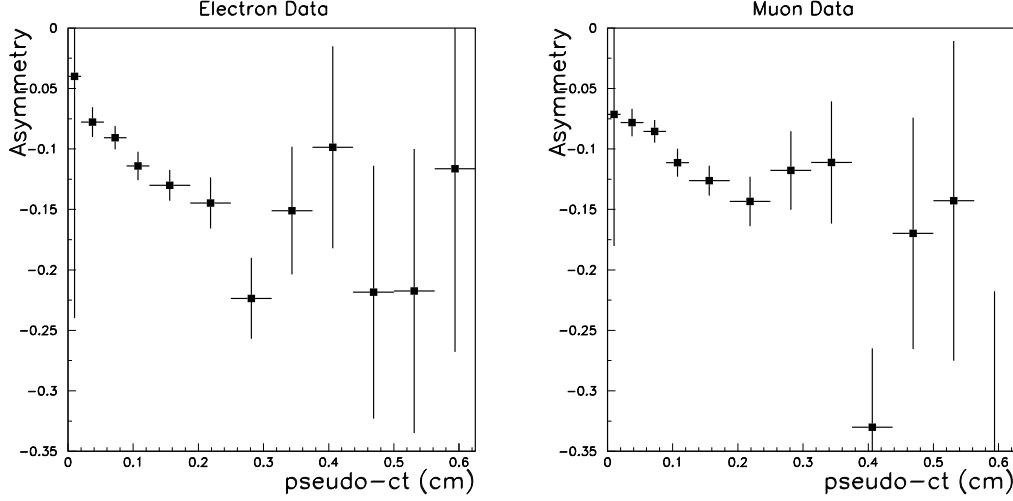


Figure 6-11: The measured asymmetries as a function of pseudo-proper time in the electron (left) and muon (right) data samples.

We fit these distributions in order to extract the value of Δm_d . In the fitting process we also determined the neutral and charged dilutions and the wrong-sign fake fraction in the muon sample.

Chapter 7

The Fit

We extracted the value of Δm_d from the measured asymmetries shown in Figure 6-11. To do this we computed the expected asymmetry as a function of pseudo-proper time for given values of Δm_d , the charged and neutral B dilutions, and the wrong-sign muon fake fraction. We then employed a least squares fit in order to determine the mixing frequency. In this chapter we show the result of fitting the measured asymmetries with the expected asymmetries to determine Δm_d . We also show how the different sources of secondary vertices contribute to the expected pseudo-proper time dependent asymmetries.

7.1 The Fitting Method

We can compute the probability of finding the sign of the SST charge, Q_{sst} , and sign of the trigger lepton's charge to be the same, $\bar{\rho}_{ss}(t')$, and different, $\bar{\rho}_{os}(t')$, as a function of pseudo-proper time, t' , using the sample composition, Δm_d , and the SST dilutions as inputs. The expected asymmetry as a function of pseudo-proper time is related to $\bar{\rho}_{ss}$ and $\bar{\rho}_{os}$ by

$$A_{par}(t') = \frac{\bar{\rho}_{ss}(t') - \bar{\rho}_{os}(t')}{\bar{\rho}_{ss}(t') + \bar{\rho}_{os}(t')}. \quad (7.1)$$

Note that A_{par} is a function of the unknown parameters, Δm_d , the neutral B meson dilution, the charged B meson dilution, and the muon wrong sign fake fraction. This

function is different for the electron and muon event samples due to difference in the sample compositions. We denote the expected parameterized asymmetry for the electron and muons samples to be A_{par}^e and A_{par}^μ respectively. Similarly, we denote the measured asymmetry in the data-averaged center of the i^{th} pseudo proper-time bin $A_{measured}^e(t'_i)$ and $A_{measured}^\mu(t'_i)$ for the electron and muon event samples respectively. In order to determine the value of the unknown parameters, we minimize, with respect to those parameters,

$$\chi^2 = \sum_e \frac{(A_{par}^e(t'_i) - A_{measured}^e(t'_i))^2}{\sigma^2(A_{par}^e, N_i^e)} + \sum_\mu \frac{(A_{par}^\mu(t'_i) - A_{measured}^\mu(t'_i))^2}{\sigma^2(A_{par}^\mu, N_i^\mu)}, \quad (7.2)$$

where N_i^e is the number of events in the i^{th} pseudo-proper time bin for the electron event sample, N_i^μ is the number of events in the i^{th} pseudo-proper time bin for the muon event sample, and

$$\sigma(A_{par}, N) = \sqrt{\frac{1 - A_{par}^2}{N}}. \quad (7.3)$$

Defined this way, σ is an unbiased estimate of the error on the asymmetry (see Appendix A). If we had used the measured asymmetry in 7.3 rather than A_{par} , we would have biased the determination of Δm_d . This is because the error determined from the measured asymmetry is smaller when the measured asymmetry fluctuates away from zero and larger when the measured asymmetry fluctuates towards zero in each pseudo-proper time bin.

In order to determine Δm_d , we therefore need to first determine the expected same-sign and opposite-sign probability density functions, $\bar{\rho}_{ss}$ and $\bar{\rho}_{os}$. We note that if we can determine the probability densities as a function of proper time, we can transform these to functions of pseudo-proper time using the appropriate k -factor distributions and the proper-time resolution function. We therefore concentrate on constructing the proper-time dependent same-sign and opposite-sign probability density functions.

The proper time dependent probability density functions can be expanded over the different particle species as follows:

$$\rho_{ss}(t) = \sum_{ptyp} \rho_{ss}(t; ptyp) f(ptyp) \quad (7.4)$$

$$\rho_{os}(t) = \sum_{ptyp} \rho_{os}(t; ptyp) f(ptyp) \quad (7.5)$$

where $ptyp$ is an index that indicates the particle type, B^0 , B^+ , B_s , Λ_b , D^0 , D^+ , and D_s , and $f(ptyp)$ is the fraction of secondary vertices due to the particle type. For the particle species that contain a bottom quark we can decompose $f(ptyp)$ into two factors:

$$f(ptyp)_{b\bar{b}} = f_{b\bar{b}} f(ptyp; b\bar{b}), \quad (7.6)$$

where $f_{b\bar{b}}$ is the $b\bar{b}$ fraction and $f(ptyp; b\bar{b})$ is the fraction of secondary vertices due to the decay of bottom hadrons of the type $ptyp$. Similarly for $c\bar{c}$,

$$f(ptyp)_{c\bar{c}} = f_{c\bar{c}} f(ptyp; c\bar{c}). \quad (7.7)$$

We can express the fractions $f(ptyp; b\bar{b})$ and $f(ptyp; c\bar{c})$ in terms of the hadron production fractions (f_u , f_d , f_s , and f_{baryon}) and the particle lifetimes:

$$f(ptyp; b\bar{b}) = \frac{f_{ptyp} \tau_{ptyp}}{\sum_{ptyp; b\bar{b}} f_{ptyp} \tau_{ptyp}} \quad (7.8)$$

$$f(ptyp; c\bar{c}) = \frac{f_{ptyp} \tau_{ptyp}}{\sum_{ptyp; c\bar{c}} f_{ptyp} \tau_{ptyp}}, \quad (7.9)$$

where f_{ptyp} is the appropriate hadron production fraction and τ_{ptyp} is the lifetime for particle $ptyp$. The sum in 7.8 is over $b\bar{b}$ particle species only and the sum in 7.9 is over the $c\bar{c}$ particle species only. The production fractions are weighted according to the lifetimes since we are only concerned with semi-leptonic decays, and we are using the fact that the semi-leptonic partial widths are nearly the same for all the particle species, and thus the semi-leptonic branching fractions are proportional to the lifetimes.

Once the expected proper time dependent probability distributions are determined, we can use Equation 5.7 to determine the probability distributions as functions of t' . The integral in k is approximated by a sum over the appropriate histograms shown in Figures 5-3 and 5-4. We have:

$$\bar{\rho}_{ss}(t) = \sum_{ptyp} f(ptyp) \sum_j \Delta k D(k_j; ptyp) \int dt R(t' - t/k_j) \rho_{ss}(t; \Delta m_d, ptyp) \quad (7.10)$$

$$\bar{\rho}_{os}(t) = \sum_{ptyp} f(ptyp) \sum_j \Delta k D(k_j; ptyp) \int dt R(t' - t/k_j) \rho_{os}(t; \Delta m_d, ptyp). \quad (7.11)$$

7.2 The Probability Density Functions for B^0 Mesons

The unmixed and mixed probability density functions for B^0 mesons are given by Equations 1.19 and 1.20. The same-sign and opposite-sign probability density functions for B^0 mesons that have been tagged on primary tracks is given by

$$\begin{aligned}\rho_{ss}^{SST-F}(t; \Delta m, B^0) &= (p_{tag}(1 - p_{w-lep}) + (1 - p_{tag})p_{w-lep})\rho_{mix} + \\ &\quad (p_{tag}p_{w-lep} + (1 - p_{tag})(1 - p_{w-lep}))\rho_{nomix} \\ \rho_{os}^{SST-F}(t; \Delta m, B^0) &= (p_{tag}(1 - p_{w-lep}) + (1 - p_{tag})p_{w-lep})\rho_{nomix} + \\ &\quad (p_{tag}p_{w-lep} + (1 - p_{tag})(1 - p_{w-lep}))\rho_{mix},\end{aligned}\tag{7.12}$$

where $p_{tag} = \frac{1+D_0}{2}$ is the probability that the production flavor tag is correct, expressed in terms of the neutral B meson dilution, D_0 , when the production flavor tag is determined by primary tracks, and p_{w-lep} is the probability that the decay flavor tag is incorrect. The same sign and opposite sign probabilities when the SST tag is determined by B daughters are given by

$$\begin{aligned}\rho_{os}^{SST-B} &= \frac{e^{-t/\tau}}{\tau}((1 - p_{w-lep})p_{tag}^{SST-B} + (p_{w-lep})(1 - p_{tag}^{SST-B})) \\ \rho_{ss}^{SST-B} &= \frac{e^{-t/\tau}}{\tau}((1 - p_{w-lep})(1 - p_{tag}^{SST-B}) + p_{w-lep}p_{tag}^{SST-B}),\end{aligned}\tag{7.13}$$

where $p_{tag}^{SST-B} = \frac{1+D_{SST-B^0}}{2}$ is the probability that the daughter-tagged SST algorithm provides the expected correlation, as determined by Equation 6.10. The probability density functions are then

$$\begin{aligned}\rho_{ss}(t; B^0) &= (1 - p_{SST-B^0})\rho_{ss}^{SST-F} + p_{SST-B^0}\rho_{ss}^{SST-B} \\ \rho_{os}(t; B^0) &= (1 - p_{SST-B^0})\rho_{os}^{SST-F} + p_{SST-B^0}\rho_{os}^{SST-B},\end{aligned}\tag{7.14}$$

where p_{SST-B^0} is the probability that the SST tag is determined by B daughters.

7.3 The Probability Density Functions for B^+ Mesons

Charged B mesons obviously do not undergo mixing. The expected correlation between the lepton and the SST charge for charged B mesons is opposite that of neutral

B mesons (see Figure 3-3). The probability density functions are thus given by

$$\begin{aligned}\rho_{os}(t; B^+) &= \frac{e^{-t/\tau}}{\tau}((1 - p_{w-lep})p'_{tag} + (p_{w-lep})(1 - p'_{tag})) \\ \rho_{ss}(t; B^+) &= \frac{e^{-t/\tau}}{\tau}((1 - p_{w-lep})(1 - p'_{tag}) + p_{w-lep}p'_{tag})\end{aligned}\quad (7.15)$$

where we have defined p'_{tag} to be

$$p'_{tag} = \frac{1 + ((1 - p_{SST-B^+})D_+ + p_{SST-B^+}D_{SST-B^+})}{2}, \quad (7.16)$$

where D_+ is the charged B dilution when tagging on primary tracks, D_{SST-B^+} is the “dilution” when tagging on B daughters, and p_{SST-B^+} is the probability of tagging on a B daughter when the vertex is due to a charged B meson.

7.4 The Probability Density Functions for B_s Mesons

The B_s meson will also undergo mixing but with a much higher oscillation frequency. The many oscillations in each bin average out to a zero asymmetry per bin. We therefore set the same sign and opposite sign probability density functions to be the same:

$$\rho_{ss} = \rho_{os} = \frac{e^{-t/\tau}}{2\tau} \quad (7.17)$$

7.5 The Probability Density Functions for Λ_b Baryons

We wish to compute the probability that we find a Λ_b at a proper time t under the assumption that it is identified as a B meson. The mass of the Λ_b is different from the mass of the B and we therefore need correct the lifetime distribution to account for this difference. We should also have corrected for this effect when constructing the B_s meson probability density function as well, but the $B_s - \Lambda_b$ mass difference is a fourth as large and was therefore neglected. We call y the Λ_b proper time variable and t the proper time variable under the assumption that the decaying particle is a B meson. We note that in terms of measurable quantities,

$$y = \frac{L_{xy}M_{\Lambda_b}}{p_t} \quad (7.18)$$

while we have as usual

$$t = \frac{L_{xy} M_B}{p_t}. \quad (7.19)$$

We can relate the variables y and t by

$$y = \frac{m_\Lambda}{m_B} t, \quad (7.20)$$

and therefore transform the probability distribution function for finding a Λ_b as a function of y , governed by the lifetime of the Λ_b , to a function of t as follows:

$$\rho(t) = \frac{d}{dT} P(t < T) = \frac{d}{dT} P\left(\frac{m_\Lambda}{m_B} t < \frac{m_\Lambda}{m_B} T\right) = \frac{dY}{dT} \frac{d}{dY} P(t < T) = \frac{m_\Lambda}{m_B} \rho(y(t)). \quad (7.21)$$

In the case of

$$\rho(y) = \frac{e^{-y/\tau}}{\tau} \quad (7.22)$$

the transformation yields

$$\rho(t) = \frac{e^{-t/\tau'}}{\tau'} \quad (7.23)$$

where

$$\tau' = \frac{m_B}{m_\Lambda} \tau. \quad (7.24)$$

We must therefore scale the lifetime according to the ratio of masses. This issue will come up again when we compute the probability density function for the prompt charm particle species. The Λ_b probability density functions are given by

$$\begin{aligned} \rho_{ss}(t; \Lambda_b) &= \frac{e^{-t/\tau'}}{\tau'} ((1 - p_{w-lep}) p_{tag} + (p_{w-lep})(1 - p_{tag})) \\ \rho_{os}(t; \Lambda_b) &= \frac{e^{-t/\tau'}}{\tau'} ((1 - p_{w-lep})(1 - p_{tag}) + p_{w-lep} p_{tag}), \end{aligned} \quad (7.25)$$

where p_{tag} is determined from the production flavor tagging dilution for the case of secondary vertex tagging on Λ_b baryons.

7.6 The Probability Density Functions for Prompt Charm Mesons

All three of the prompt charm probability density functions are very similar, differing only in the sign of the asymmetry and the value of the lifetimes and masses. We

therefore present all three together. As in the Λ_b case, the lifetimes must be scaled by the ratio of the mass of the B meson to the mass of the charm meson. The probability density functions are given by

$$\begin{aligned}
\rho_{ss}(t, D_u) &= \rho_1(t; D_u) \\
\rho_{os}(t, D_u) &= \rho_2(t; D_u) \\
\rho_{ss}(t, D_d) &= \rho_2(t; D_d) \\
\rho_{os}(t, D_d) &= \rho_1(t; D_d) \\
\rho_{ss}(t, D_s) &= \rho_1(t; D_s) \\
\rho_{os}(t, D_s) &= \rho_2(t; D_s),
\end{aligned} \tag{7.26}$$

where we have defined

$$\begin{aligned}
\rho_1(t; D_i) &= \frac{e^{-t/\tau'_i}}{\tau'_i} ((1 - p_{w-lep})p_{tag} + (p_{w-lep})(1 - p_{tag})) \\
\rho_2(t; D_i) &= \frac{e^{-t/\tau'_i}}{\tau'_i} ((1 - p_{w-lep})(1 - p_{tag}) + p_{w-lep}p_{tag}).
\end{aligned} \tag{7.27}$$

7.7 Dilutions

The probability that a lepton provides an incorrect determination of the B decay flavor is determined from the sample composition, with the muon fake fraction left undetermined. The probability that a flavor tag at the time of production is correct depends on the SST dilution and is given by

$$p_{tag} = \frac{1 + D}{2} \tag{7.28}$$

where the dilution is different for each particle species. Most of the SECVTX tags in the sample are due to decaying B^0 and B^\pm mesons. We let the neutral B dilution (D_0) and the charged B dilution (D_+) float in the fit that we used to determine Δm_d . Because daughter-tagging effects are explicitly extracted for B^0 and B^+ , these dilutions are independent of t' . We fit the other particle species dilutions with a linear function, as can be seen in Figure 7-1 for the $b\bar{b}$ particle species and in Figure 7-2 for the $c\bar{c}$ particle species. We fixed the slope of these dilutions to the Monte Carlo

values. We also fixed the ratio of the neutral B dilution to the particle dilution at $t' = 0.3$ cm. In other words, the offset of the dilutions are pegged to the neutral B dilution via the Monte Carlo ratio of dilutions, for particles other than B^0 and B^+ .

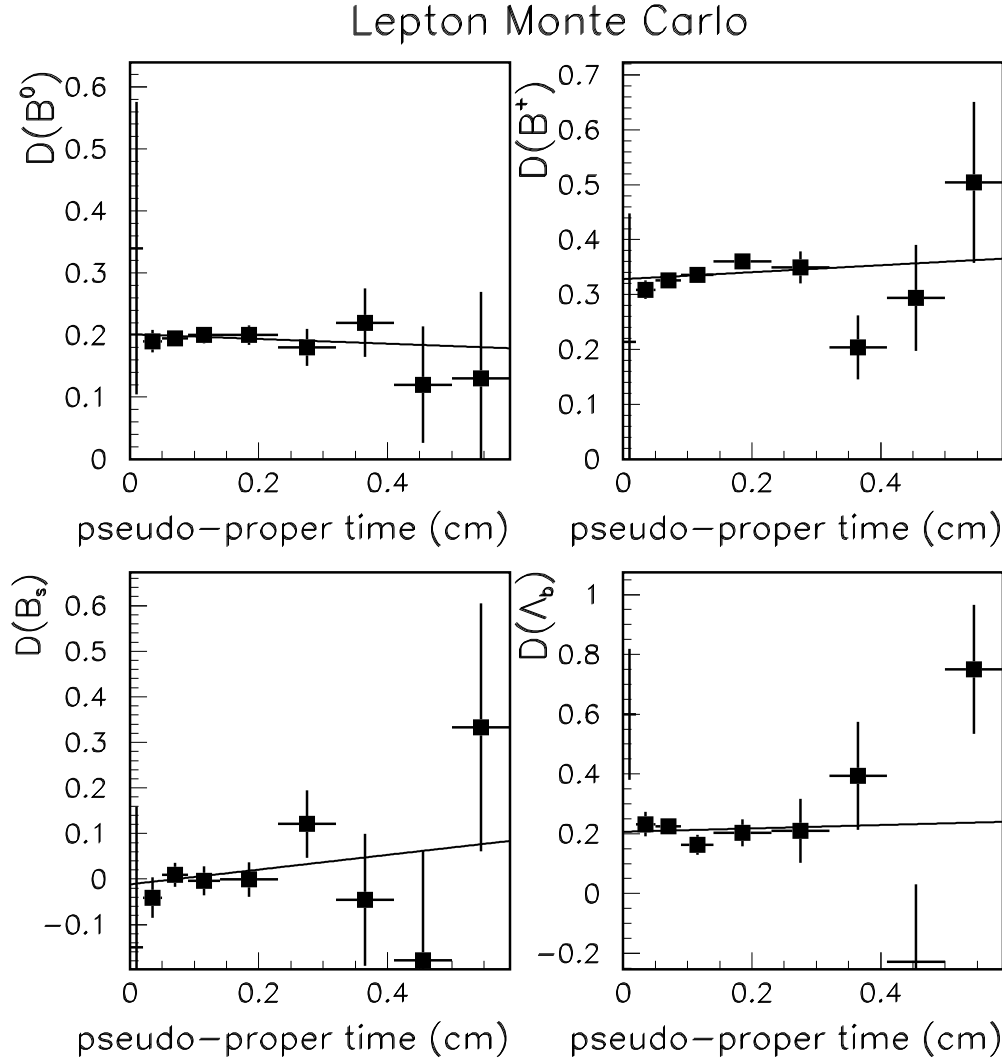


Figure 7-1: The dilution as a function of t' for $b\bar{b}$ particle species using the voting algorithm. Also shown are linear fits to the dilutions. The B^0 and B^+ dilutions have no t' dependence by construction (and the fits have no significant slopes).

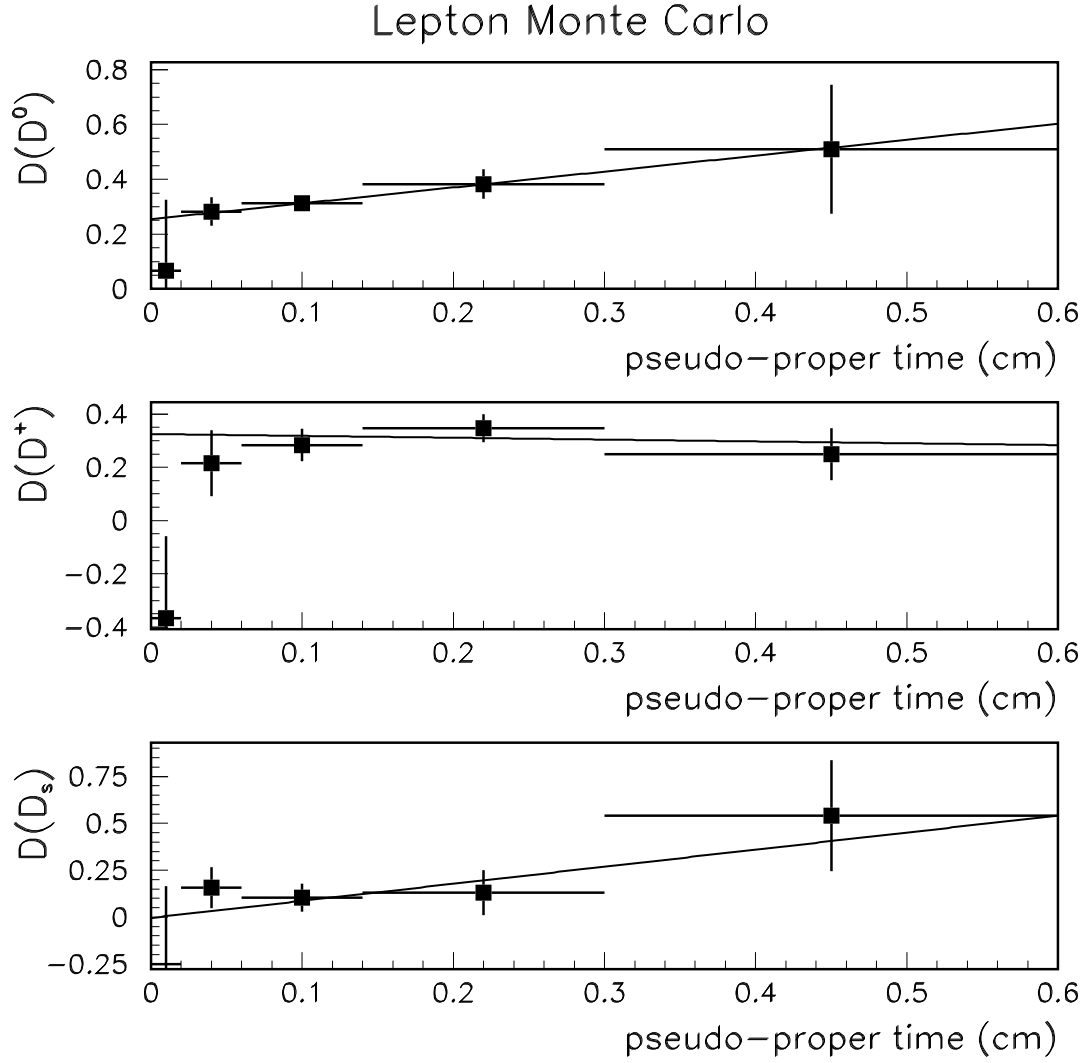


Figure 7-2: The dilution as a function of t' for $c\bar{c}$ particle species using the voting algorithm. These linear fits are used as the dilution shape in the determination of Δm_d .

7.8 Results

We fit the electron and muon data simultaneously by minimizing the χ^2 function shown in Equation 7.2 with respect to Δm_d , the neutral and charged B dilutions, and the wrong-sign muon fake fraction. The fit results are shown in Figures 7-3 and 7-4. The fit value of Δm_d is same in both plots because the parameters were determined in a single combined fit. We obtain

$$\Delta m_d = (0.42 \pm 0.09) \times (\text{ps})^{-1} \tag{7.29}$$

$$D_0 = 0.13 \pm 0.03$$

$$D_+ = 0.35^{+0.04}_{-.03}$$

$$f_{wsfake}^\mu = 0.02^{+.03}_{-.02}$$

where the quoted errors are statistical only.

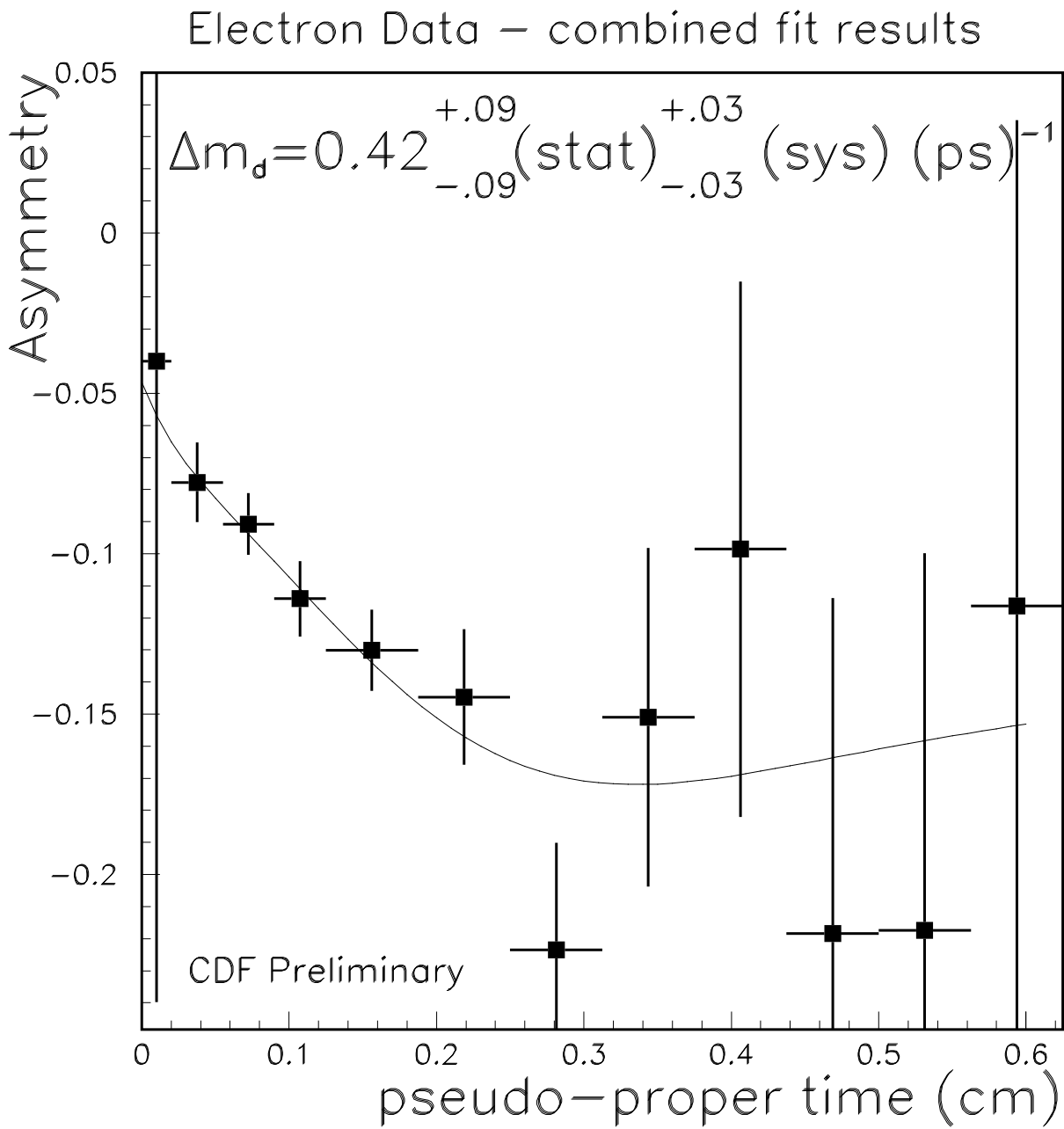


Figure 7-3: Fit results for the electron asymmetry as a function of t' from the combined electron and muon fit super-imposed over the measured asymmetries from the electron event sample.

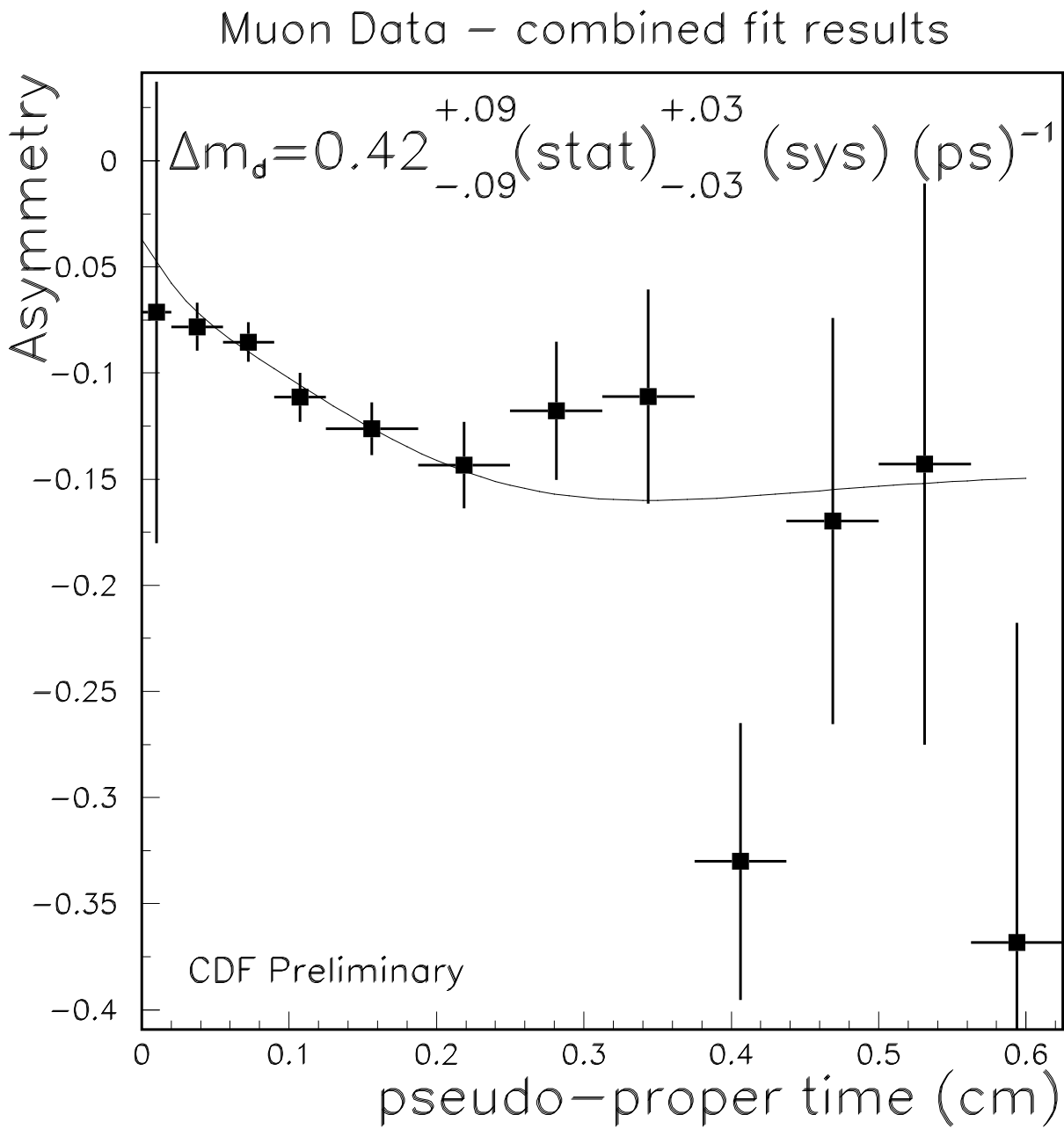


Figure 7-4: Fit results for the muon asymmetry as a function of t' from the combined electron and muon fit super-imposed over the measured asymmetries from the muon event sample.

Chapter 8

Systematic Uncertainties

In this chapter we present the effects of assumptions we have made in the construction of the same-sign and opposite-sign probability density functions in the fit. We have identified several different categories of assumptions that have a systematic effect on this analysis:

- The input parameters to the fit,
- The k -factor distributions,
- The resolution in L_{xy} ,
- The t' dependence of SST dilutions,
- The tagging on B daughters.

We treat each category separately.

8.0.1 Parameters

We call Δm_d , D_0 , D_+ , and f_{wsfake}^μ the “output parameters” of the fit and the parameters used for the computation of A_{par}^e and A_{par}^μ that were not determined from the fit the “input parameters.” Some of the input parameters are specific to this analysis. For example, the sample composition fractions and the parameterizations of the Monte Carlo based daughter-tagging probabilities were input parameters. In addition

to the parameter values, we have determined the errors on those values, and these errors should be reflected in the errors from the fit results. Other input parameters, such as the particle lifetimes, have been determined elsewhere, but still have errors that should be reflected in the determination of Δm_d . In some cases, different input parameters affect the same physical aspects described by the fitter, for example the B^0 lifetime and the hadronic fractions both affect the fraction of secondary vertices due to B^0 mesons as a function of t' . The method that we employed in order to estimate the systematic uncertainties accounted for these types of correlated effects. We did this by performing a fit in which we treated all of the parameters as input parameters. In this fit we simultaneously determined the four input parameters of the normal fit and the forty parameters (p_1, \dots, p_{40}) shown in the Tables 8.1 and 8.2. We added a new term to the χ^2 function shown in Equation 7.2 for the forty new output parameters. Each of these new terms were of the form

$$\frac{(p_i - \bar{p}_i)^2}{\sigma_i^2}, \quad (8.1)$$

where \bar{p}_i is the central value of the i^{th} parameter and σ_i is the error on that parameter. The χ^2 function therefore looks like:

$$\chi^2 = \sum_e \frac{(A_{par}^e(t'_i) - A_{measured}^e(t'_i))^2}{\sigma^2(A_{par}^e, N_i^e)} + \sum_\mu \frac{(A_{par}^\mu(t'_i) - A_{measured}^\mu(t'_i))^2}{\sigma^2(A_{par}^\mu, N_i^\mu)} + \Sigma, \quad (8.2)$$

where

$$\Sigma = \sum_{params} \frac{(p_i - \bar{p}_i)^2}{\sigma_i^2}. \quad (8.3)$$

We call the fit in which we minimize the χ^2 in Equation 8.2 the “super-parameter fit.”

The output parameters are determined from the super-parameter fit within an error, which we call $\sigma_{tot}^i(float)$ for the i^{th} parameter, where we have indicated that the forty parameters are floating in the fit. We are really only interested in three of these errors, $\sigma_{tot}^{\Delta m_d}(float)$, $\sigma_{tot}^{D_0}(float)$, and $\sigma_{tot}^{D^+}(float)$.

Next we fit the data using the χ^2 function shown in Equation 7.2 with the four original output parameters and forty input parameters. Rather than setting the input parameters to their central values, we use the values of the parameters determined

from the super-parameter fit. The errors on the output parameters from this fit are statistical, and we denote them $\sigma_{stat}^i(fixed)$, where we have indicated that the forty parameters were fixed in the fit. We determined the systematic error due to the forty input parameters from the relationship

$$\sigma_{sys} = \sqrt{\sigma_{tot}(float)^2 - \sigma_{stat}(fixed)^2}. \quad (8.4)$$

The systematic errors due to the input parameters can be found in Table 8.3.

parameter	value	positive error	negative error
$\tau_{B^0} \ 10^{-12}\text{s}$	1.54	0.03	0.03
τ_{B^0}/τ_{B^+}	1.07	0.03	0.03
$\tau_{B_s} \ 10^{-12}\text{s}$	1.54	0.07	0.07
$\tau_{\lambda_b} \ 10^{-12}\text{s}$	1.24	0.08	0.08
$\tau_{D^0} \ 10^{-12}\text{s}$	0.415	0.004	0.004
$\tau_{D^p} \ 10^{-12}\text{s}$	1.057	0.015	0.015
$\tau_{D_s} \ 10^{-12}\text{s}$	0.495	0.013	0.013
f_u	0.397	0.018	0.022
f_d	0.397	0.018	0.022
f_s	0.105	constrained by $\sum f = 1$	constrained by $\sum f = 1$
f_{bary}	0.101	0.039	0.031
p_{seq}^{ele}	0.06	0.01	0.01
f_{fake}^{ele}	0.004	0.002	0.002
f_{conv}	0.008	0.001	0.001
f_{seq}^{muo}	0.085	0.01	0.01
$M_{B^0} \ \text{GeV}$	5.279	0.002	0.002
$M_{B^p} \ \text{GeV}$	5.278	0.002	0.002
$M_{B_s} \ \text{GeV}$	5.369	0.002	0.002
$M_{\lambda_b} \ \text{GeV}$	5.624	0.009	0.009
$M_{D^0} \ \text{GeV}$	1.8646	0.0005	0.0005

Table 8.1: The first half of the input parameters to the fit.

parameter	value	positive error	negative error
M_{D^+} GeV	1.8693	0.0005	0.0005
M_{D_s} GeV	1.9685	0.0006	0.0006
f_{ele}^{bb}	0.96	0.01	0.01
f_{muo}^{bb}	0.92	0.01	0.01
Dil Slope Λ_b	0.06	0.23	0.23
Dil Slope D^0	0.58	0.42	0.42
Dil Slope D^+	0.14	0.29	0.29
Dil Slope D_s	0.66	0.62	0.62
B^0 d-tag probability p1	14.4	1.2	1.2
B^0 d-tag probability p2	.084	0.012	0.012
B^0 d-tag probability p3	0.026	0.007	0.007
B^0 d-tag dilution p1	9.136	8.48	8.48
B^0 d-tag dilution p2	0.32	0.13	0.13
B^0 d-tag dilution p3	-0.340	0.04	0.04
B^+ d-tag probability p1	17.2	2.2	2.2
B^+ d-tag probability p2	0.077	0.008	0.008
B^+ d-tag probability p3	0.020	0.005	0.005
B^+ d-tag dilution p1	33.38	26.27	26.27
B^+ d-tag dilution p2	0.74	0.51	0.51
B^+ d-tag dilution p3	-0.23	0.06	0.06

Table 8.2: The second half of the input parameters to the fit.

parameter	positive error	negative error
$\Delta m_d (ps)^{-1}$	0.017	0.013
D^0	0.021	0.005
D^+	0.0283	0.0245

Table 8.3: Systematic errors associated with the input parameters.

8.0.2 k -Factor Distributions

The k -factor distributions, shown in Figures 5-3 and 5-4, are basic components in the transformation of the proper time dependent asymmetries to the pseudo-proper time dependent asymmetries. The central value of the k -factor distributions and the particle lifetimes together determine the scale for the pseudo-proper time. We considered two sources of systematic effects on the determination of the k -factor distributions, the decay model for B mesons and the effective isolation selection requirements for the trigger electrons.

Decay Model

The k -factor distributions are determined by the multiplicity and kinematics of the hadron decays associated with the secondary vertices in the inclusive lepton samples. These distributions are sensitive to the energies carried by the trigger lepton, neutrino, and neutral decay products. We used the QQ program [28] developed by the CLEO collaboration to simulate the decay of B mesons. In order to estimate the impact of the decay model on the measurement, we generated new samples of electron and muon $b\bar{b}$ events in which the B meson is decayed according to phase space. From these Monte Carlo samples, we recomputed the k -factor distributions for the B mesons, and fit the data to determine Δm_d and the charged and neutral B dilutions. We took the differences between the output parameter values determined from this fit and the original fit to be the systematic errors, which we symmetrized since there is no physical reason to expect the error due to the decay model to be either positive or negative. The systematic errors determined from this effect is shown in Table 8.4.

parameter	positive error	negative error
$\Delta m_d (ps)^{-1}$	0.003	0.003
D^0	0.0	0.0
D^+	0.0	0.0

Table 8.4: Systematic errors associated with the decay model.

Electron Isolation

We forced the p_t distribution of the trigger lepton determined from the Monte Carlo to agree with distribution determined from the data by weighting the Monte Carlo accordingly (Figure 4-3). As explained in section 6.2.1, the trigger electron is isolated by the requirement that there be very little energy measured in the hadronic calorimeter near the electron track. This selects decays for which the hadrons do not travel along with the trigger electron. If the Monte Carlo detector simulation did not properly emulate the effects of this isolation requirement but the Monte Carlo still (as a result of the weighting) provided the same electron p_t spectrum as the data, the kinematics of the B decays that satisfy the isolation requirement would have to be different in the Monte Carlo compared to the data. If the kinematics of the B decays were different, the k -factor distribution would be different as well. To account for this effect we interchanged the electron and muon k -factor distributions since the muon is not required to be isolated. We symmetrized the difference between the two fits as the systematic error, shown in Table 8.5.

parameter	positive error	negative error
$\Delta m_d \text{ (ps)}^{-1}$	0.002	0.002
D^0	0.001	0.001
D^+	0.001	0.001

Table 8.5: Systematic errors associated with the modeling of electron isolation.

8.0.3 L_{xy} Resolution

If the resolution in L_{xy} (and thus t') is not properly simulated in the Monte Carlo, we would expect to see a bias in the determination of Δm_d . The argument of the

resolution function, $t' - t/k$, is proportional to the width of the resolution in L_{xy} , ΔL_{xy} . A conservative estimate on the L_{xy} resolution is 20% [32]. We therefore rescaled the proper time resolution function by $\pm 20\%$ and re-fit to determine the systematic effects on the fit parameters from the shifts in the output parameters. Table 8.6 shows the systematic uncertainties due to the uncertainty on the L_{xy} resolution scale.

parameter	positive error	negative error
$\Delta m_d \text{ (ps)}^{-1}$	0.008	0.008
D^0	0.003	0.003
D^+	0.001	0.001

Table 8.6: Systematic errors associated with the resolution in L_{xy} .

8.0.4 Tagging on B Daughters

We used Monte Carlo studies to determine the fraction of B^0 and B^+ events that are SST-tagged on B daughters as a function of pseudo-proper time. We also determined the SST asymmetries as a function of pseudo-proper time when the SST tag is determined by B daughters. If the Monte Carlo does not accurately model the daughter-tagging probabilities and asymmetries, the fit may be biased. The number and distribution of fragmentation tracks relative to B daughter tracks dominates the daughter-tagging probabilities and asymmetries. We therefore compared the daughter-tagging shapes from two versions of Pythia, one that was tuned [27] to match fragmentation distribution in $b\bar{b}$ production (the Monte Carlo sample used in this analysis), and one that was untuned. In the untuned Pythia sample, we re-determined the daughter-tagging probabilities as a function of t' and the associated asymmetries, using the same functional form for the parameterizations. We used these new parameterizations to fit for the four output parameters in this analysis. We symmetrized the differences between the old and new values as the systematic

uncertainties from the use of Monte Carlo in modeling daughter-tagging for the fitter. The systematic errors due to this effect is shown in Table 8.7.

parameter	positive error	negative error
$\Delta m_d (ps)^{-1}$	0.019	0.019
D^0	.003	.003
D^+	0.0	0.0

Table 8.7: Systematic errors associated with the Monte Carlo model for daughter-tagging.

8.0.5 Dilutions for Particles Other Than B^0 and B^+

We used the ratio of dilutions for Λ_b , B_s , D^0 , D^+ , and D_s to the neutral B dilution at $t' = 0.3$ cm from the Monte Carlo. We follow the same procedure as we did in estimating the effect of daughter-tagging: repeating the fit using ratios derived from the untuned Pythia Monte Carlo and symmetrizing the difference in fit results. Table 8.8 shows the systematic uncertainties due to the uncertainty on the ratios of dilutions.

parameter	positive error	negative error
$\Delta m_d (ps)^{-1}$	0.0	0.0
D^0	.001	.001
D^+	0.002	0.002

Table 8.8: Systematic errors associated with the Monte Carlo determination of dilution ratios.

8.1 Total Systematic Errors

We summed in quadrature the systematic errors from the identified sources of uncertainty. We find that the systematic errors are considerably smaller than the statistical errors for Δm_d while they are comparable for the dilutions.

parameter	σ_{sys}^+	σ_{sys}^-	σ_{stat}^+	σ_{stat}^-
$\Delta m_d (ps)^{-1}$	0.027	0.025	0.09	0.09
D^0	0.0214	0.007	0.03	0.03
D^+	0.0284	0.0246	0.03	0.04

Table 8.9: Combined systematic errors, dominated by the input parameters and the Monte Carlo model for daughter-tagging.

Chapter 9

Conclusions

In this thesis we have unambiguously shown that it is possible to study B mesons in inclusive lepton samples at hadron colliders by exploiting charge-flavor correlations in the production process. In our measurement of Δm_d , we have resolved difficulties due to large backgrounds and the effects from tagging on B daughters inherent to the inclusive environment. Two novel aspects of this analysis are the construction of a voting based same side tagging algorithm and the use of distributions over r and ΔR to separate B daughter tracks from primary tracks. We measured the neutral B meson mixing frequency to be

$$\Delta m_d = 0.42_{-0.09}^{+0.09}(\text{stat})_{-0.03}^{+0.03}(\text{sys}) \times (\text{ps})^{-1}.$$

This measurement is statistics limited. The statistical precision of our determination of Δm_d is within the range of other measurements performed at CDF. An inclusive lepton analysis, using both the Soft Lepton and the Jet Charge opposite side taggers, has a statistical error of 0.05 [31] while a partially reconstructed analysis using $\bar{B}^0 \rightarrow l\bar{\nu}D^{*+}X$ using the Soft Lepton tagging algorithm to determine the production flavor has a statistical error of 0.099 [35]. The world average is given by $\Delta m_d^{\text{world}} = 0.46 \pm 0.018$ [4].

9.0.1 Future Applications

The Tevatron and the CDF detector are currently being substantially upgraded for a new data taking run called Run II. Nearly twenty times the data collected in Run I will be recorded in the first phase of Run II. There will be improved versions of the CTC and SVX tracking detectors. In particular, the new silicon vertex detector will record tracks in three dimensions. There will be a Level 2 trigger to select events with displaced tracks. This will provide a high statistics low background B event sample. With three-dimensional silicon vertexing, the differentiation between B daughters and primary tracks should be much more effective. The techniques outlined in this thesis should allow for clean inclusive B measurements.

A possible extension of the techniques employed in this analysis is to use the distributions that separate daughter tracks from primary tracks for secondary vertexing. By adding charges of tracks with high probability of being a B daughter to the sum of the charges of the tracks that comprise a secondary vertex, the charge of the decaying b hadron can be determined. The most significant background source in this analysis is the decays of charged B mesons. A charge determination of the decay vertex would allow for a significant reduction in the charged B background as well as a means to reduce the correlations between the measured charged B dilution and Δm_d . This is because the offset due to charged B mesons in the measured asymmetry would be smaller and better determined. The probability distributions can also be used to improve the proper time resolutions by helping to provide better measurements of B momenta and the location of B decays.

The Voting SST algorithm as constructed for this analysis is independent of the Soft Lepton and Jet Charge opposite side taggers. The simultaneous application of both the opposite side taggers and our SST algorithm would therefore provide a better Δm_d measurement than using OST or SST algorithms exclusively.

Voting SST algorithms should prove useful in both inclusive and exclusive B samples for production flavor tagging. This technique can play an important role in reducing uncertainties in future measurements of Δm_d and Δm_s as well as in

observing CP violating effects at hadron colliders.

Appendix A

The Statistical Error on an Asymmetry

A measured raw mixing asymmetry, \mathcal{A}_{raw} , is defined in terms of the number of events for which the production and decay flavor taggers are the same sign, \mathcal{S} , and the number events that they are the opposite sign, \mathcal{O} :

$$\mathcal{A}_{raw} = \frac{\mathcal{S} - \mathcal{O}}{\mathcal{S} + \mathcal{O}}. \quad (\text{A.1})$$

Since every flavor tagged event falls into one of the two categories, the probability distribution over \mathcal{A}_{raw} is binomial. We can therefore express the error on the asymmetry in terms of the true asymmetry, \mathcal{A}_{true} and the number of events. It is convenient to make the following definitions:

$$n \equiv \mathcal{S} + \mathcal{O} \quad (\text{A.2})$$

$$s \equiv \frac{\mathcal{S}}{n}. \quad (\text{A.3})$$

We call the true probability for getting a same-sign event \bar{s} . The same sign fraction, s , is related to the asymmetry by

$$s = \frac{1 + \mathcal{A}_{raw}}{2} \quad (\text{A.4})$$

$$\bar{s} = \frac{1 + \mathcal{A}_{true}}{2}. \quad (\text{A.5})$$

According to the binomial distribution, the variance on s is given by

$$\sigma_s^2 = \frac{\bar{s}(1 - \bar{s})}{n} = \frac{1}{n} \left(\frac{1 + \mathcal{A}_{true}}{2} \right) \left(\frac{1 - \mathcal{A}_{true}}{2} \right) = \frac{1 - \mathcal{A}_{true}^2}{4n}. \quad (\text{A.6})$$

We can express \mathcal{A}_{raw} in terms of s to get

$$\sigma_{\mathcal{A}_{raw}}^2 = \sigma_s^2 \left(\frac{ds}{d\mathcal{A}_{true}} \right)^2 = 4\sigma_s^2 = \frac{1 - \mathcal{A}_{true}^2}{n}. \quad (\text{A.7})$$

So the error on the asymmetry is given by

$$\sigma_{\mathcal{A}_{raw}} = \sqrt{\frac{1 - \mathcal{A}_{true}^2}{n}}. \quad (\text{A.8})$$

We define the production flavor tagging efficiency, ϵ to be:

$$\epsilon \equiv \frac{n}{N}, \quad (\text{A.9})$$

where N is the number of events prior to production flavor tagging. When it is necessary to correct the raw asymmetry by a scale factor,

$$\mathcal{A}_{raw} = D\mathcal{A}_{corr} \quad (\text{A.10})$$

we get for the error on the corrected asymmetry:

$$\sigma_{\mathcal{A}_{raw}} = D\sigma_{\mathcal{A}_{corr}} \quad (\text{A.11})$$

and we therefore get

$$\sigma_{\mathcal{A}_{corr}} = \sqrt{\frac{1 - \mathcal{A}_{true}^2}{N\epsilon D^2}}. \quad (\text{A.12})$$

It is because of Equation A.12 that we optimized the probability cut by maximizing ϵD^2 and thereby minimizing the error on the asymmetry.

Bibliography

- [1] N. Cabibbo, Phys. Rev. Lett.**10**, 531 (1963).
- [2] M. Kobayashi and T. Maskawa, Progr. Theor. Phys. **49**, 652 (1973).
- [3] V. F. Weisskopf and E. P. Wigner, Zeits. f. Phys. **63**, 18 (1930).
- [4] C. Casso *et al*, (The Particle Data Group), 1999 Web Update of Particle Listings, July 6, 1999.
- [5] T. Inami and C. S. Lim, Progr. Theor. Phys. **65**, 297 (1981).
- [6] A. J. Buras and M. . Lindner, “Heavy flavors,” *Singapore, Singapore: World Scientific (1992) 785 p. (Advanced series on directions in high energy physics, 10)*.
- [7] G. Danby *et al.*, Phys. Rev. Lett **9**, 36 (1962).
- [8] M. Gell-Mann, Phys. Lett **8**, 214 (1964).
- [9] G. Zweig , CERN Report 8419/Th 412 (1964).
- [10] E. D. Bloom *et al.*, Phys. .Rev. Lett. **23**, 930 (1969).
- [11] S. L. Glashow, J. Iliopoulos, and L. Maiani, Phys. Rev.**D2**, 1585 (1970).
- [12] J. H. Christenson *et al.*, Phys. Rev. Lett. **13**, 138 (1964).
- [13] S. W. Herb *et al.*, Phys. Rev. Lett. **39**, 252 (1977).
- [14] F. Abe *et al.*, Phys. Rev. Lett. **74**, 2626 (1995).

- [15] L. Wolfenstein, Phys. Rev. Lett. **51**, 1915 (1983).
- [16] L. L. Chau and W. Y. Keung, Phys. Rev. Lett. **53**, 1802 (1984).
- [17] F. Abe *et al.*, Nucl. Inst. and Meth. Phys. Res., **271A**, 387 (1988);
Fermilab-Pub-94/024-E, submitted to Nucl. Instrum. Methods Phys. Res.
- [18] P. Sphicas and D. Vucinic *On Using Pythia to Model the Underlying Event in B and W Events*, CDF internal note number 4097 (1998).
- [19] M. Gronau A. Nippe J. Rosner, Phys. Rev. **D 47**, 1988 (1993).
- [20] H.-U. Bengtsson and T. Sjöstrand, Computer Physics Commun. **46**, 43 (1987).
- [21] T. Reggie, Nuovo Cimento **14**, 951 (1959).
- [22] X. Artru and G. Menessier Nucl. Phys. **B70**, 422 (1975).
- [23] Y. Nambu Phys. Rev. **D12**, 2060 (1975).
- [24] The first B^0 mixing analysis was time integrated: H. Albrecht *et al.* [ARGUS COLLABORATION Collaboration], Phys. Lett. **B192**, 245 (1987).
For another example see: M. Artuso *et al.*, Phys. Rev. Lett. **62**, 2233 (1989).
- [25] W. Yao *et al*, CDF Internal Note 2716 (1994).
- [26] B. Mattingly *et al*, CDF Internal Note 2615 (1994).
- [27] D. Vucinic, Massachusetts Institute of Technology, Ph.D. dissertation, *Observation of Excited B Mesons in $p\bar{p}$ Collisions at $\sqrt{s} = 1.8$ TeV*, September, 1998.
- [28] P. Avery, K. Read, and G. Trahern, Cornell Internal Note CSN-212, March 25, 1985 (unpublished). We use version 9.1.
- [29] N. Isgur and M. B. Wise, Phys. Lett. **B237**, 527 (1990).
- [30] M. Shapiro *et al.*, CDF Internal Note 1810 (1992).

- [31] O. Long, University of Pennsylvania, Ph.D. dissertation, *A Proper Time Dependent Measurement of Δm_d Using Jet Charge and Soft Lepton Flavor Tagging*. See also: O. Long, J. Kroll, N. Lockyer, M. Paulini, M. Peters, M. Shapiro *An Update of the Vertex Tagged Inclusive Lepton Data Proper Time-Dependent B^0 Mixing Analysis*, CDF internal note number 4315 (1997).
- [32] P. Maksimovic, Massachusetts Institute of Technology , Ph.D. dissertation, *Observation of $\pi - B$ meson Charge-flavor Correlations and Measurement of Time Dependent $B^0 \bar{B}^0$ Mixing in $p\bar{p}$ Collisions*, November 1997.
- [33] K. Kelley, Massachusetts Institute of Technology, Ph.D. dissertation, *Measurement of the CP -violation parameter $\sin(2\beta)$* , September 1998.
- [34] Petar Maksimović, Private communication.
- [35] T. Affolder *et al.* [CDF Collaboration], Phys. Rev. **D60**, 112004 (1999).